Illuminating Correlated Matter with Angle-Resolved Photoemission Spectroscopy

Dissertation
zur
Erlangung der naturwissenschaftlichen Doktorwürde
(Dr. sc. nat.)
vorgelegt der
Mathematisch-naturwissenschaftlichen Fakultät
der
Universität Zürich
von
Kevin Pasqual Kramer
aus
Zürich, ZH

Promotionskommission

Prof. Dr. Johan Chang (Vorsitz)
Prof. Dr. Titus Neupert
Prof. Dr. Claude Monney

Zürich, 2022

Illuminating Correlated Matter with Angle-Resolved Photoemission Spectroscopy

PhD thesis presented to
the Faculty of Science of
the University of Zurich
by Kevin Pasqual Kramer

PhD committee
Prof. Dr. Johan Chang (Head)
Prof. Dr. Titus Neupert
Prof. Dr. Claude Monney

University of Zurich[UZH]

Zürich, 2022

Preface

The foremost and official purpose of this PhD thesis is to present novel scientific insights that have resulted from the projects carried out in the course of my four year engagement as a PhD student in Johan Chang's Laboratory for Quantum Matter Research (LQMR). The major results I have contributed to have already been communicated and published in peer-reviewed journals [1–6]. Therefore, large portions of this text naturally constitute repetitions of already available material. The format of a thesis, however, allows me to present said material in a more consistent and more complete manner than what would be possible within the boundary conditions that necessarily accompany academic publications.

Over the past four years, I have learned a lot from all kinds of different people, textbooks and scientific papers. Especially the early stages as a PhD student involve the intake of large amounts of new information. I have found that some of the most useful resources for me during that time were other people's PhD theses, because they contain explanations and overviews of the state-of-the-art in the field, written from a viewpoint not too far from my own. Now that my time has come to write up a thesis, I hope that this document can serve as a useful starting and reference point for people who are entering this exciting yet perhaps intimidatingly large and quickly developing field.

Thesis summary

The thesis opens with an introductory chapter that talks about the larger picture and motivations behind the concrete and very specific research results that are presented in the later chapters. In the following three chapters, we then zoom into the research landscape and lay down the core concepts necessary for the understanding of the results. Chapter 2 revolves around technical and engineering aspects of angle-resolved photoemission spectroscopy (ARPES), the experimental technique primarily employed by me during my PhD studies. A focus is put on explaining the foundations that underly some of the selection rules and enhancement effects that can be made use of by the experimenter to obtain additional information. Chapter 3 first takes a step back and reviews some broadly applied concepts in condensed matter physics, such as the foundations for density functional theory calculations, before honing in on the theoretical core underlying ARPES: the spectral function and its description of correlated matter in terms of the self-energy. The contents of chapter 4 are directly aimed at researchers in the position of analyzing ARPES data. The most important aspects of ARPES postprocessing and analysis are explained in quite some detail. In the chapter's last section I present the software suite `data-slicer` which I have developed in order to support ARPES experimentation at synchrotron facilities.

The remaining chapters lay out and discuss experimentally obtained physical results. A series of new insights has been gained on the material family of the cuprate high-temperature superconductors. Concretely, these entail (i) the discovery of a two dimensional type-II Dirac cone in , (ii) three-dimensionality of the Fermi surface in overdoped La-based cuprates, (iii) identification of the Cu $d_{3z^2-r^2}$ derived band in five electron- and hole-overdoped cuprate compounds, (iv) a universal methodology for density functional theory based electronic structure calculations for the same five compounds and (v) the formulation of a spectroscopic analog of the Kadowaki-Woods relation, unifying the

Fermi liquid picture for oxides.

The realitiy of the academic publication process has led to these observations being published in separate papers, obscuring their interconnectivity. Writing this thesis provided me with the chance to collect these results in one spot and show how they have come about. I have attempted to lay out how these successive experimental observations have come about in a coherent and almost chronological manner. Hopefully, this allows the reader to comprehend how the collective understanding of these systems has changed within the LQMR group and makes it possible to understand our viewpoints even better than by reading the individual papers. Chapter 5 lays out the results on the electronic band structures of overdoped cuprate high-temperature superconductors while chapter 6 explains how the sum of these band structure observations has allowed us to employ considerations from Fermi liquid theory to formulate a spectroscopic version of the Kadowaki-Woods relation.

Finally, in chapter 7 I review our findings on the heavy fermion compound $CeRu_2Si_2$. There, we have been able to obtain ARPES data of unprecedented quality. This has allowed us to employ a polarization dependence analysis to uniquely identify the Ru d derived conduction bands. Calculations of the orbital overlap between these conducting d states and the localized Ce $4f$ electrons provide a measure for the strength of the hybridization between these bands. The calculations also predict a temperature dependence of the hybridization strength, which implies a Fermi surface reconstruction with change in temperature. This reconstruction is observed experimentally and we are able to connect it to the break-up of composite Kondo quasiparticles.

Contents

Glossary and Acronyms

1D	**One dimensional**.
2D	**Two dimensional**.
3D	**Three dimensional**.
ARPES	**Angle-resolved photoemission spectroscopy**. An experimental technique that can give direct insights into electronic dispersions of condensed matter. Thoroughly introduced in chapter 2.
—	**Antinode**. In the context of the cuprate HTSCs the antinode refers to the BZ horizontal or vertical, 45° rotated from the nodal direction. See node.
VUV-ARPES	**ARPES using visible to ultraviolet energies**.
BCS	**Bardeen-Cooper-Schrieffer**. The three phycisists accredited for their explanation of conventional superconductivity.
Bi2201	$\mathbf{Bi_{2-x}Pb_{x+y}Sr_{2-y}CuO_{6+\delta}}$.
BCT	**Body-centered tetragonal**.

BZ	**Brillouin zone**. Analog of the unit cell of a crystal lattice for the reciprocal lattice in k-space. Thanks to Bloch's theorem, the description of dispersions in a periodic crystal can be reduced to the first BZ.
—	**Ce-122**. Short notation we use here for tetragonal materials with the composition CeT_2Si_2, where T refers to a transition metal ($T \in \{Cu, Ru, Au, Rh, Pd, \dots\}$.
CCD	**Charge coupled device**. Semiconducter based light detectors, widely used in imaging technology.
—	**Cleave**. Here refers to a common method for obtaining atomically flat and uncontaminated surfaces. See section 2.2.2.
CMP	**Condensed matter physics**. A large subfield of modern physics with close vicinity to material science. It is concerned with the study of properties of matter in a condensed state.
CEF	**Crystal electric field**. Also *ligand field*. The electric field exerted at a site of interest by the NN atoms (ligands). The effects of the CEF typically lead to a lifting of degeneracy of the energy levels on that site.
CSRO	$\mathbf{Ca_{1.8}Sr_{0.2}RuO_4}$.
—	**Cuprate**. Here used to refer to the cuprate SCs, a class of materials that are made up of CuO_2 layers separated by other metal oxide layers. The cuprates prominently exhibit unconventional superconductivity at record-holding high transition temperatures.
DOS	**Density of states**. A function of energy whose integral between two values is the number of states present in that energy window.

DFT	**Density functional theory**. The backbone of many electronic structure calculations. See section 3.2 in chapter 3 for an introduction.
DLS	**Diamond Light Source**. A synchrotron facility in Oxford, United Kingdom.
—	**Dispersion**. The relation between energy and momentum of a (quasi)particle.
DMFT	**Dynamical mean field theory**. An approach to electronic structure calculations where the untractable interactions between particles are mapped onto the problem of a *local* impurity interacting with a bath of non-correlated electrons.
eV	**Electronvolt**. The kinetic energy gain of an electron when accelerated through an electrical potential of 1 V.
EDC	**Energy distribution curve**. A line of constant momentum in an EDM.
EDM	**Energy distribution map**. ARPES intensity distribution as a function of angle (crystal momentum) and energy. Sometimes referred to as an ARPES spectrum.
ESNO	$\mathbf{Eu_{2-x}Sr_xNiO_4}$.
Eu-LSCO	$\mathbf{La_{2-x-y}Eu_xSr_yCuO_4}$.
FSM	**Fermi surface map**. An experimentally obtained representation of the FS.
—	**Fermi velocity**. Velocity of QPs at the Fermi level. Here denoted v_F.
—	**Fermi level**. Also *Fermi energy* or sometimes *Fermi edge*. Energy separating occupied from unoccupied states in the ground state. Thermodynamically it is the energy required to add one electron to a system.

—	**Fermi liquid**. Refers to a system that can be described by Landau's Fermi liquid theory, i.e. where there is a direct correspondence between the particles of a hypothetical, identical but non-interacting system and the renormalized QPs of the interacting system. See section 3.3.3.
FS	**Fermi surface**. A surface in k-space that separates occupied from unoccupied energy levels in the ground state. Electrons lying in the vicinity of the FS usually dominate the physically observable properties.
FWHM	**Full width at half maximum**.
GGA	**Generalized gradient approximation**. An extension to DFT.
GUI	**Graphical user interface**.
HDD	**Hard disk drive**.
HTSC	**High-temperature superconductor**. A material that exhibits superconducting properties that cannot be explained by conventional BCS theory.
INS	**Inelastic neutron scattering**.
k-space	**Reciprocal space**. Also *momentum space*. The vector space spanned by the components of the momentum wave vector **k**. It is essentially the Fourier transform of *real* space and, due to the periodicity of crystal lattices, an omnipresent concept in CMP. long
LQMR	**Laboratory for Quantum Matter Research**. Johan Chang's research group at the University of Zürich.
LV	**Linear vertical**.
LH	**Linear horizontal**.

LDA	**Local density approximation**. An essential approximation for the feasability of electronic structure calculations. See also DFT and section 3.2 in chapter 3.
LSCO	**$La_{2-x}Sr_xCuO_4$**.
MBPT	**Many-body perturbation theory**.
—	**Mirror plane**. The experimental mirror plane in ARPES is defined by the vector of the incoming photon and the vector of the photoemitted electron. See figure 2.5. Symmetry with respect to this plane can have important consequences on the photoemission intensity.
MDC	**Momentum distribution curve**. description=Constant energy line in an enegy-k spectrum.
—	**Mott insulator**. A material that would be expected to be conducting from a band structure perspective, but turns out to be insulating due to strong repulsive interactions effectively splitting the conduction band, resulting in a band gap.
NN	**Nearest neighbor**.
NNN	**Next nearest neighbor**.
—	**Node**. In this context usually referring to a point in k-space where an energy gap vanishes. For the cuprate HTSCs, the nodal direction refers to the BZ diagonal, where the pseudogap is zero.
PSI	**Paul Scherrer Institute**. A research facility in Villigen, Switzerland. Hosts, among other things, an electron-synchrotron, neutron scattering beamlines and a free electron laser.

PES	**Photoemission spectroscopy**. A photon in – electron out measurement technique that can give insight into the electronic DOS.
PLCCO	**$Pr_{2-x-y}La_xCe_yCuO_4$**.
PIT	**Python Image Tool**.
QCP	**Quantum critical point**. Quantum analouge of a classical critical point where the phase transition is a consequence of quantum fluctuations, as opposed to thermal fluctuations. Consequently, occurs only at $T = 0\,\mathrm{K}$, but with observable effects in its vicinity in the phase diagram.
QO	**Quantum oscillation**. Usually refers to a measurment technique based on de Haas-van Alphen effect in which the periodic modulations of physical observables, such as the magnetic susceptibility, with inverse magnetic field strength are used to obtain information on the FS structure.
QP	**Quasiparticle**. A (collective) excitation that results from interactions in a system can often be treated as if it were a non- or weakly interacting particle with its own dispersion relation. In that case we speak of a quasiparticle.
STS	**Scanning tunneling spectroscopy**. An operational mode of a scanning tunneling microscope setup that can give spatially resolved spectroscopic information.
—	**Self-energy**. In the context of CMP, the self-energy contains the net effects of (untractable) electronic interactions on a particle's total energy. This complex quantity is denoted as Σ here.
SX-ARPES	**Soft x-ray ARPES**.

SOC	**Spin-orbit coupling**. The quantum mechanical interaction between a particle's spin- and orbital-angular momenta.
SMES	**Superconducting magnetic energy storage**.
SQUID	**Superconducting quantum interference device**. A highly sensitive device for the measurement of magnetic fields. It is technologically based on the principle of Josephson junctions.
SC	**Superconductor**. A material that shows a resistivity drop to zero and perfect diamagnetism when cooled below a characteristic critical temperature T_c.
SLS	**Swiss Light Source**. The synchrotron at PSI.
TB	**Tight binding**. A model for the description of the electronic structure of condensed matter where the conduction electrons are thought to be tightly bound to the ionic sites and predominantly move between sites by *hopping* from one to the next.
Tl2201	$\mathbf{Tl_2Ba_2CuO_{6+\delta}}$.
UHV	**Ultra high vacuum**. Pressure conditions below $100\,\mathrm{nPa} = 1 \times 10^{-9}\,\mathrm{mbar} \approx 7.5 \times 10^{-10}\,\mathrm{Torr}$.
VHS	**Van Hove singularity**. A divergence in the DOS that typically arises as a consequence of the dispersion relation going through a maximum, minimum or saddle point.
—	**Work function**. The amount of work necessary for an electron in a material to escape through the surface into vacuum. This is a surface property and here denoted as $e\Phi$.
XAS	**X-ray absorption spectroscopy**.

Acknowledgements

It is not possible for an individual to make scientific progress without relying directly or indirectly on the help of others. Experiments cannot be conducted without the teams that constructed and maintain the experimental stations. Software cannot be written without relying on already existing software suites, frameworks or programming languages. The efforts to build experimental stations or software frameworks, in turn, depend on know-how and experience from preceding pioneering endeavours or work from different fields. Furthermore, all these efforts can only be maintained in a functioning and fruitful environment that gives people the opportunity to reach the necessary education and sustains their hard work. From this viewpoint, it becomes clear that any form of progress is really the natural result of societal developments, one might call it a kind of emergent phenomenon, and the presented work forms no exception. I would therefore ask the reader to keep this fact in awareness during the lecture of this thesis and not get lured into the false impression that the presented work could be the achievement of a single person alone, despite the fact that the document bears the name of one single author and is largely formulated using the *editorial we* (with the obvious exception of this very personal section and any situation where a statement directly reflects a personal decision or opinion). It should be pointed out, however, that any responsibility for the contents of this thesis and potential mistakes, falsehoods or otherwise problematic elements therein lies with me alone.

I would like to dedicate the rest of this section to acknowledge and point out some of the people who have been involved with this work and made valuable contributions in a more direct sense. At the same time, I would like to give thanks to people who have been important, helpful, valuable or otherwise dear to me in my academic and personal development during the time of my PhD studies.

I am grateful on many levels to my principal advisor Johan Chang. While his scientific expertise and drive are obvious to anyone who meets

him, his unparalleled dedication to his students and group members becomes clear very quickly, too. I am thankful for his guidance and advice, the many constructive discussions and the opportunities he has provided and continues to provide for me. It is clear that he cares for his students far beyond the work that is conducted in the Laboratory for Quantum Matter.

Within the group, I have always enjoyed an exceptionally friendly and collaborative atmosphere. Denys Sutter was my originial entry point into the group and I was wise to follow him. I could benefit greatly from his experience as a senior PhD student and his spot on meta analyses as well as his unique humorous character that would lighten up the experimental sessions. As another senior in the synchrotron team, I have spent many experimental shifts with Masafumi Horio. While these were first and foremost amazing opportunities for me to learn from a true ARPES master and benefit from his crystal clear explanations of the core concepts and subtleties, I have also always enjoyed his calm nature and the interesting discussions about Japanese (pop) culture. He continues to be a role model in correctness and clear-headedness.

The beamtimes were later joined by Karin von Arx, Qisi Wang and Julia Küspert, all of whom contributed tremendously to these often taxing periods both on the scientific and personal sides. These three have also shared an office with me, which enabled lots of pleasant and interesting exchanges. Furthermore, they have been extremely kind to carefully read through the draft version of this thesis during a very stressful period of experiments and proposal submission deadlines. Their keen and attentive comments have contributed enormously to the improvement of this document.

While I did not have the chance to work more directly with many of the other group members, I am most grateful to have been surrounded by such good people during all this time. I thank Lakshmi Das for combining sillyness with existential philosophy, Daniel Destraz for his razor sharp observations and for getting me engaged in university politics, Jaewon Choi for exchanging Baduk wisdom for skiing instructions and

Ruggero Frison for sharing interesting viewpoints and the development of an alternate system for keeping that *darn* office window open. In the lab, Dominik Biscette and Damian Bucher have always been able to help out by finding an easier way of doing things.

Further very valuable support during beamtimes was often provided by Yasmine Sassa and *fake* Kevin Hauser, as well as Anar Bold. It has been enriching to witness how each individual was able to bring something unique to the experience of experimental shift work. None of the experiments would have been possible without the commitment and helpful support of the teams at the respective beamlines. I therefore owe many thanks to Eli Rothenberg and Aaron Bostwick from the MAESTRO beamline at the Advanced Light Source, Berkeley, to Nicholas Plumb, Wojciech Pudelko, Jonas Krieger, Niels Schröter and Vladimir Strokov from the SIS and ADDRESS beamlines at Paul Scherrer Institute (PSI), to Timur Kim, Céphise Cacho and Moritz Hösch from I05 at Diamond Light Source (DLS) and to Julien Rault, Patrick Lefèvre and François Bertran from CASSOPEE at the SOLEIL synchrotron.[1]

On the scientific side, I was lucky that many experienced people have provided guidance, feedback, inputs and tuition. These include Claude Monney and Titus Neupert who were kind enough to be part of my promotion committee as well as Marco Grioni who has kindly agreed to act as a referee for this thesis. Stepan Tsirkin shared lots of his wisdom about density functional theory (DFT). For the heavy fermion project (presented in chapter 7) fruitful discussions were held with Daniel Mazzone and Nicolas Gautier. Even more support was provided by Rina Tazai and her calculations of the relevant orbital overlaps.

Alessandro Vindigni, Jürg Osterwalder, René Monnier, Doug Potter, Romain Teyssier and many others have provided valuable lectures from which I benefitted greatly. I have learned a lot through hands-on

[1] According to Masafumi, SOLEIL is the first and only brown synchrotron building he has ever seen.

experience in the welcoming surrounding of Günther Dissertori's group during a year at CERN with Werner Lustermann, Jannis Fischer, Chiara Casella, Mikiko Ito, Alexander Howard, Christian Haller and Michael Dröge. During another valuable and influential time I have been accompanied and guided by Tom Gregorkiewicz, who unexpectedly but peacefully passed away in July of 2019, Antonio Capretti and the other fantastic people of the Institute of Physics at the University of Amsterdam.

I would like to extend further thanks to the many people that often remain hidden and seldom receive any credit, even though they are essential to the functioning of the whole system through more than just their work alone, but oftentimes also through their sheer willingness to help on a personal level. This includes the administrative team around Carmelina Genovese, Denise Caneve, Monika Röllin and Brigitte Freund, senior scientists with multiple functions such as Matthias Hengsberger and Peter Robmann as well as the Junior Researcher representatives in the Faculty Assembly.

The continuous support and trust of my loving parents as well as my wonderful sister has been a source of strength for which I am very grateful. I am also thankful to my *Grossmami* for her unshakable believe in me. I am truly blessed and privileged to be surrounded by kind hearted people, especially in our gorgeous Yumo Park, and I thank Tobias Kloter, Alexandra Kaufmann, Miku and Toto for sharing this wonderful experience together. Similarly, I thank This for his willingness to proof-read and his general, unparalleled kindness and Giovanni and Noëmi for giving me the chance to experience a completely different way of life and putting things into perspective. A final expression of gratitude and love that can only be diminished by putting it in written form goes out to the love of my life, Hanin.

Chapter 1: General introduction

This first chapter aims at providing orientation for the reader by starting out in a birds-view perspective far above the research landscape and successively zooming in closer until we hone in on the contents of this thesis: angle-resolved photoemission spectroscopy and correlated matter. Diving down, we motivate each stage by answering the *why*'s, i.e. by giving good reasons for why people could be interested in spending time in the respective field of research. While the different sections implicitly convey an answer to the *what*, more concrete elaborations will be presented in chapters 2 to 4.

We start our skydive far out in section 1.1, where we have a great view over all of science, before we quickly approach the field of material science and condensed matter physics in section 1.2. We will discover the fasci-

nating land of correlated matter within condensed matter physics in section 1.3. Finally, in section 1.4, we get our first look at photoemission spectroscopy, where we will land and which we are going to explore more deeply in the next chapters.

The newly obtained scientific results which are presented in this thesis pertain to quite different material groups, namely the cuprates and heavy fermion compounds. Thus, I have decided to keep this introductory chapter rather general. A more concrete presentation of the research situation and open questions in these material families is delegated to the corresponding chapters (5 and 7).

1.1 Why science?

It can be reasonably expected that the grand majority of the potential readership of this thesis comes from a research background and would be intrinsically motivated to contribute to science. It may therefore seem redundant to motivate the scientific endeavour as whole. Personally, however, during my PhD studies I have realised that it can be very useful to have a few clear lines of reasoning ready in order to justify the sometimes massive investments into research.

One of the most impressive demonstrations of the power and success of the scientific method I have read can be found in Yuval Noah Harari's *Brief history of Humankind* [7]. In that text the historian constructs his argument by pointing towards a shift in paradigm and self-awareness of humanity: The shift from an "I know everything" to an "I do not know everything" attitude. To present day humans that have been brought up in a society where the latter point of view is the norm, it can be difficult even to imagine that the former attitude was once dominant. Harari shows this at the example of ancient maps, which, interestingly, never show any blank spaces, even though large parts of the planet had been undiscovered by the respective societies at the time of the maps' creation. Unknown regions were just filled with sea or made up land masses, and a global border arbitrarily drawn. For European societies, the discovery of America triggered the shocking realization that there seemed to be, in fact, much more than they currently knew about. Consequently, maps started to be drawn primarily based on data, rather than according to some philosophical or religious program. They became more accurate and admitted to not having complete information by leaving unknown regions blank. See figures 1.1 and 1.2 for eurocentric examples of this observation.

As long as there does not seem to be anything unknown, there is no reason to go out and explore. From the seemingly simple realization that we do not know everything, immediately follow large efforts to find answers and acquire more knowledge. Societies soon realized the

Figure 1.1: The *Tavola di Velletri*, a world map from the first half of the 15th century. North is oriented at the bottom of the map, so the top shows Africa, the left half Asia and the right half Europe. Hardly any spot on the map is left without a geographic or decorative feature or some descriptive text, giving the impression that all there is to know is already known. File from the public domain.

enormous benefits they could gain by venturing out into the unknown and hardly any effort and cost was spared to conduct countless research expeditions. This paradigm shift slowly expanded from geography to other disciplines of thought and the resulting scientific revolution changed the shapes of societies and the planet they lived on in an unprecedented manner. Even if the overall benefits and harms of this development can and should be critically discussed, it cannot be denied that the core scientific attitude of "I don't know it, but I will try to

Figure 1.2: World map from 1650. Large portions of the map are left blank, admitting to the fact that not enough data was available to the cartographer to draw the map at the precision he or she was aiming for. File from the public domain.

find out" holds almost unimaginable power.[1]

I have often been asked the question why one should waste any time doing elementary or fundamental research, when we have so many urgent problems that require advances in applied research to be tackled. A short answer to this was once provided to me by Brian Schmitt [8]: "If humanity had only ever conducted applied research, we now would have candles that burn very bright and last a long time, but no light bulbs".

[1] As we shall see, many of the novel insights presented in this thesis are linked to venturing into unknown (k-space) regions in order to obtain accurate (Fermi surface) maps.

1.2 Why condensed matter physics?

At the time of this writing, society is indeed faced with challenges of unprecedent scale. These include climate change, pollution of water, air and soil resources and medical threats, such as currently demonstrated by the global COVID-19 pandemic. As laid out before, each scientific discipline has its own justification. In light of the urgency of these great societal questions, however, material science and condensed matter physics (CMP) undoubtedly deserve special attention [9]. The potential of these disciplines to change society can amply be demonstrated at the example of semiconductor research and the development of the transistor, the foundational building block of computers. There is hardly any other technology that has conquered our daily lives and most aspects of economy and industry at such a speed and with such a high impact than the computer.

Innovations from CMP are ubiquitous in medical imaging, sensor and detector systems, applications of lasers and memory technology. Other fields of research, such as other branches of physics or chemistry often benefit from discoveries and insights made in CMP as completely new avenues are unlocked for exploration. Currently, semiconductor research and advances in CMP are used with the goal of creating more efficient solar panels [10], batteries [11] and hydrogen storage technology [12], enabling us to establish a more sustainable energy portfolio. Improvements in carbon capture technologies may make it possible for us to reduce the atmospheric greenhouse gas concentration. While this would not ultimately solve the problem, it can still be expected to hopefully reduce the severity of the consequences of climate change and to effectively buy us time to implement more fundamental solutions.

Even if the solution to societal problems cannot be a purely technological one, it is difficult to imagine that technological innovations are not going to play, at the very least, a supportive role.

1.3 Why correlated matter?

1.3.1 The fascination of superconductivity

If semiconductors are what attracted an enormous audience to join the CMP party, superconductivity might be what makes them stay. The phenomenon was initially discovered by Heike Kamerlingh Onnes as a drop in the resistivity of Hg to unmeasurably small values at temperatures below 4.2 K in the year 1911. His data is shown in figure 1.3 (a). Only two years later, he was awarded the Nobel prize [13].[2] In subsequent research during the first half of the twentieth century, more and more elements and alloys were found to exhibit the signature properties of a vanishing resistivity and a complete expulsion of magnetic fields from the material (perfect diamagnetism, Meissner effect) below a critical temperature T_c and a critical magnetic field H_c.

A vanishing resistivity in a conductor is a truly remarkable phenomenon of quantum physics and completely unexpected from a classical viewpoint. After all, most physicists and engineers would likely sign the statement: "No physical system is without friction". One cannot help but dream about the possibilities that such a *frictionless* conductor could enable. No resistivity means no heating up of the material, which would imply that we can send extremely large currents through such a wire. In fact, it is only limited by the critical current I_c, which is the value at which the induced magnetic field exceeds the critical field H_c. As a second consequence of zero resistivity, we have that a once induced current in a superconducting loop would keep going indefinitely. Nowadays it is indeed empirically confirmed that a superconducting current does not seem to lose any energy. Such currents have been maintained in gravimetric measurement devices for over 26 years [14]. Within the accuracy of the measurement, no decay

[2] At the time of Onnes being awarded the Nobel prize, the importance of superconductivity was not yet recognized, however. The prize was received instead "for his investigations on the properties of matter at low temperatures which led, inter alia, to the production of liquid helium".

of the supercurrent has been detected. Conversely, one can use the errorbar of the measurement to put a lower limit on the lifetime of the supercurrent. That time turns out to exceed the age of the universe.

What keeps the superconducting dreamers on the ground is of course the requirement of extremely low temperatures for the superconducting state to stabilize. If only the intriguing properties of superconductors (SCs) could be accessed at or around room temperature. In 1957, when Bardeen, Cooper and Schrieffer were eventually able to explain the experimental phenomenon, hopes of immediate, amazing technological revolutions were shattered: Their Bardeen-Cooper-Schrieffer (BCS) theory contained an upper limit on the value for T_c. Considering the known elements of the periodic table, this maximum value has been placed in the order of 40 K [15], far below technologically interesting temperatures.[3]

It took another 30 years before the dream would be fully reignited. In 1986, K. A. Müller and J. G. Bednorz of IBM reported a vanishing resistivity in the Ba–La–Cu–O system [18]. The resistivity drop occured at a value of $T_c \approx 30\,\mathrm{K}$ — which is larger than what one would expect for this compound, according to BCS theory. It soon became clear that non-BCS or *unconventional* mechanisms for superconductivity existed and in the time that followed, many new compounds and material families were discovered that exhibit high transition temperatures: high-temperature superconductors (HTSCs). A timeline of the discoveries of compounds and their transition temperatures is found in figure 1.3 (b). Particulary, new members of the cuprates were soon identified which had a value of T_c above the technologically relevant boiling point of liquid nitrogen (77 K). One representant of the cuprates, which has been discovered by Schilling *et al.* at the University of Zürich [19], still holds the record for the highest T_c at ambient pressure with a value of

[3] This value does not consider extreme pressure conditions. The BCS value of T_c for metallic hydrogen is expected to lie approximately at room temperature [16]. The problem is that metallic hydrogen is very difficult to obtain. Recently, however, it has been possible to stabilize metallic H_2S by using astronomically large pressures, resulting in a value of $T_c = 203\,\mathrm{K}$ [17].

130 K. The mechanisms at play in HTSC compounds are still, to this day and despite immense research efforts, not fully understood. Not having an established theoretical framework for HTSCs also means that we do not know of any upper bound for T_c — the dream of a room temperature SC lives on.

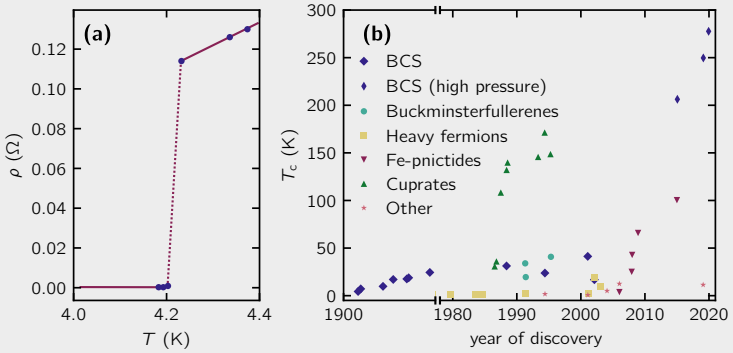

Figure 1.3: History of superconductivity. **(a)** Resistivity drop of Hg at low temperatures as measured by Heike Kamerlingh Onnes. **(b)** Representatives of HTSCs arranged by year of discovery and maximal T_c. Different material families are encoded by marker shapes and colors. Mind the unevenly spaced x axis. Figure adapted from [20] (CC BY-SA 4.0).

1.3.2 Applications of superconductors

What makes physicists and engineers so excited about HTSCs and room temperature superconductivity? Beside a fascination for the underlying physics, it is the technological potential that lies within. HTSCs with transition temperatures that can be reached at relatively low cost by use of liquid nitrogen have many applications already today. They are found, for example, in medical imaging machines, such as

magnetic resonance imaging (MRI) or nuclear magnetic resonance (NMR) devices, where the SCs are necessary to produce the extremely high magnetic fields. With the same function of producing large magnetice fields, HTSCs are also being employed in research applications such as in the Large Hadron Collider (LHC) at CERN or in tokamak fusion reactors [22]. Commercially available superconducting cables can be used to reduce the weight of wind turbines, allowing them to be built higher at a lower effective cost per unit of produced energy [23]. The fact that such wires allow for much larger currents than their conventional metallic counterparts makes them ideal for fast charging of electric vehicles. Further applications of nitrogen cooled HTSCs include geological measurement devices [14] or the maximally sensitive devices for magnetization measurements, superconducting quantum interference devices (SQUIDs).

Overcoming the requirement for cooling, however, would unlock even more groundbreaking applications, many of which would intensely support the electrification of society, and therefore be key to the transition away from fossil fuels. Room temperature SCs are envisioned to be used for power transportation with practically no loss of energy. They could also cut down on the material and space use of electric grid lines. As current in superconducting loops and coils does not decay, such systems can be used for power storage, one of the major hindrances in the way of electrification. In fact, such superconducting magnetic energy storage (SMES) systems have already been used with nitrogen cooled HTSCs [24]. Furthermore, room temperature SCs could be employed in magnetically levitating trains and be key to the electrification of air travel, as they would allow the design of smaller and lighter electromotors, especially once the requirement of cooling to temperatures below 100 K is removed. The Chūō Shinkansen is a magnetically levitating trainline, currently under construction in Japan. It makes use of He-cooled SCs for levitation and propulsion and will reach a maximum velocity of 500 km/h. The so-achieved travel times are going to effectively replace the need for air-travel between Tōkyō

and Ōsaka [25].

A world in which we so urgently need to stop emitting greenhouse gases would massively benefit from the realization of room temperature superconductivity.

1.3.3 Emergent phenomena and the zoo of correlated matter

The intense research that has been carried out on the topic of SCs has led to the discovery of a large variety of new materials which exhibit novel, interesting and often not well understood properties. Exploration of this zoo of new material families and physical phenomena has been the task of many condensed matter phycisists and material scientists in the past decades. It seems that many of the difficult to explain observations originate from the fact that we have strong interactions (or correlations) between the electrons in these compounds. As will be elaborated upon in chapter 3, these correlations are effectively intractable and it is the sheer astronomic number of interactions that are simultaneously at work that produce such unexpected states of matter.

The elementary interactions between two or three charged particles are well understood and widely tought at high school level. The observation that simply combining many of these *simple* interactions can lead to the emergence of completely new phenomena has presented a paradigm shift. As Anderson points out [26], the so-called constructionist hypothesis does not withstand the observation of emergence. In the constructionist point of view, the universe can be described in terms of a set of elementary, fundamental laws. Any observation at a higher level would be seen simply as a repeated application of these fundamental laws, e.g. chemistry would just be an application of CMP, and CMP in turn is just applied particle physics. This line of thinking is often used by physicists to make themselves feel good by thinking: "We are the only ones who understand the world at its most fundamental level and everything else, like psychology, is ultimately just

applied physics". However, the argument is equally likely to be turned around by, e.g. a psychologist: "In order to understand psychology I have to understand biology, which is based on chemistry, which requires me to understand physics. Thus, I have to know about all of these things and more, which makes me the most knowledgable of all".

Everybody would do well in humbly realizing that all attempts at setting up such an hierarchical point of view are incapacitaded in light of the phenomenon of emergence. Even if the elementary interplays at one scale can be understood and described (e.g. interactions and reactions of molecules in chemistry), the collective result of combining many of these interactions is the emergence of effects that could not be predicted from the previous level and require entirely new laws and concepts to be described. To use Anderson's words: "More is different" [26].

With this, we have at least three good reasons to study correlated matter: (i) Any information about the physical laws at work in correlated matter could give us the key insights that are missing for the understanding of unconventional superconductivity. Furthermore, since most HTSCs exhibit emergent phenomena besides superconductivity, it is important to study these different phases separately from each other before we can understand their interplay. (ii) Besides the basic motivation for fundamental science laid out in section 1.1, many of the newly discovered phenomena bear their own potential for interesting applications. (iii) Given that the concept of emergence is present at all scales and could therefore present a truly fundamental (meta) law of the universe, we can hardly spend too much efforts investigating it.

1.4 Why photoemission spectroscopy?

The typical properties of matter one is interested in for technological applications are resistivity, magnetization, specific heat, compressibility and the behaviour of these observables when the external (temperature, pressure) or internal (carrier concentration, doping) conditions are

changed. In order to determine whether a material is superconducting or not, for example, it is enough to check whether its resistivity drops to zero and it exhibits the Meissner effect below a certain temperature. However, the puzzles that correlated matter poses cannot be solved by using such macroscopic probes alone. In order to get a full understanding of the processes that are going on, it is imperative that we illuminate the mystery from all angles, with all methods available to us. Scanning tunneling spectroscopy (STS) and -microscopy experiments [27] deliver direct information about the spatial distributions of atoms and charge fluctuations in a crystal. X-ray and neutron diffraction and scattering techniques have long been established as key probes of matter, giving insights into atomic and magnetic structures. This is showcased by such seminal discoveries as that of the double-helix structure of DNA [28] and antiferromagnetism [29], that have both been awarded a Nobel prize.

Given that many of the most interesting phenomena emerge from electronic correlations, it is clear that obtaining knowledge of the electronic structure is of utmost value. Angle-resolved photoemission spectroscopy (ARPES) is an experimental "photon in – electron out" technique that directly probes the electronic dispersions or the electronic band structure of the material under investigation [30, 31]. That is, ARPES allows to directly visualize and measure the relation between the electron's momentum and its energy inside the sample. Besides the fact that concrete data on the dispersions is rich with physical information, I find it personally most fascinating that a concept as abstract as the electronic band structure can be obtained and visualized in such a direct manner. The work that is presented in this thesis revolves around ARPES and a thorough description of the technological, theoretical and technical aspects of this experimental method is presented in chapters 2 to 4 and thoroughly reviewed in the literature [31].

ARPES has undoubtedly evolved to be a core component in the toolbox of CMP. It has allowed, for example, such important measurements as the angle dependence of the superconducting gap [32,

33]. However, in light of the focus that this text puts on ARPES alone, I want to repeat and stress the point made above: Ultimately, a combination of all available avenues towards insight must be utilized to reach a satisfactory understanding of the currently still unknown.

When I joined Johan Chang's Laboratory for Quantum Matter Research (LQMR) to take up my PhD studies in 2017, I was confronted with the rich body of decades worth of intense research on HTSCs and correlated matter. Many difficult and interesting problems and questions are currently debated in these fields and are still awaiting their solution. Within our team in the LQMR, we have employed ARPES to illuminate some of these issues. The novel insights that were obtained in this process are presented in chapters 5 to 7.

Concretely, chapter 5 contains a series of results on the band structure of cuprate HTSCs, including the discovery of a two dimensional (2D) type-II Dirac cone and the three-dimensionality of the Fermi surface (FS) in $La_{2-x}Sr_xCuO_4$ (LSCO) and La-based cuprates, the identification of the Cu $d_{3z^2-r^2}$ derived band and its influence on material properties across overdoped cuprates and a methodology for their band structure calculations with density functional theory (DFT). Chapter 6 presents ARPES data on the electron-doped cuprate compound $Pr_{2-x-y}La_xCe_yCuO_4$ (PLCCO) with which we have carried out a thorough self-energy analysis. This is combined with previous results in order to obtain a spectroscopic formulation of the Kadowaki-Woods relation, effectively unifying the Fermi liquid picture across a large range of correlated oxide materials. Finally, chapter 7 reviews novel ARPES data on the heavy fermion compound $CeRu_2Si_2$ and shows how the unprecedented data quality has enabled us to completely identify the conduction bands, to characterize their hybridization with the localized Ce $4f$ electrons and to understand the temperature driven FS reconstruction.

Chapter 2: Angle-resolved photoemission spectroscopy

This chapter is concerned with the experimental technique employed in the presented work: angle-resolved photoemission spectroscopy. We start by giving a chronological overview of the evolution of photoemission spectroscopy from the discovery of the underlying principles to the modern day experimental reality in section 2.1. This is followed by a review of the involved technical and physical concepts in sections 2.2 and 2.3, with a focus on polarization selection rules and Fano resonances.

2.1 Chronological overview

Towards the end of the nineteenth century, Heinrich Hertz and Wilhelm Hallwachs reported an intriguing observation of light influencing electrically charged bodies [34, 35]. They found that shining light onto an electrical conductor results in charge being expelled from that material. Closer investigation of this so-called photoelectric effect lead to a series of observations that could not be satisfactorily explained in the framework of classical physics. Progress could only be made after the birth of a completely new idea, namely the concept of light quanta introduced by Max Planck in the year 1900 to find an empirical description for the spectrum of black-body radiation [36]. It was Albert Einstein who then applied this concept of quantized photons to explain the photoelectric effect [37]. These were the first of a series of revolutionary steps that ultimately lead to the introduction of Quantum Physics, and they were acknowledged as such by being awarded the Nobel prize in 1918 (Planck) and 1921 (Einstein).[1]

This photoelectric effect opened the door for deep investigations into the electronic structure of materals by means of photoemission spectroscopy (PES). By illuminating a sample surface with light of a given energy, electrons are expelled. The electrons' kinetic energies can be measured and from that one can infer their energetic structure inside the sample. As an extension to this, if the emitted electrons are filtered or sorted by their momentum in addition to their energy, one can obtain information on the momentum dependent energetic structure, more commonly known as the energy-momentum relation or the *dispersion relation* of the electrons. This is the principle of angle-resolved photoemission spectroscopy (ARPES) [38, 39].

The earliest implementations of ARPES would allow the experimenter to record a single energy distribution curve (EDC) for one discrete angle (momentum) at a time before the experimental geometry

[1] In light of the 100^{th} anniversary of Einstein's Nobel prize, I hope that this thesis can serve as a small tribute to the celebrations.

had to be changed to allow for a measurement at a different angle. The development of *hemispherical electron analyzers* that could simultaneously sort the emitted electrons by energy *and* momentum lead to an order of magnitude increase in experimental throughput [40]. However, ARPES remained a very challenging technique due to its many boundary conditions that are technically difficult to meet simultaneously: Firstly, the experiment has to be conducted under ultra high vacuum (UHV) conditions to prevent sample surface degradation and to ensure the electrons are not scattered or absorbed on their trajectories from the sample towards the analyzer. Secondly, one should be able to move the sample in a stable and reproducible manner along three translational and three rotational degrees of freedom.[2] Furthermore, adjustable sample temperatures reaching as close to absolute zero as possible would be desirable for a range of investiagtions. All of that is combined with the need for stable and high intensity sources of monochromatic light as well as fast and reliable readout electronics. Finally, the requirement for a clean sample surface (as outlined in section 2.2.2) requires the respective advancements in material science and chemistry to enable the growth of suitable single crystals of quasi two dimensional (2D) materials and the development of dedicated preparation techniques that enable a bulk sample to be cleaved — i.e. cut or broken open along an atomic crystal plane.

It is thanks to the efforts of countless technicians and scientists and the evolutions in UHV technology, stable piezo motors for sample manipulators at simultaneous temperature control with cutting edge cryo technology, lasers and increasingly brilliant synchrotron facilities as light sources and much more that current day ARPES stations operate on a whole new level compared to their early ancestors. It is nowadays customary for a regular ARPES session to generate dozens of three

[2] Requiring six degrees of freedom is perhaps spoken from a place of luxury. In principle, four degrees of freedom are enough to carry out a measurement and early setups did indeed operate in this manner. The amount of inconvenience that this must have posed is difficult to imagine for a spoiled experimentor who has benefitted from the advancements made by the pioneers of the past.

dimensional (3D) datasets with total sizes in the order of GiB. This increased throughput has also allowed to add additional parameters to the experiment. While at earlier stages some of the major tunable parameters were the sample temperature, the incident photon energy, polarization and sample doping, new setups now allow for accessing further dimensions. Thanks to highly focused beam spot sizes in the order of tens to hundreds of nm, it is possible to collect ARPES spectra as a function of real space beam position on the sample [41]. This so-called nano-ARPES mode therefore combines reciprocal and real space information. Spin-resolved ARPES allows probing different electronic spin channels separately and time-resolved ARPES can give insights into electron dynamics [42].

2.2 Technical requirements

In order to carry out an ARPES measurement, the following three elements are required:

- A source of monochromatic light. In modern setups this is usually a laser, a He lamp combined with a monochromator or radiation from a synchrotron.
- A clean, single crystalline sample surface of the material under study. This condition implies the necessity of a UHV atmosphere.
- A means of sorting the expelled electrons by energy and momentum, typically through a so-called electron analyzer.

In the following, we will give a short discussion of these three elements and how they were implemented in the presented work.

2.2.1 Synchrotron radiation

As stated earlier, when it comes to the choice of light source for an ARPES experiment, three main options exist: a laser, a He lamp

or synchrotron radiation. Using a laser or a He lamp has several advantages, such as high energy resolution up to the sub-meV range [42] and the ability to operate an independent setup that is always available to the experimenter without the need to apply for beam time and travel to a synchrotron facility. However, with a laser based setup one is constrained to a fixed and discrete photon energy depending on the used laser or to a comparatively small energy window in the case of a He lamp. In these two cases, the available energies are in the order of tens of electronvolt (eV), which limits the accessible area in k-space as is indicated in figure 4.3. Synchrotrons, on the other hand, usually allow the use of continuously tunable radiation ranging from tens to hundreds or thousands of eV. The increased energy range comes at the cost of a reduced energy resolution and the sheer organizational complications of operating a large scale synchrotron facility as opposed to an in-house setup. Evidently, different systems come with their strengths and weaknesses, making them more or less applicable to different problems (table 2.1). As the work presented here has been carried out exclusively at synchrotrons, the remaining discussion will only be concerned with synchrotron radiation.[3]

A synchrotron is a ring shaped particle accelerator for charged particles. In the case of the facilities used in the presented work the accelerated particles are electrons. The charged particles are accelerated through a linear accelerator before they are channelled into the synchrotron storage ring. The storage ring consists of alternating sections of straight linear accelerators and bent segments. The particles are held on a path through the use of magnetic fields in the bent segments and accelerated up to relativistic speeds in the linear segments. A schematic depiction of a synchrotron with the most important components is presented in figure 2.1.

Accelerated charged particles produce radiation. Because the par-

[3]Recently, an additional option for a light source has become available: the free electron laser. It has been employed, for example, in place of a regular laser as the probe beam for time-resolved ARPES [43].

Table 2.1: Differences between properties of lasers and synchrotron radiation.

	laser	synchrotron
energy	fixed	variable
energy range	tens of eV	30 eV to 2000 eV
energy resolution	< 1 meV	~ 1 eV
photon flux	$\sim 10^{15}$ photons per second	$\sim 10^{13}$ photons per second per 0.1 % bandwidth

ticles are moving at relativistic speeds, their emission profile is highly directional, meaning that a very focused beam of radiation is generated. In early synchrotrons, the radiated emissions that was created through the bending magnets that keep the particles on their track was used directly. Modern facilities make use of the more sophisticated method of generating the radiation by use of *undulators*. An undulator is essentially a periodic arrangement of alternating magnetic fields. An electron passing through them will be brought to oscillate with the wavelength of the magnets in the undulator, resulting in coherent emission of photons.

The so created highly focused and intense electromagnetic radiation is directed out of the synchrotron and can be further guided, focused, monochromated, polarized or otherwise tuned by means of different optical elements. The details of the employed optics depend on the desired application. This ability to produce high intensity light over a broad energy spectrum is a major reason for why synchrotron facilities are so versatile and powerful.

Synchrotron experiments have become a core element of research in countless disciplines, such as solid state physics, chip manufacturing and nanofabrication, molecular biology and medicine. It therefore comes

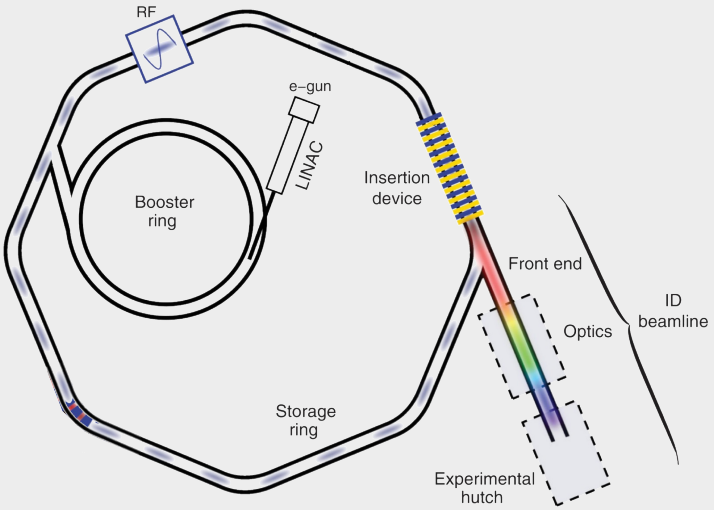

Figure 2.1: Schematic of a synchrotron. Electrons are accelerated through a linear accelerator (LINAC) into a booster ring, where they are further accelerated before being injected into the storage ring. They are kept on their path by use of magnetic fields and held at relativistic velocities through radio frequency (RF) supplies. Insertion devices (ID) such as undulators make use of the electrons to create highly focused beams of radiation that can be used for various applications at different beamlines. Figure adapted from [44].

as no surprise that larger and more powerful facilities are continuously being built. Figure 2.2 shows how the synchrotron *brilliance*, a measure for the number of photons that can be generated by a facility, has increased exponentially over time. Major technical improvements, particularly in the evolution of the insertion devices from bending magnets (1st generation) over wigglers (2nd generation) to undulators

(3rd generation), have allowed these tremendous jumps in performance and similar evolutions are likely to ensure that synchrotron research will continue to play a major role in technological and scientific progress [44].

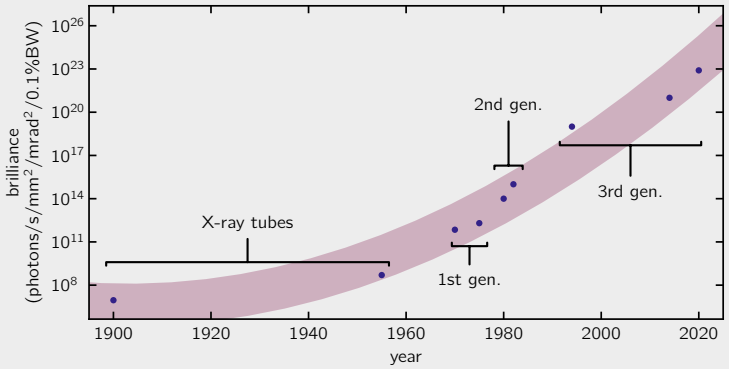

Figure 2.2: Evolution of synchrotron brilliance over time. Figure adapted from [44].

2.2.2 Sample surface

The photoemission process is based on the absorbtion of a photon by an electron inside a sample. The absorbing electron is accelerated and can leave the confines of the material given that its kinetic energy is sufficiently high (cf. also section 2.3). However, the electron may undergo scattering processes on its way out of the sample that could change its track or reduce its energy, making it impossible to infer its original energy-momentum state. Therefore, only the subset of electrons that leaves the sample without any additional scattering can be effectively used to infer properties of the initial state before photon absorption.

The so-called *universal curve* contains information on the average path an electron inside a solid state sample can travel before undergoing a scattering process. This *inelastic mean free path* Λ_e is a function of the electron's kinetic energy and has been experimentally determined and empirically described as depicted in figure 2.3. From this data it becomes clear that the mean free path for electrons expelled in ARPES, where the kinetic energies range from tens of eV to one or two keV, is in the order of a few Å. In other words, the great majority of the electrons that contribute to the signal in an ARPES measurement stem from a region ranging only a few unit cells from the surface. Indeed, one can say that for energies below roughly 200 eV, one mostly probes the outermost unit cell only. ARPES using visible to ultraviolet energies (VUV-ARPES) is thus highly sensitive to the physics at the sample surface. This fact has been made use of in the investiagtion of surface specific physics [45, 46].

The surface sensitivity is somewhat weakend for higher energies, such as in soft x-ray ARPES (SX-ARPES), where the used energies range from hundreds of eV to a few keV. Nevertheless, it is clear that even small variations or perturbations of the material surface, for example through surface oxidation or adhesion of atmospheric molecules, have a critical impact on the measurement. It is this sensitivity that dictates the requirement of a single crystalline sample surface that is kept free from disturbances by being held under UHV conditions.

There are different ways of creating a sufficiently clean surface in the first place. Here, the method of choice for all presented measurements has been the popular *top post cleaving method*. For this procedure, a small metallic post is glued on top of a piece of the material under investiagtion (usually a single crystal with volumes in the mm^3 range) under atmospheric pressure. The so prepared sample is then introduced into the evacuated measurement chamber. Once inside the chamber and under UHV atmosphere, the metallic post is mechanically hit off the sample. In this manner, ideally, a small part of the sample is removed

and a perfectly clean surface remains at the cleaving plane. Evidently, how well this process works or does not work is highly dependent on the crystal structure and the interatomic forces inside the sample. Whether or not it is possible to create a successful cleave with a given material thus becomes a critical factor for the feasability of an ARPES study. Examples of materials that exhibit a strong degree of two-dimensionality and thus cleave easily are layered systems, such as $Bi_{2-x}Pb_{x+y}Sr_{2-y}CuO_{6+\delta}$ (Bi2201) or van-der-Waals materials such as graphene and the transition metal dichalcogenides with chemical formulas MX_2 where M is a transition metal (e.g. Mo or W) and X a chalcogen atom (e.g. S, Se or Te). All of these are made up of flat layers that are stacked on top of each other and held in place by comparatively weak interlayer forces.

For more *three dimensional* crystals it can be much more difficult to obtain such a surface. But through dedication and creativity, new techniques and skills evolve. For the infamously difficult to cleave representant of the cuprate high-temperature superconductors (HTSCs), $La_{2-x}Sr_xCuO_4$ (LSCO), for example, researchers have developed dedicated sample preparation techniques and *tricks* that significantly increased the reproducibility of a cleave. One such method is the use of a specialized sample holder that allows driving a knife-like edge into the crystal just before hitting the top-post [47]. As another example, in chapter 7 we will present data that was taken on the fully three dimensional $CeRu_2Si_2$, where a lot of learning was necessary before a successful experiment could be conducted.

2.2.3 Electron analyzer

The sorting of electrons by energy and momentum is usually achieved through a hemispherical electron analyzer as is depicted in figure 2.4. The central principle is that of two concentric spherical shells of different radii, between which an electric potential difference (the so-called *pass energy* E_{pass}) is applied. Before the electrons enter the area of the

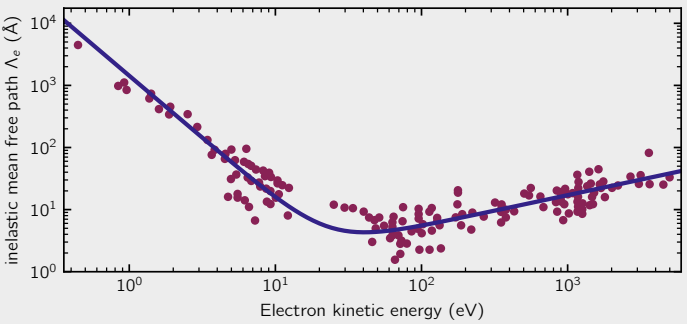

Figure 2.3: Plot of the experimentally determined inelastic mean free path Λ_e as a function of kinetic energy E_{kin} for electrons escaping from condensed matter. The solid line represents a fit of the function $\Lambda_e = A/E_{\text{kin}}^2 + B\sqrt{E_{\text{kin}}}$ with $A = 1430\,\text{Å}\,\text{eV}^2$ and $B = 0.54\,\text{Å}/\text{eV}^{0.5}$. Recreated from [48].

electric field between the hemispheres, they go through a system of electronic lenses for focusing and a linear retarding potential V_r, effectively slowing them down from kinetic energy E_{kin} to $E'_{\text{kin}} = E_{\text{kin}} - eV_r$.

Electrons entering the electric field between the hemispheres are deflected towards the inner sphere. The electron's trajectories depend on the relative amounts of the kinetic energy E'_{kin} at the moment of entering the electric field and the strength of the field E_{pass} itself. If the kinetic energy of the incoming electron is large with respect to E_{pass}, this electron will hit the outer shell. If, on the other hand, E'_{kin} is too small, the electron will collide with the inner shell. Only the subset of electrons with E'_{kin} in a range defined by E_{pass} will travel through the whole hemisphere and make it to the detector at the other end. In this manner, electrons of a given kinetic energy range can be *selected*

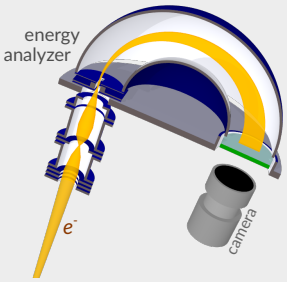

Figure 2.4: Schematic cross section of a hemispherical electron analyzer. Electrons (e^-) enter the analyzer through the entrance slit after having gone through a system of electron lenses and the retardation potential V_r. By applying a voltage between the inner and outer hemispheres, an electric field is generated that guides the electrons onto the detector. The trajectory of an electron depends on the applied voltage and its kinetic energy and momentum. Figure adapted from [49] (CC BY-SA 4.0).

by adjusting E_{pass} and V_r accordingly.[4]

We have seen how electrons with different kinetic energies end up at different radial positions at the outgoing end of the hemispherical analyzer. Similarly, the position at which an electron enters the analyzer through the entrance slit is translated to a polar position on the outgoing end. Since the position along the analyzer entrance slit is a consequence of the electron's momentum, we see that in this manner both energy and momentum are encoded in the position at which the electron leaves the analyzer. This position can be recorded with a suitable detector – usually a charge coupled device (CCD) camera prepended by a microchannel plate for increased detection efficiency – and later translated back into the original energy and momentum information of

[4] As E_{pass} also defines the energy window and is coupled to the energy resolution, one typically uses V_r for the selection of kinetic energy while keeping E_{pass} constant.

the recorded electrons (section 4.1.1).

Commercially available analyzers were used for the experiments presented in this thesis. At most of the visited beamlines an analyser by Scienta [50] is installed. The SX-ARPES measurements conducted at the ADDRESS beamline made use of a model by SPECS^{TM} [51].

2.3 Physical description of the photoemission process

Descriptions of the photoemission process are abundantly present in the literature and in published theses. The depths of these descriptions range from rather brief and concise [42, 52, 53] to more in-depth [39, 54, 55] or with a focus on certain aspects, such as matrix element effects [56] or the spectral function [38]. Here, I therefore do not aim at repeating what has already been said in a better way than I possibly could. Instead, I choose to take a rather brief path towards the elements that are most important to the work presented here: polarization selection rules and Fano resonances.

2.3.1 The photoemission intensity

In simple terms, the photoemission process consists of an electron in a solid in its initial state that interacts with a photon. Through that interaction the electron acquires additional energy and is expelled from the solid into vacuum, reaching its final state. However, strictly speaking one would have to treat the collective of electrons inside the solid as an N particle initial state that interacts with the electromagnetic field of the photon to produce a collective final state. Instead of treating this whole process as one quantum mechanical transition, it has been found to be much more practical to divide the process up into individual segments that can be handled more easily:

1. an electron inside the solid absorbs a photon, gaining kinetic energy,

2. the electron travels through the solid towards the surface and

3. the electron passes the potential barrier and is transmitted into vacuum.

This division constitutes the so-called *three-step model* .

Since the expelled electron gains relatively high kinetic energies and one can safely assume that the remaining electrons quickly rearrange to screen the effective attractive potential of the hole left behind, one usually employs the so-called *sudden approximation* and treats the interacting electron as instantaneously independent of the remaining $N-1$ electron system. The only effect the expelled electron feels is the net periodic potential inside the bulk.

Since the wavelengths of the used photons are orders of magnitude larger than the atomic length scales, a third approximation can be made in that the electromagnetic vector field operator can be taken to be independent of the position $\mathbf{r}$. This *dipole approximation* simplifies the interaction Hamiltonian.

Combined, the mentioned approximations lead to the following expression for the photoemission intensity I as a function of electron momentum $\mathbf{k}$ and energy ω:

$$I(\mathbf{k},\omega) \propto |M_{i,f}|^2 \cdot \mathcal{A}(\mathbf{k},\omega) \cdot f(\omega,T) \quad . \tag{2.1}$$

$f(\omega,T)$ denotes the Fermi-Dirac distribution

$$f(\omega,T) = (1+\exp\left[\beta(\omega-\mu)\right])^{-1} \quad , \tag{2.2}$$

with the chemical potential μ and the Boltzmann factor $\beta = (k_{\mathrm{B}}T)^{-1}$. The Fermi-Dirac distribution reflects the fact that only occupied states can be probed by photoemission. $M_{i,f}$ is the so-called interaction matrix element that gives rise to intensity variations across k-space. It is also at the core of certain selection rules that will be discussed in a later section. $\mathcal{A}(\mathbf{k},\omega)$ is the particle removal spectral function that is introduced in the framework of simplifying the untractable problem of

dealing with a system of many ($\approx 10^{23}$) interacting particles. It can be thought of as the electronic dispersion and is, in essence, what we are usually interested in measuring. A more rigorous definition of $\mathcal{A}$ can be found in section 3.3.2 in equation (3.8).

2.3.2 Selection rules

The matrix element from equation (2.1) essentially constitutes a product of the final state $\langle\phi_f|$, the quantum mechanical vector field $\mathbf{A}$ and momentum $\mathbf{p}$ operators and the initial state $|\phi_\mathrm{i}\rangle$: $M_{i,f} \propto \langle\phi_\mathrm{i}|\,\mathbf{A}\cdot\mathbf{p}\,|\phi_\mathrm{f}\rangle$. This expression mostly depends on the momentum vectors of initial and final states $\mathbf{k}_\mathrm{i}$ and $\mathbf{k}_\mathrm{f}$ as well as that of the incoming photon $\mathbf{k}_{h\nu}$ and its polarization vector $\boldsymbol{\epsilon}$. In this manner, the matrix element can contribute to significant intensity variations throughout k-space. For a thorough discussion on approximative expansions of the matrix element the reader is referred to the excellent review by Simon Moser [56]. Here we focus solely on the effect of the polarization vector $\boldsymbol{\epsilon}$ on $M_{\mathrm{i,f}}$.

The expression $\langle\phi_\mathrm{f}|\,\boldsymbol{\epsilon}\,|\phi_\mathrm{i}\rangle$ is evaluated as an integral over space:

$$M_{i,f} \sim \int_{\mathbb{R}^3} \phi_\mathrm{f}(\mathbf{r})\boldsymbol{\epsilon}\phi_\mathrm{i}(\mathbf{r})\mathrm{d}^3 r \quad . \tag{2.3}$$

The factors in the integrand can have certain symmetry properties. Of particular interest is the reflection with respect to the experimental mirror plane $\mathcal{R}$. This plane is defined by the directions of the incoming photon $\mathbf{k}_{h\nu}$ and the outgoing electron $\mathbf{k}_\mathrm{f}$ (or, in more pragmatic terms, by the origin of the incoming light, the sample position and the analyzer slit), see figure 2.5. Eigenfunctions of $\mathcal{R}$ can have an eigenvalue of $+1$, meaning the reflect perfectly onto themselves, or -1 in which case they reflect exactly on their negation. An eigenfunction fulfilling the former is called *even*, one of the latter case is called *odd*. It turns out that all three factors of the integrand can be eigenfunctions of $\mathcal{R}$ – at least within reasonable approximation: (i) The available polarizations $\boldsymbol{\epsilon}$ at ARPES endstations are usually constructed to be

parallel (π) or perpendicular (σ) to the experimental mirror plane, so the corresponding photons are even or odd, respectively. (ii) For the electron's final state ϕ_f the *free electron final state* approximation has proven to be very practical. Under this approximation, the final state is assumed to be that of a free electron traveling through vacuum within the experimental mirror plane and is thus even. (iii) Finally, the electron's initial state ϕ_i has a symmetry with respect to the crystal lattice. By proper orientation of the sample and depending on the symmetry properties of the electron orbital in question, it may or may not be possible to make it an eigenfunction of $\mathcal{R}$. This forms the basis for making use of the polarization selection rules in ARPES as we will see shortly.

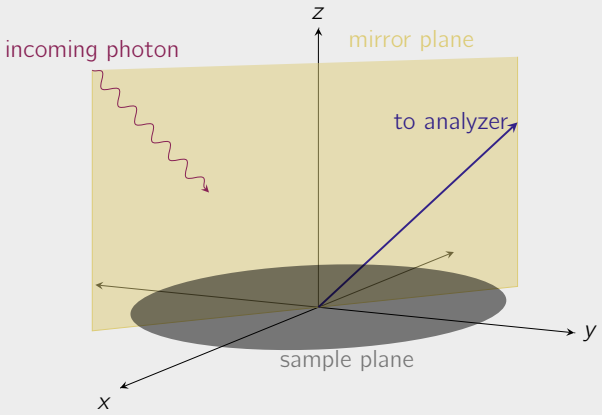

Figure 2.5: Scheme of the experimental mirror plane. It is spanned by the vectors of the incoming photon beam and the one connection the emission location to the center of the electron analyzer.

Having established that the integrand in equation (2.1) can often be made a product of even or odd functions, we remind ourselves of the

simple fact that the integral of an odd function over all of $\mathbb{R}^3$ vanishes because all the parts in the positive domains cancel out those in the negative domains. Since ϕ_f can be taken to be even, as established in the last paragraph, the whole integrand becomes odd if either $\boldsymbol{\epsilon}$ or ϕ_i are odd, but not both at the same time. Whenever we have an odd integrand, $M_{i,f}$ vanishes and with it the ARPES intensity $I(\mathbf{k}, \omega)$ as a whole. Through appropriate arrangement of the sample orientation and the used light polarization $\boldsymbol{\epsilon}$ we can therefore *suppress* specific states in the signal. If employed systematically, these simple selection rules therefore allow extracting information about the symmetry character of the electronic initial state ϕ_i. The selection rules are summarized in table 2.2.

Table 2.2: Summary of the polarization selection rules in ARPES. Since the final state ϕ_f is even, if the product of the initial state ϕ_i and the polarization operator $\boldsymbol{\epsilon}$ happens to be odd we will get a vanishing transition probability $\langle \phi_f | \boldsymbol{\epsilon} | \phi_i \rangle$.

ϕ_i	light polarization	$\langle \phi_f \vert \boldsymbol{\epsilon} \vert \phi_i \rangle$
even	π	$\neq 0$
odd	π	$= 0$
even	σ	$= 0$
odd	σ	$\neq 0$

2.3.3 Fano resonances

The matrix element that appears in the expression for the photoemission intensity described by equation (2.1) can be seen as a measure for the interaction probability between the incoming photon and the ejected electron. As we have seen in the preceding section, there are cases

where this probability drops to zero. There are, however, also situations where this probability is strongly enhanced. Exciting the system at a so-called Fano resonance presents one of these cases, and it is commonly used in photoemission experiments [57].

The Fano resonance is a general consequence of interacting waves and can therefore be encountered in many areas [58]. It arises due to the interference of a discrete excitation mode with a continuum of modes, that are in this context referred to as *background*. A precise mathematical derivation can be found in the original work by Fano [59], which explained the line shape of inelastic electron scattering at He, where two processes interfere: the scattering of the electron at the He atom (background) and the excitation of a He atom with subsequent ejection of an electron through autoionization (discrete). A somewhat intuitive explanation for the effect can be reached if one considers a system of two coupled harmonic oscillators O_1 and O_2, each with their espective eigenfrequency ω_1 and ω_2. We now imagine that one drives oscillator O_1 with an externally applied force at frequency ω. The situation for is depicted schematically in figure 2.6 (a). The equations of motions for the system are

$$\ddot{x}_1(t) = -\omega_1^2 x_1(t) - \gamma_1 \dot{x}_1(t) + k[x_1(t) - x_2(t)] + f(t) \tag{2.4}$$

$$\ddot{x}_2(t) = -\omega_2^2 x_2(t) - \gamma_2 \dot{x}_2(t) + k[x_2(t) - x_1(t)] \quad . \tag{2.5}$$

We are interested in the frequency responses of the two oscillators, so it is useful to Fourier transform the equations:

$$\left[\frac{\mathrm{d}^2}{\mathrm{d}t^2} + \gamma_1 \frac{\mathrm{d}}{\mathrm{d}t} + \omega_1^2 - k\right] X_1(\omega) + kX_2(\omega) = F(\omega) \tag{2.6}$$

$$\left[\frac{\mathrm{d}^2}{\mathrm{d}t^2} + \gamma_2 \frac{\mathrm{d}}{\mathrm{d}t} + \omega_2^2 - k\right] X_2(\omega) + kX_1(\omega) = 0 \quad , \tag{2.7}$$

where the capital letters designate the respective Fourier transforms, $X_i(\omega) = \mathcal{F}x_i(t)$. This system of equations can be solved for the

frequency responses χ_i which works out to:

$$\chi_1(\omega) = \frac{X_1(\omega)}{F(\omega)} = \frac{1}{c_1(\omega)\left(1 - \frac{k^2}{c_1(\omega)c_2(\omega)}\right)} \tag{2.8}$$

$$\chi_2(\omega) = \frac{X_2(\omega)}{F(\omega)} = -\frac{k}{c_2(\omega)}\chi_1(\omega) \tag{2.9}$$

where we introduced the terms

$$c_1(\omega) = \omega_1^2 - \omega^2 + i\gamma_1\omega - k \tag{2.10}$$

$$c_2(\omega) = \omega_2^2 - \omega^2 + i\gamma_2\omega - k \quad . \tag{2.11}$$

Without any coupling between the two oscillators, it is clear that the frequency dependent amplitude of the response of the system will show the typical Lorentzian resonance profile, peaking at $\omega = \omega_1$. For a nonzero coupling and for ω_2 far enough away from ω_1, lying somewhere in the tails of the uncoupled resonance profile, one would find that the resonance of O_2 at ω_2 manifests itself in the total frequency response of the system, see figure 2.6 (b). In this viewpoint, ω_2 can be seen as the *discrete* state, while the continuous *background* spectrum is provided by the tails of the uncoupled resonance profile of O_1.

In the case of photoemission, the continuum of excitations is provided by the usual photoemission process of an electron in the valence band region. In this context, we speak of a continuum because the electron can be photoemitted by every incoming photon energy $h\nu$, as long as it is larger than the binding energy plus the work function: $h\nu >= E_B + e\Phi$. On the other hand, the discrete state here refers to the resonant excitation of a core electron into the valence band and the subsequent photoemission through autoionization. This process has a finite interaction probability only if the excitation energy is close to the energy difference between the core and valence states — but when it does contribute, it enhances the signal significantly thanks to the resonant nature of the transition. The difference between the two processes is schematically depicted in figure 2.7.

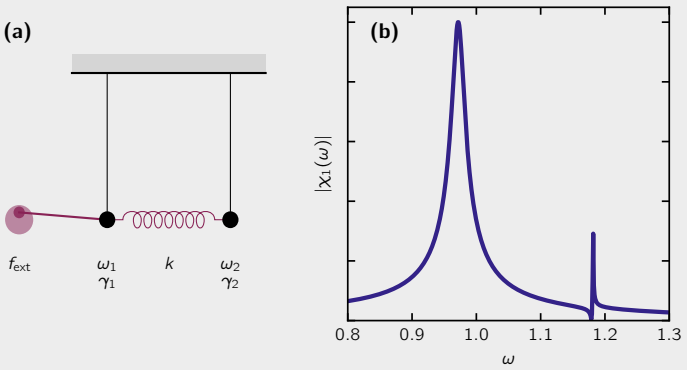

Figure 2.6: Toy model for the explanation of the Fano resonance. **(a)** Drawing of two pendulums coupled by a spring, where the left pendulum can be driven by an external motor. **(b)** Frequency response for this system as given by equation (2.8). The used values are $\omega_1 = 1$, $\omega_2 = 1.2$, $\gamma_1 = 0.02$, $\gamma_2 = 0.0$, $k = 0.05$. The main peak of O_1 is slightly redshifted from $\omega = \omega_1$ due to the coupling. The resonance peak of O_2 manifests itself as a peak in the *background* region of the main peak, near $\omega = \omega_2$. Notice the characteristic line shape that quickly drops to 0 just before reaching the peak.

This fact can be used in photoemission to enhance the relative intensity of certain electronic states [57]. In particular, by tuning the excitation energy to a suitable transition of one of the atoms in a compound, one can enhance the signal of the electronic states that predominantly stem from that atom. This knowledge can provide valuable insights into the origins of the observed band structure. We will make use of this fact in chapter 7.

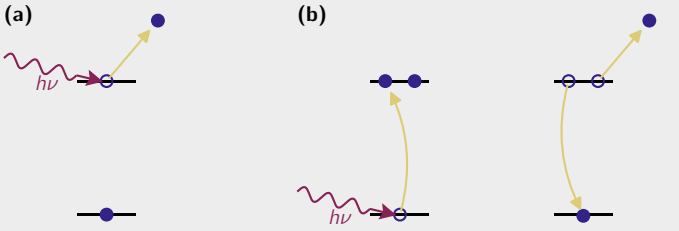

Figure 2.7: Simple schematic diagram of (a) photoemission and (b) resonant autoionization. Two energy levels are drawn, occupied by electrons (blue circles). In the photoemission process (a) the incoming photon with energy $h\nu$ interacts with the electron in the upper energy level, transferring all its energy to it, resulting in the electron being emitted. In (b), the photon interacts with the lower lying electron, allowing it to hop to a different energy state. In a second step, the excited electron relaxes back to its original state, thereby transferring its excess energy (which is again $h\nu$) to another electron that can be photoemitted.

Chapter 3: Review of condensed matter theories

Dealing with systems with astronomically large numbers of particles poses an enormous challenge to physical and computational methodologies. The tremendous efforts at tackling this problem have led to a rich system of theories, each one more sophisticated than the one before, that partly complement and partly build upon each other. In the present chapter we aim at giving a brief overview over a selection the theoretical concepts with a strong focus on the ones that provide the direct basis for work presented in this thesis. Section 3.1 acts as an overall introduction that summarizes the earliest and most commonly used approximations. It directly leads to the description of

density functional theory in section 3.2. Section 3.3 formally introduces the spectral function that is at the heart of angle-resolved photoemission spectroscopy and gives a brief explanation of many-body perturbation theory. The chapter concludes by linking different theoretical viewpoints together at the example of the Kadowaki-Woods ratio.

3.1 The many-body problem

The core problem of solid state physics is that we are dealing with a system of $\sim 10^{23}$ interacting particles – nuclei and electrons. Obviously, this is completely untractable, neither analytically nor computationally. The challenge, therefore, lies in finding reasonable simplifications that open a pathway for solving the problem. A first such simplification is the Born-Oppenheimer or *adiabatic* approximation, that proposes to split up the total wave function of the system into an electronic part that depends on the nuclear and electronic coordinates and a nuclear part which only depends on the nuclear coordinates. The assumption that the nuclear wave function does not depend very much on the electronic coordinates is justifiable since the electronic mass is orders of magnitude smaller than the nuclear mass, especially for larger atoms. This simplified system is, however, still completely untractable.

The Hartree-Fock approximation allows to simplify the problem to a point where it can be solved: A system of non-interacting identical fermions can be described by a properly antisymmetrized linear combination of single particle states. This is exactly provided by a Slater determinant. The ground state for the interacting system should then be given by a superposition of Slater determinants. The idea of the Hartree-Fock approximation instead is to use just one single Slater determinant to describe the state of the interacting system. This simplification leads to a system of equations that can be solved computationally, however the results systematically underestimate the experimentally measured bandwidths of semiconductors. The reason lies in the fact that electronic interactions, while represented in the Hamiltonian, are not encoded in the Slater determinant (only the Pauli principle is) and the information about dynamical correlation is therefore missing.

3.2 The Kohn-Sham equations and the local density approximation

An approach outside the Hartree-Fock approximation is based on the Hohenberg-Kohn theorem, which essentially states that all properties of the system can be described by a unique functional of the *ground state density alone*. This provides the foundation for density functional theory (DFT) wherein the problem of solving the N particle system reverts to finding its ground state density n_0, which is the one that minimizes the system's energy. Kohn and Sham have assumed that for every system of interacting particles, there exists a system of non-interacting ones with the same density. Following this line of thinking led them to a set of equations that can be solved self-consistently, the Kohn-Sham equations:

$$V_i(\mathrm{r}) = V_{\mathrm{ext}}(\mathbf{r}) + \int \mathrm{d}\mathbf{r}' W(\mathbf{r}, \mathbf{r}') \cdot n_i(\mathbf{r}') + V_{\mathrm{xc}}\left([n_i], \mathbf{r}\right) \tag{3.1}$$

$$\left(-\frac{\hbar^2}{2m_{\mathrm{e}}}\nabla^2 + V_i(\mathbf{r})\right) \cdot \phi_n(\mathbf{r}) = \varepsilon_n \phi_n(\mathbf{r}) \tag{3.2}$$

$$n_{i+1}(\mathbf{r}) = \sum_{n=1}^{N} |\phi_n(\mathbf{r})|^2 \tag{3.3}$$

Here, V_{ext} stands for the external potential of the nuclei, W denotes the Coulomb repulsion between electrons, V_{xc} is the so-called exchange correlation energy – a quantum phenomenon with no classical analog – and the ϕ_n denote single particle wavefunctions with their energies ε_n. This system of equations can be solved by assuming a certain starting form of the electron density $n_0(\mathbf{r})$ to find a first approximation for the potential V_0 by using equation (3.1). The electron orbitals ϕ_n can be computed for this V_0 with equation (3.2). These orbitals, in turn, can be used through equation (3.3) to determine a better approximation to the electron desity, n_1. The procedure continues by plugging the

new n_1 into the first equation and going through the same steps again. This can be repeated until the values of the density do not change significantly anymore.

However, V_{xc}, a crucial parameter for this whole calculation, remains unknown. It can be determined exactly for a homogeneous electron gas, but not for the actual, inhomogeneous system. This is where the local density approximation (LDA) comes in. Since the exchange correlation energy can be determined for a homogeneous electron gas and these numerical results can be parametrized as a function of density, they are used in the LDA to approximate the exchange correlation energy for the inhomogeneous system. It is simply assumed that at any point $\mathbf{r}$, the system with *local density* $n(\mathbf{r})$ has a its value for the exchange correlation energy equal to that of a homogeneous system of the same density.

DFT in the LDA provides the foundation for countless electronic structure calculations that have been carried out by the solid state physics community over the years. It is routinely implemented in code bases that allow for such calculations [60, 61] and there exist several extensions, such as the generalized gradient approximation (GGA). It is certainly a hugely successful theory, even though it has its limits. For example, it systematically underestimates the band gaps in semiconductors and is known to have difficulties predicting the levels of f electronic orbitals, as the LDA becomes less applicable with these more localized states. Despite those shortcomings, most approaches that go beyond DFT, such as dynamical mean field theory (DMFT), still rely on it for a first input and it will certainly remain a central element in the collective toolbox of solid state physics.

3.3 Excited electronic states

DFT as described in the preceding section is essentially a theory and methodology for the ground state. Different approaches are necessary in order to describe excitations of the system. One way that has

proven to be very successful for the low energy excitations is Landau's theory of Fermi liquids [62]. Before reviewing the core concept of a Fermi liquid, we are going to focus on a different pathway that is more directly linked to the microscopic processes in photoemission: Green's function approach and many-body perturbation theory (MBPT). The microscopic Green's approach is closely linked to the macroscopic Fermi liquid theory, as we will discuss towards the end of this section.

The goal in MBPT is to describe the response of the full system of electrons to the addition or removal of an electron. The latter is, of course, exactly what we are interested in in photoemission experiments. The excited states are termed quasiparticles (QPs) which can be electron- or hole-derived and their wave functions to quantum number s are denoted as $f_s(\mathbf{x})$. Starting point is the Schrödinger equation

$$\left(-\frac{\hbar^2}{2m}\nabla^2 + V(\mathbf{x}) - E_s\right) f_s(\mathbf{x}) + \int \Sigma(\mathbf{x}, \mathbf{x}'; E_s) f_s(\mathbf{x}') \mathrm{d}\mathbf{x}' = 0 \quad . \tag{3.4}$$

The $\mathbf{x}$ contain the space and spin coordinates. V denotes the static potential of the ions and E_s the energy eigenvalue. The new quantity Σ is the so-called self-energy. It is meant to contain the net effect of all the statistical and dynamical correlations [including, among other things, V_{XC} from equation (3.1)] and is a priori unknown. One could say that we are packing everything we are not really able to describe into this new term. In some sense this means that we are transforming the problem of the many-body system to that of finding reasonable approximations to the self-energy.

3.3.1 The spectral function

Equation (3.4) can be tackled by using a Green's function approach. This means that we look for a function $G(\mathbf{x}, \mathbf{x}'; E)$ which satisfies

$$\left(-\frac{\hbar^2}{2m}\nabla^2 + V(\mathbf{x}) - E\right) G(\mathbf{x}, \mathbf{x}'; E) \quad + \\ \int \Sigma(\mathbf{x}, \mathbf{x}''; E) G(\mathbf{x}, \mathbf{x}''; E) \mathrm{d}\mathbf{x}'' = -\delta(\mathbf{x} - \mathbf{x}') \quad . \quad (3.5)$$

$G(\mathbf{x}, \mathbf{x}'; E)$ represents the response of the system to an infinitesimal perturbation. Through a series of considerations (see equations (C.1) to (C.12)) it can be shown that a form like

$$G(\mathbf{x}, \mathbf{x}'; E) = \sum_s \frac{f_s(\mathbf{x}) f_s^*(\mathbf{x}')}{E - \varepsilon_s + i\Delta\,\mathrm{sgn}(\varepsilon_s - E_\mathrm{F})} \quad (3.6)$$

satisfies section 3.3.1 and therefore fulfills the requirements for a Green's function. In equation (3.6), ε_s denotes the excitation energy, that is the difference from the ground state to the state with an additional/removed particle and the f_s are the QP amplitudes. E_F is the Fermi energy and Δ represents an infinitesimal that is added in order to formally reach convergence. Confer section C.1 for more details. One can rewrite this in the so-called spectral representation

$$G(\mathbf{x}, \mathbf{x}'; E) = \oint_{\mathbb{C}} \mathrm{d}E' \frac{\mathcal{A}(\mathbf{x}, \mathbf{x}'; E')}{E - E'} \quad (3.7)$$

where we have introduced the *spectral function*

$$\mathcal{A}(\mathbf{x}, \mathbf{x}'; E) = \sum_s f_s(\mathbf{x}) f_s^*(\mathbf{x}') \delta(E - \varepsilon_s) \quad . \quad (3.8)$$

The spectral function $\mathcal{A}$ is the same object we have encountered in section 2.3 in equation (2.1). $\mathcal{A}$ essentially represents what is measured in a photoemission experiment and we therefore have a strong

motivation to find concrete expressions for it that can be used to model the photoemission intensity. In order to reach such an expression, we first provide an alternate relation between G and $\mathcal{A}$ that results from carrying out the contour integral in equation (3.7):

$$\mathcal{A}(\mathbf{x}, \mathbf{x}'; E) = -\frac{1}{\pi} \operatorname{sgn}(\varepsilon_s - \mu) \operatorname{Im} G(\mathbf{x}, \mathbf{x}'; E) \quad . \tag{3.9}$$

Next, we realize that it is more natural to express G and $\mathcal{A}$ in terms of the principal quantum number n and the QP momentum vector $\mathbf{k}$ instead of the space and spin coordinates $\mathbf{x}$. The results of MBPT then lead to

$$G(n, \mathbf{k}; E) = \frac{1}{E - \varepsilon_{n,\mathbf{k}} - \operatorname{Re}\Sigma(n, \mathbf{k}; E) - i \operatorname{Im}\Sigma(n, \mathbf{k}; E)} \quad , \tag{3.10}$$

which diverges for energies

$$E_n(\mathbf{k}) = \varepsilon_{n,\mathbf{k}} + \operatorname{Re}\Sigma[E_n(\mathbf{k})] + i \operatorname{Im}\Sigma[E_n(\mathbf{k})] \quad . \tag{3.11}$$

The interpretation of equation (3.10) is that the system has decaying excitations at the complex energies $E_n(\mathbf{k})$ with the energy peak shifted by $\operatorname{Re}\Sigma$ with respect to the unperturbed case $\varepsilon_{n,\mathbf{k}}$ and an inverse lifetime proportional to $-\operatorname{Im}\Sigma$. Note the implicit nature of equation (3.10): in order to find the excitation energies $E_n(\mathbf{k})$ we have to evaluate the (a priori unknown) self-energy *at the excitation energy itself*. In order to overcome this, one usually assumes that the real part of the self-energy varies slowly and that the real part can therefore be expanded around the unperturbed energy $\varepsilon_{n,\mathbf{k}}$

$$\operatorname{Re}\Sigma(E_n(\mathbf{k})) \approx \operatorname{Re}\Sigma(\varepsilon_{n,\mathbf{k}}) + (E - \varepsilon_{n,\mathbf{k}}) \left.\frac{\partial \Sigma}{\partial E}\right|_{E=\varepsilon_{n,\mathbf{k}}} \quad . \tag{3.12}$$

We now introduce the *dynamical renormalization factor* $Z_{n,\mathbf{k}}$,

$$Z_{n,\mathbf{k}} = \left(1 - \left.\frac{\partial \operatorname{Re}\Sigma}{\partial E}\right|_{E=\varepsilon_{n,\mathbf{k}}}\right)^{-1} \quad , \tag{3.13}$$

which can be interpreted as a measure of interaction strength. $Z = 1$ corresponds to no electronic interactions, while for $0 < Z < 1$, a smaller value of Z indicates a stronger correlations. With Z we can write

$$G(n, \mathbf{k}; E) = \frac{Z_{n,\mathbf{k}}}{E - \varepsilon_{n,\mathbf{k}} - Z_{n,\mathbf{k}} \left[\mathrm{Re}\,\Sigma(\varepsilon_{n,\mathbf{k}}) + i\,\mathrm{Im}\,\Sigma(\varepsilon_{n,\mathbf{k}})\right]} \quad . \tag{3.14}$$

And finally, by use of equation (3.9) we find the desired expression for the spectral function:

$$\mathcal{A}(n, \mathbf{k}; E) = \frac{1}{\pi} \frac{Z_{n,\mathbf{k}}^2\,\mathrm{Im}\,\Sigma(\varepsilon_{n,\mathbf{k}})}{\left[E - \varepsilon_{n,\mathbf{k}} - Z_{n,\mathbf{k}}\,\mathrm{Re}\,\Sigma(\varepsilon_{n,\mathbf{k}})\right]^2 + \left[Z_{n,\mathbf{k}}\,\mathrm{Im}\,\Sigma(\varepsilon_{n,\mathbf{k}})\right]^2} \quad . \tag{3.15}$$

In order to get an understanding for these results, it is instructive to discuss the case of a non-interacting system, characterized by a vanishing self-energy, $\Sigma = 0$. In this situation, removing or adding an electron from or to the system would not affect the remaining electrons. The corresponding energies, as given by equation (3.11), are just the *bare band* energies $\varepsilon_{n,\mathbf{k}}$, as given by a DFT calculation in the LDA. The spectral function in this case reverts to a delta function at the $\varepsilon_{n,\mathbf{k}}$ and the (angular) photoemission spectrum simply shows peaks at the respective energy (and $\mathbf{k}$) values. For more general cases, the practical effect of the self-energy on the obtained angle-resolved photoemission spectroscopy (ARPES) spectra is that the real part $\mathrm{Re}\,\Sigma$ shifts the energy level of the peaks, while the imaginary part $\mathrm{Im}\,\Sigma$ leads to a broadening.

An important property of the self-energy Σ should be noted here. Since Σ is effectively a response function, its real and imaginary parts are linked by Kramers-Kronig relations, as is fundamentally true for response functions obeying causality. Concretely, this means that the

following equations hold:

$$\begin{aligned} \mathrm{Re}\,\Sigma(E) &= \frac{1}{\pi}\mathcal{P}\int_{-\infty}^{\infty}\frac{\mathrm{Im}\,\Sigma(E')}{E'-E}\mathrm{d}E' \\ \mathrm{Im}\,\Sigma(E) &= -\frac{1}{\pi}\mathcal{P}\int_{-\infty}^{\infty}\frac{\mathrm{Re}\,\Sigma(E')}{E'-E}\mathrm{d}E' \quad . \end{aligned} \tag{3.16}$$

These relations principally allow the construction of either the real or imaginary parts of the self-energy from the knowledge of the other. Alternatively, fulfilling the Kramers-Kronig relation can be seen as a criterion that any model or experimentally determined result for the self-energy must fulfill.

3.3.2 Many-body perturbation theory

The core problem of equations (3.14) and (3.15) is that the shape of the self-energy is still unknown. One way to find it, is by means of a perturbative approach, where the effects of the self-energy are treated as a small deviation from the non-interacting case. In practice, this amounts to considering higher order scattering terms in the total Green's function. For example, to first order, in addition to the unperturbed propagation of an electron, two scattering processes have to be considered: Coulomb scattering with another electron, whereby some momentum transfer occurs and the generation of an electron–hole pair. It turns out that if only first order terms are considered, this approach is equivalent to the Hartree-Fock approximation that was mentioned in section 3.3. Higher order terms will include repeated combinations of these two elementary processes. The number of processes to consider is already quite large (> 10) at second order, making this task increasingly difficult. In the *random phase approximation* only one of these processes — the one that is considered to be dominant — is taken at every order.

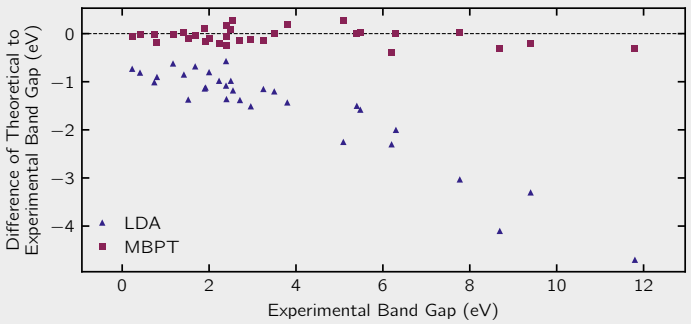

Figure 3.1: Calculated versus experimentally determined band gaps for 31 different semiconducting materials. The LDA values consistently underestimate the band gap, as can be seen by their deviation from the horizontal line at 0. The MBPT values for the same compounds all end up in near perfect agreement with the measurements. In particular, the remaining deviations are of statistical instead of systematic nature. Figure adapted from [63] wherein the used data and references for the theoretical and experimental values can be found.

Such calculations have provided a significant improvement over the LDA results for many semiconducting materials [63], as is showcased in figure 3.1. Despite its successes, like any approximation, MBPT has its limitations. It fails in the case of very large interaction strengths. For exapmle, the Mott insulating state, which is purely due to strong correlations, is not explained by MBPT. It also tends to incorrectly predict the location or appearance of satellite peaks [64].

3.3.3 Connection to Fermi liquid theory

We will now briefly review some of the core ideas in Landau's Fermi liquid theory. This will give us the foundation to show how it is connected to the concepts of the spectral function and the self-energy that were just discussed, and how this opens the door for testing the theory experimentally and for measurements of the contained parameters.

The core idea of the macroscopic Fermi liquid theory [62] is that all states of the interacting system have a direct counterpart in the non-interacting system, the ideal Fermi gas. One can reach the states of the interacting system by starting from the non-interacting one and *adiabatically* turning on the interactions. This implies that the number of states remains conserved and therefore *a priori* excludes phenomena like superconductivity. Furthermore, the scattering events that are considered within this framework can only occur between particles in an energy window of $\pm k_B T$ around the Fermi level and have to adhere to momentum conservation. These facts restrict the validity of the theory to low temperatures and low binding energies.

It is found that the net effect of all the interactions is for the electrons to behave as if they were non-interacting (free) particles with a renormalized energy, finite lifetime and an *effective mass* m^*: QPs. The effective mass is given through the Fermi velocity,

$$v_F = |\nabla_{\mathbf{k}} \varepsilon_{\mathbf{k}}|_{\mathbf{k}=\mathbf{k}_F} = \frac{\mathbf{k}_F}{m^*} \quad . \tag{3.17}$$

Notice that m^* is in general not a scalar quantity but rather a tensor with energy and $\mathbf{k}$ dependence.

Expectations for the macroscopic observables can be derived for such a system of Fermi liquid QPs. The electronic specific heat of a Fermi liquid C scales with temperature T while its resistivity is proportional to T^2 [equations (3.20) and (3.21)] below an energy scale ω_c. In the limit $k_B T \ll \omega_c$, the Wiedemann-Franz law [65] dictates a fundamental relation between heat and charge conduction. Under sufficiently strong electron correlation ($\omega_c \to 0$), the Fermi liquid

concept breaks down and is replaced with a Mott insulating or non-Fermi liquid state. Studying this breakdown route is an important step to conceptualize non-Fermi liquids that are often found in the context of unconventional superconductivity [66–69].

We see that in both, the microscopic approach and the macroscopic Fermi liquid theory, we end up containing the net effect of the interactions in one term: $\Sigma(\mathbf{k}, E)$ and $m^*(\mathbf{k}, E)$ respectively. It is therefore natural to think that a link between these quantities should exist. Indeed, it can be shown that in the vicinity of the Fermi level E_F

$$\frac{1}{m^*} = \left[\frac{1}{m} + \frac{1}{\hbar^2 k_\mathrm{F}} \left.\frac{\partial \,\mathrm{Re}\,\Sigma(\mathbf{k}, E_\mathrm{F})}{\partial \mathbf{k}}\right|_{\mathbf{k}=\mathbf{k}_\mathrm{F}}\right] \cdot Z_{\mathbf{k}_\mathrm{F}} \quad , \tag{3.18}$$

i.e. $m^* \propto Z^{-1}$. From this follows an expression for the self-energy that describes a Fermi liquid:

$$\Sigma_\mathrm{FL}(\mathbf{k}, E) = \alpha(\mathbf{k})E + i\beta(\mathbf{k})[E^2 + (\pi k_\mathrm{B} T)^2] \quad . \tag{3.19}$$

In practice, one often makes the additional assumption that the $\mathbf{k}$ dependence of the self-energy is small and can approximately be ignored. Such a Fermi liquid is called *local* and the considerations in the following sections will be based on a local Fermi liquid, unless stated otherwise.

Experimental ARPES spectra can be fitted in order to determine the parameters in equation (3.19) (see section 4.2) which in turn, through Fermi liquid theory, relate to macroscopic quantities such as the electronic specific heat or the resistivity. Indeed, the self-energy is closely linked to experimental observables, as we shall try to sketch in the following.

Kadowaki-Woods ratio

We are interested in the coefficients A and γ that are found in the expressions for resistivity and electronic specific heat of a Fermi liquid,

respectively:

$$\rho(T) = \rho_0 + AT^2 \tag{3.20}$$

$$c_{\text{el}}(T) = \gamma T \quad . \tag{3.21}$$

Rice first observed that the ratio A/γ^2 (now called the Kadowaki-Woods ratio) appeared to be a constant for many transition metals [70]. Almost 20 years later, after the discovery of heavy fermion systems, Kadowaki and Woods proposed that A/γ^2 was also a constant for members of the heavy fermion family — though a different one than that for the transition metals [71]. Similar behaviour is, however, not observed for other material classes such as the oxides or organic compounds. And even some heavy fermion compounds do not seem to follow the rule. The situation is depicted in figure 3.2 (a).

However, the following highly simplified arguments would actually suggest that a more universal relation between A and γ could be expected to exist. Loosely speaking, the resistivity ρ is linked to the scattering rate of QPs in a material, which is the inverse of their lifetime τ. The inverse lifetime, on the other hand, is proportional to the imaginary part of the self-energy:

$$\rho \propto A \propto \tau^{-1} \propto \operatorname{Im}\Sigma \quad . \tag{3.22}$$

Similarly, the electronic specific heat is proportional to the effective mass m^*, and through equation (3.18) we therefore get a connection between γ and the dynamical renormalization factor Z:

$$c_{\text{el}} \propto \gamma \propto m^* \propto Z^{-1} \quad . \tag{3.23}$$

Additionaly, the real and imaginary parts of the self-energy are connected through the Kramers-Kronig relation, equation (3.16).

With such a level of interconnectedness between the different coefficients one could be tempted to think that there should be a unifying relation. Indeed, in 2009 another attempt at finding such a ratio eventually succeeded. Jacko, Fjærestad and Powell rescaled the A/γ^2

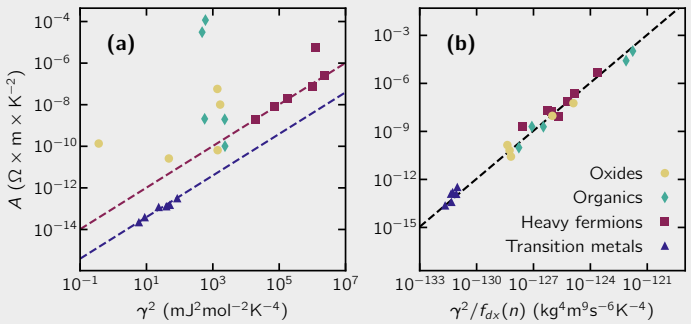

Figure 3.2: Kadowaki-Woods ratio. **(a)** Plot of the squared coefficient γ of the electronic susceptibility against the coefficient A of the linear term in the resistivity for representatives of different material classes. Dashed lines indicate the constant ratios of A/γ^2 suggested by Rice for transition metals and Kadowaki and Woods for heavy fermion systems. Some compounds do not seem to follow the constant A/γ^2 law. **(b)** By applying a scaling $f_{dx}(n)$ that takes into account the system's dimensionality, electron density and the interlayer spacing Jacko, Fjærestad and Powell were able to show that $Af_{dx}(n)/\gamma^2$ appears to be a universal constant across different material families. Figure recreated after [72].

ratio by a factor $f_{dx}(n)$ that depends on the system's dimensionality, its electron density and the interlayer spacing (for layered system). The result is depicted in figure 3.2 (b), where all the compounds across four different classes of correlated materials nicely fall on the proposed line — despite the fact that A and γ^2 vary over many orders of magnitude.

Chapter 4: ARPES data treatment and analysis

Angle-resolved photoemission spectroscopy (ARPES) is a fascinating experimental technique, both from the physical and technical points of view, as elaborated upon in chapter 2, but also in terms of the practical experience for the experimenter. The process of planning, preparing and carrying out an experiment at a synchrotron is certainly rather unique and exciting. Finishing the experiment, however, just signifies the beginning of the next challenge: The collected data awaits being sifted through, visualized and analyzed such that meaningful physical statements can be extracted and novel insights be gained. The amount of treatment and processing

involved in ARPES data analysis is rather large and many technical and physical aspects have to be considered.

The present chapter aims at giving a thorough review of the steps that are required to transform the arrays of numbers obtained at the measurement station into a meaningful picture. Section 4.1 reviews the typical processing routines of angle to conversion, energy correction, background subtraction and band tracing and discusses some technicalities involved with those. Principles of the analysis for the prominent case of extraction of the self-energy from ARPES spectra is described in section 4.2. The chapter closes with section 4.3, where a discussion about the importance of fast data visualization in synchrotron science and other fields precedes the presentation of the `data-slicer` package, a software tool I have developed during my PhD studies to account for just that need. Results and contents of the latter section have been published in a peer-reviewed journal [5].

4.1 ARPES data treatment

The principle of an electron analyzer as described in section 2.2.3 allows separating photoelectrons according to their kinetic energies and momentum components. However, the event that is actually measured is the impact of an electron on a pixel of the charge coupled device (CCD) camera. The task of the experimenter is it then to translate these pixel coordinates to the corresponding $(E, k_{\|})$ values. The basics of these transformations are explained in the following.

4.1.1 Conversion of photoemission angle to momentum

Photoelectron momentum

Within the three-step model (section 2.3.1) the photoelectron goes through three distinct states: the bound state before photon absorbtion, the plane wave travelling towards the material surface with wave vector $\mathbf{k}_0$ and energy E_0 and the free electron plane wave in vacuum with wave vector $\mathbf{k}_1$ and energy E_1. The bound state absorbs the full energy $h\nu$ and momentum of the photon. However, the photon momentum is negligibly small in this situation.[1] The energetic price for leaving the bound state is the sum of the state's binding energy E_B and the material's work function $e\Phi$. Consequently, the final, free electron's kinetic energy is given by

$$\begin{aligned} \frac{\hbar^2 \mathbf{k}_1^2}{2m} &= E_1 = h\nu - E_B - e\Phi \\ \Rightarrow k_1 &= \frac{\sqrt{2m}}{\hbar}\sqrt{h\nu - E_B - e\Phi} \quad . \end{aligned} \tag{4.1}$$

Before the electron leaves the crystal surroundings it was embedded in the crystal's potential, which it has to traverse before leaving the potential to vacuum. One could expect that travelling through the

[1] The photon momentum needs to be considered in the case of the higher photon energies used in soft x-ray ARPES (SX-ARPES).

crystal potential and then escaping through the sample surface, which presents a nontrivial electrostatic situation, to a suddenly potential-free region would generally affect the electron's trajectory. It turns out, however, that this process can be satisfactorily modeled by a constant *inner potential* V_0 that drops to zero at the sample surface as a step-function [39]. Traversing this inner potential step then just comes at the additional cost V_0:

$$E_1 = E_0 - V_0 \quad . \tag{4.2}$$

Importantly, the momentum component parallel to the sample surface is conserved in this process. Leaving the crystal and passing the inner potential step therefore only affects the perpendicular momentum component:

$$k_{1,\parallel} = k_{0,\parallel} \tag{4.3}$$

$$k_{1,\perp} = \sqrt{k_{0,\perp}^2 - \frac{2mV_0}{\hbar^2}} \quad . \tag{4.4}$$

In angle-resolved photoemission spectroscopy (ARPES) we measure the angles θ_k along the analyzer slit from which we can reconstruct the momentum vectors in the lab frame as

$$\mathbf{k}_1^{\text{lab}} = k_1 \begin{pmatrix} \sin\theta_k \sin\gamma_0 \\ \sin\theta_k \cos\gamma_0 \\ \cos\theta_k \end{pmatrix} \quad , \tag{4.5}$$

with γ_0 referring to the angle of the analyzer slit with respect to the experimental mirror plane that is defined in section 2.3.2 of chapter 2. $\gamma_0 = 0°$ corresponds to the *horizontal* geometry, depicted in figure 4.1, while in the *vertical* geometry we have $\gamma_0 = 90°$. These vectors now have to be transformed to the sample coordinate system.

Rotation to the sample frame

A typical ARPES geometry is depicted in figure 4.1, where the sample is imagined to be located at the center of the coordinate axes. In the following we will denote the coordinate system of the lab frame as X with axes x, y and z and the coordinate system of the sample as X'' with axes x'', y'' and z''. The singly primed coordinate system X' represents an intermediate frame that we will be introduced shortly.

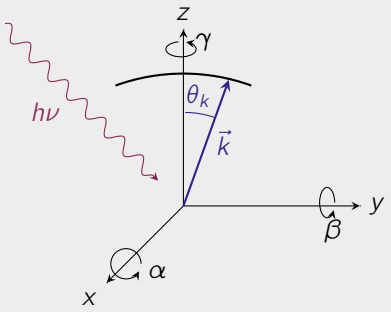

Figure 4.1: The experimental geometry. The mirror plane defined by the incoming photon and the outgoing electron with wave-vector $\vec{k}$ is the yz plane in this example. Here, the analyzer slit is oriented in this plane, therefore this is the *horizontal* analyzer slit geometry.

The manipulator allows rotations about three axes. The first one is the rotation about the x axis by angle α. Notice that naming conventions differ from beamline to beamline (cf. table 4.1). This first rotation is independent of the other two. *Independent* here means that, irrespective of the state of the other two angles, we always rotate around the original x axis, perpendicular to the experimental mirror plane (see figure 2.5 and the containing section). The other two rotations are dependent on α and each other, meaning that their respective axis of rotation will generally deviate from the original coordinate axes of

system X. The angle of rotation around the current y axis will be called β in the following. In the horizontal analyzer slit geometry, this is what is changed in order to record a k-space map. Finally, the rotation about the current z' axis is often called the *azimuth* or ϕ, while for consisteny we will call it γ here. It is worthwile to note that in ARPES, rotations about γ correspond to k-space rotations about the same angle.

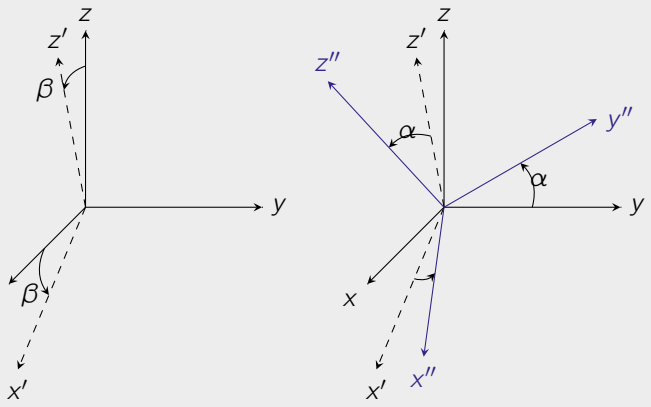

Figure 4.2: The first rotation of β about the y axis (left) and the second rotation of α about the original x axis (right), leading to the sample coordinate system Σ''.

In order to convert the measured vectors of equation (4.5) from the lab to the sample frame we start by first rotating the coordinate system by the angle β around the y axis (figure 4.2, left). The result is, that we find ourselves in the intermediate sample frame X'. In a second step, we then rotate by α around the original x axis (figure 4.2, right). Alternatively, one could first rotate by α around x and then by β around the new y' axis, but mathematically this turns out to

be the same: $R_{y'}R_x = R_xR_yR_x^{-1}R_x = R_xR_y$. Note that we do not need to explicitly worry about the azimuthal rotation γ. As mentioned before, azimuthal rotations follow a correspondence between real and reciprocal space: No matter what frame we are in, γ always signifies a rotation about the *current* z (or z' or z'') axis.

In order to express $\mathbf{k}^{\text{lab}}$ in the sample frame, we have to apply the inverse transformation to it. The calculation can be found in section C.2 of appendix C. This evaluates to

$$\begin{aligned}
k_{1,x}^{\text{sample}} =& k_1(\sin\theta_k \sin\gamma_0 \cos\beta \\
&- \sin\theta_k \sin\alpha \sin\beta \cos\gamma_0 \\
&+ \cos\theta_k \cos\alpha \sin\beta) \\
k_{1,y}^{\text{sample}} =& k_1(\sin\theta_k \cos\alpha \cos\gamma_0 \\
&+ \cos\theta_k \sin\alpha) \\
k_{1,z}^{\text{sample}} =& k_1(-\sin\theta_k \sin\beta \sin\gamma_0 \\
&- \sin\theta_k \sin\alpha \cos\beta \cos\gamma_0 \\
&+ \cos\theta_k \cos\alpha \cos\beta) \quad .
\end{aligned} \tag{4.6}$$

Finally, we need to consider the effect of the inner potential as in equation (4.4):

$$\mathbf{k}_0^{\text{sample}} = \begin{pmatrix} k_{1,x}^{\text{sample}} \\ k_{1,y}^{\text{sample}} \\ \sqrt{(k_{1,z}^{\text{sample}})^2 + 2mV_0/\hbar^2} \end{pmatrix} \quad . \tag{4.7}$$

Simplifications for concrete geometries

For the horizontal analyzer slit geometry that is depicted in figure 4.1 with the slit in the yz plane (which here constitutes the experimental

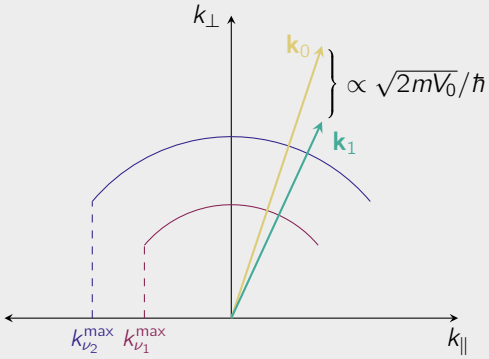

Figure 4.3: Schematic of pertinent k-space vectors. The right half shows how the momentum changes from $\mathbf{k}_0$ to $\mathbf{k}_1$ when passing the inner potential step. Notice how the parallel component is conserved. The smaller red and larger blue arcs indicate the shell of $\mathbf{k}$ vectors that is probed for different photon energies $h\nu$. The $k_\nu^{\max}$ demonstrate how larger photon energies allow probing larger areas in k-space. Here $h\nu_2 > h\nu_1$.

mirror plane) we have that $\gamma_0 = 0$ and the result of equations (4.6) and (4.7) simplifies:

$$\mathbf{k}_0^{\text{sample}} = \begin{pmatrix} k_1 \sin\beta \cos(\alpha + \theta_k) \\ k_1 \sin(\alpha + \theta_k) \\ \sqrt{[k_1 \cos\beta \cos(\alpha + \theta_k)]^2 + 2mV_0/\hbar^2} \end{pmatrix} . \tag{4.8}$$

For the vertical geometry, where the analyzer slit lies in the xz plane, perpendicular to the experimental mirror plane, the crystal momentum

can be found as

$$\mathbf{k}_0^{\text{sample}} = \begin{pmatrix} k_1[\sin\theta_k \cos\beta + \cos\theta_k \cos\alpha \sin\beta] \\ k_1 \cos\theta_k \sin\alpha \\ \sqrt{k_1^2[\cos\theta_k \cos\alpha \cos\beta + \sin\theta_k \sin\beta]^2 + 2mV_0/\hbar^2} \end{pmatrix} \tag{4.9}$$

In this case, the data files come as a function of β, with a different α for each slice of a map, as opposed to the horizontal geometry.

Azimuth

The azimuthal rotation $R_z(\gamma)$ could have been included in all these calculations. It turns out, however, that $R_{z''}R_{y'}R_x = R_xR_yR_z$, so if we want to account for some azimuthal rotation, we can simply multiply our converted $\mathbf{k}_0^{\text{sample}}$ with $R_z^{-1}(\gamma)$ — there is no additional warping or bending introduced through the azimuth.

Table 4.1: Naming conventions at different beamlines (may be out of date or otherwise faulty – use at your own risk). The analyzer position defines whether the polarizations linear horizontal (LH) and linear vertical (LV) refer to even and odd mirror symmetry or vice versa.

Beamline	analyzer slit	α	β	γ	analyzer pos.
SIS	horiz.	theta	tilt	phi	horiz.
ADRESS	horiz.	theta	tilt	azimuth	vert.
I05	vert.	polar	tilt	azimuth	horiz.
CASSIOPEE	vert.	theta	tilt	phi	horiz.
MAESTRO	both	alpha	beta	phi	vert.

4.1.2 Adjustment of the energy levels

In principle, it should be possible to calculate the trajectories of photoelectrons of different kinetic energies from the geometry and field strength inside the electron analyzer. In order to translate kinetic into binding energies relative to the Fermi level E_F, however, the usually unknown value of the work function has to be included in the calculation. It is therefore more practical to determine the Fermi level by comparison to a reference measurement.

The reference is obtained by repeating a scan with identical parameters as are used for the measurement of the sample at a polycrystalline metallic piece (usually Cu or Au) that is in electrical and thermal contact with the sample under investigation and therefore has the same temperature and the same value for E_F. Since it is polycrystalline, we expect an isotropic distribution of spectral weight below E_F, i.e. with no angular (k) dependence. More precisely, the occupation of energy levels should follow the Fermi-Dirac distribution for Fermions [equation (2.2)]. The strategy to determine the position of E_F for every angular channel is therefore to fit each energy distribution curve (EDC) to the Fermi-Dirac distribution of the right temperature. In order to mimick the effect of the finite resolution of the detection system, one convolves the Fermi-Dirac distribution with a Gaussian bell curve. The standard deviation σ of this Gaussian bell curve is proportional to the instrumental resolution. Furthermore, since inelastic scattering typically leads to a growing contribution of background counts with increasing binding energy (see section 4.1.3), it is helpful to model this by allowing for a linear slope below E_F. In total, the fit function we use in order to determine the Fermi level from reference EDCs is

$$\mathrm{fit}(E, E_F, T, \sigma, m) = (f * g_\sigma)(E, E_F, T, \sigma) + \Theta(E_F - E) \cdot m \cdot E \quad (4.10)$$

where

$$f(E, T, E_F) = (1 + \exp[\beta \cdot (E - E_F)])^{-1} \tag{4.11}$$

$$\beta = (k_B T)^{-1} \tag{4.12}$$

$$g_\sigma(E) = \exp\left[-\frac{1}{2}\left(\frac{E}{\sigma}\right)^2\right] \tag{4.13}$$

$$\Theta(E_F - E) = \begin{cases} 0, & \text{if } E > E_F \\ 1, & \text{otherwise} \end{cases} . \tag{4.14}$$

By fitting this function to every EDC of a reference spectrum we obtain the Fermi energy as a function of angular (k) channel. This distribution contains some noise due to the uncertainty in the fit. It is therefore common to either employ a polynomial fit to this distribution or to smoothen it by means of a box-filter or similar smoothing procedures. The now continuous Fermi energy versus angle (k) distribution is used to correct the Fermi level in every channel. The full Fermi level adjustment procedure is illustrated and explained in figure 4.4.

4.1.3 Background subtraction

In virtually all spectroscopy methods, the obtained data contains an intrinsic and extrinsic background. As an example, for the cuprates, it has been demonstrated that these background contributions have significant dependencies on binding energy [73]. In fact, the background at binding energies of 1 eV might be an order of magnitude larger than at or near the Fermi level. For comparison of band structures across a wide range of binding energy, it can be useful to subtract the background intensity.

Of course, different possibilities for modeling the background exist. One of the *classics* is a background construction methodology first proposed by Shirley [74]. Besides a trivial determination of detector

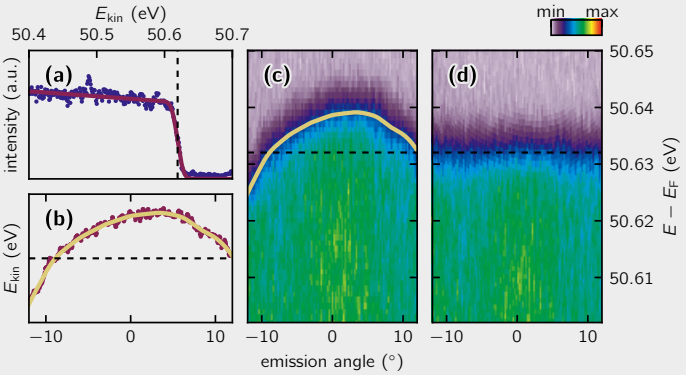

Figure 4.4: Illustration of the Fermi level fitting procedure. **(a)** The points represent an example EDC extracted from the reference spectrum shown in (c). The red line is a fit of the function in equation (4.10) to the data points. From this fit, the value of E_F is determined for this angular channel (dashed line). **(b)** The extracted values of E_F for every angular channel are plotted as points. The line is the result of applying a box-filter smoothing algorithm. The dashed line represents the reference energy that is used as the Fermi energy. **(c)** Raw reference spectrum from a Au sample. One can see that the transition from occupied to unoccupied levels occurs at different y (energy) coordinates for every angular channel. The full and dashed lines are the same as in (b). **(d)** Energy-adjusted Au spectrum. Each angular channel has been shifted according to the difference between the full and dashed lines in (c) with the result that we have a straight Fermi edge at the dashed line.

noise by averaging the intensity in a region of no physical signal (e.g. above E_F), the method suggests that the remaining background signal is mainly due to inelastic scattering. The amount of electrons that can be inelastically scattered at a given energy E is proportional to the integrated density of states (DOS) above E. In other words, the higher energy electrons can potentially be scattered and contribute to

the signal at lower energies, but the lower energy electrons will not appear as background at higher energies — at least not through first-order inelastic scattering processes. Within this model, the background subtracted intensity is found through the implicit equation

$$I_{n+1}(E) = I_n(E) - I_{n+1}(E = E_0) \cdot s \cdot \int_E^\infty I_n(E')\mathrm{d}E' \quad . \qquad (4.15)$$

Here, E_0 is at an energy where no signal is expected and s is chosen such that the converged intensity fulfills $I(E_0) = I(E > E_\mathrm{F})$, in other words, such that the background is completely removed. figure 4.5 shows the construction of a Shirley background profile for an angle-integrated x-ray photoemission spectrum.

Slight variations, extensions and alternative procedures to the Shirley method, that effectively lead to very similar results exist [75]. More specialized methods are needed for the concrete case of angle-resolved photoemission. There, the Shirley procedure employed to the angle-integrated spectrum smears out any actual k dependence in the signal by increasing the background of all momentum distribution curves (MDCs) even if high intensity is found for only for a few values of k. On the other hand, using the Shirley scheme for each MDC independently effectively assumes that inelastic scattering preserves k, which is difficult to justify.

In the specific case of the cuprates, a specialized methodology has been suggested by Kaminski *et al.* [73]. They propose to fit each MDC with Lorentzian curves and take the linear contributions as the background signal for that energy (implicitly assuming k independence of the background). However, that approach is limited to single-band dispersions and quickly becomes impractical for multi-band systems, as one would have to adapt the curve fitting to the number of (expected) bands present in each MDC and it becomes unclear which linear part to use as the background.

Another method that we wish to present here was (to the best of our knowledge) first implemented by Christian Matt [76] and is loosely

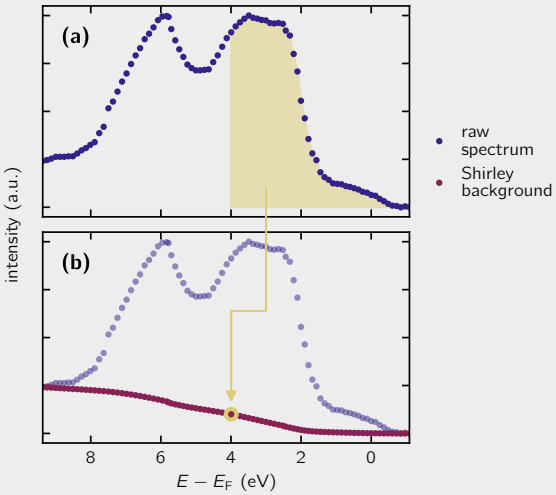

Figure 4.5: Construction of a Shirley background profile. **(a)** Data points of an x-ray photoemission spectrum of Au. The shaded region shows an integration range from a given binding energy (here 4 eV) downwards. The point of the background profile shown in **(b)** at that same energy is directly proportional to this area. Each point at binding energy E of the background is found by integrating the spectrum from E downwards. Finally, the so found background profile is normalized such that the high binding energy end of the spectrum and the background match up [factor s in equation (4.15)]. Data from [74].

based on the knowledge and expectations that underly the Shirley and Kaminski approaches. However, it accounts for the experiential observation that these models remain incomplete and sometimes even fail in practice. Therefore, a more pragmatic approach with very similar implicit assumptions is employed.

Here, the intrinsic background is assumed to be k-independent.[2] The background profile is estimated by averaging a number (e.g. five) of lowest intensity points of each MDC [1, 76]. In this fashion, a k-constant background at each binding energy is subtracted. The method therefore leaves MDCs unchanged. This comparatively simple procedure provides a practical and very efficient means of estimating the background counts from the data. The advantage to the more sophisticated methods discussed before is that it provides no tunable parameters that would affect the resulting background profile and is thus less susceptible to operator arbitrariness and more efficient when comparing numerous datasets. We stress, however, that for flat non-dispersive bands such a background determination is not advisable as the band structure will be eliminated in the subtraction procedure. Two examples, of this background subtraction scheme, using data on Eu-LSCO and Tl2201 from chapter 5, are shown in figure 4.6.

4.1.4 Tracing bands and enhancing their visibility

For quantitative statements it is usually necessary to carry out some sort of fitting of a model to the obtianed data. In the discussion of ARPES or similar data, however, one is sometimes just interested in semi-quantitative or qualitative observations: How many bands are there? At which energies do they start or end? Can we identify some band crossings? How do the measurements compare to predictions, e.g. of density functional theory (DFT) calculations? In order to address such questions it is often helpful to employ techniques that enhance the visibility of bands instead of going through a full fitting routine.

A method that has found widespread use [77–85] is to plot the second derivative of the (background subtracted) EDCs or MDCs. For two dimensional (2D) datasets it is common to apply a generalization

[2] The extrinsic k dependence that arises from channel dependent variable detector sensitivity can be removed by comparison to a reference spectrum.

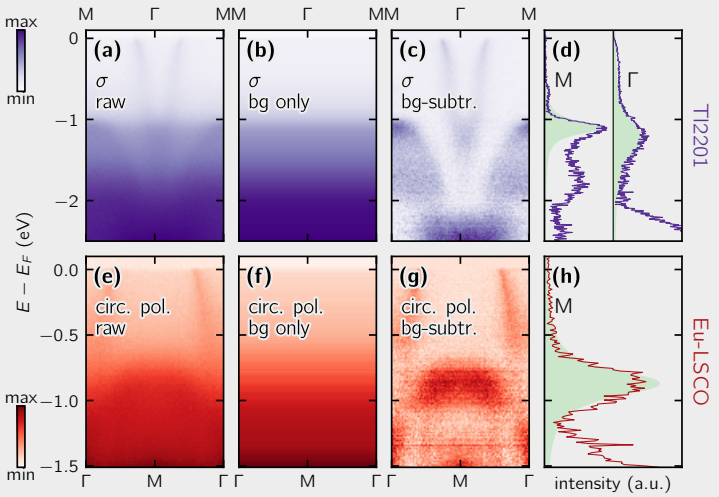

Figure 4.6: Demonstration of the used background subtraction procedure at the examples of Tl2201 (a-d) and Eu-LSCO (e-h) data. **(a)** and **(e)** Raw ARPES spectra. **(b)** and **(f)** k-independent background profile obtained by averaging the five lowest points at each energy row. **(c)** and **(g)** Result of subtracting (b)/(f) from (a)/(e), respectively. Features in higher binding energy the band structure that were previously hidden now become apparent. **(d)** and **(h)** EDCs at the Γ and M points of the background-subtracted spectra, as indicated.

of the second derivative, the Laplacian ∇^2:

$$\nabla^2 f(x,y) = \frac{\partial^2 f}{\partial x^2} + \frac{\partial^2 f}{\partial y^2} \quad . \tag{4.16}$$

The motivation for this methodology is that the absolute value of second derivative is typically large in the vicinity of a local maximum. There are drawbacks to the simplicity of this approach, though. The

peak positions in the second derivatives are generally slightly off the peak positions of the data and they can differ between MDC and EDC analyses.

For 2D analyses, significant distortions can occur depending on many factors, such as the directions and density of the features in data space. To overcome these problems, Zhang *et al.* [86] have proposed a more sphisticated method based on the 2D-curvature $C_f(x,y) \propto$

$$\frac{\left[1+a\left(\frac{\partial f}{\partial x}\right)^2\right] b\frac{\partial^2 f}{\partial y^2} - 2ab\frac{\partial f}{\partial x}\frac{\partial f}{\partial y}\frac{\partial^2 f}{\partial x \partial y} + \left[1+b\left(\frac{\partial f}{\partial y}\right)^2\right] a\frac{\partial^2 f}{\partial x^2}}{\left[1+a\left(\frac{\partial f}{\partial x}\right)^2 + b\left(\frac{\partial f}{\partial y}\right)^2\right]^{3/2}} \quad . \tag{4.17}$$

a and b are parameters that account for potentially different units of the variables x and y. Zhang *et al.* argue that the curvature C_f traces the actual peak positions more closely and more consistently than the Laplacian.

I want to stress again that the methods described in this section are unfit to produce quantitative or even reproducible results and should merely serve as a means for efficient data visualization that can serve as a basis for rough, qualitative statements or pointers for a model-based analysis. The first reason for this is the simple fact that these techniques are precisely *not* based on any physical model. The second reason is the high susceptibility of such visualization methods to the input parameters. Working with real data, I have found that tweaking the input parameters can lead to massively diverging results, sometimes going as far as creating the semblance of band features where there are clearly none to be found by more rigouros methodologies.

4.2 ARPES self-energy analysis

As we have seen in equation (3.15) in section 3.3.1, the spectral function that is probed by ARPES can be written in the form of a

Lorentzian line shape. By direct comparison to the general formulation of such a Lorentzian (we now drop the band index n in Z and ε for convenience),

$$\begin{aligned}\mathcal{A}(\mathbf{k}, E) &= \frac{1}{\pi} \frac{Z_{\mathbf{k}}^2 \operatorname{Im}\Sigma(\varepsilon_{\mathbf{k}})}{\left[E - \varepsilon_{\mathbf{k}} - Z_{\mathbf{k}} \operatorname{Re}\Sigma(\varepsilon_{\mathbf{k}})\right]^2 + \left[Z_{\mathbf{k}} \operatorname{Im}\Sigma(\varepsilon_{\mathbf{k}})\right]^2} \\ &= \frac{A}{\pi} \frac{\Gamma}{(E - E_0)^2 + \Gamma^2} \quad ,\end{aligned} \tag{4.18}$$

we can identify:

$$\begin{aligned} E_0 &= \varepsilon_{\mathbf{k}} - Z_{\mathbf{k}} \operatorname{Re}\Sigma \\ \Gamma &= Z_{\mathbf{k}} \operatorname{Im}\Sigma \\ A &= Z_{\mathbf{k}} \quad . \end{aligned} \tag{4.19}$$

Knowing that E_0 represents the peak position and Γ its full width at half maximum (FWHM), this, in principle, opens the path to extract the self-energy Σ from ARPES spectra. However, the temptingly simple assignments of equation (4.19) hide the energy dependence of $\operatorname{Re}\Sigma$ and $\operatorname{Im}\Sigma$. This means that the actual peak position itself will generally be a function of E and this has to be considered if one were to analyze EDCs. An additional complication when analyzing EDCs arises from the presence of a nontrivial E-dependent background (as was discussed in section 4.1.3) [38].

If the problem at hand allows for it, it is therefore often more practical to analyze MDCs instead [87]. In the vicinity of the Fermi level we can savely assume the bare band dispersion to be linear: $\varepsilon_{\mathbf{k}} \approx \hbar v_{\mathrm{F}}(k - k_{\mathrm{F}})$, with the Fermi velocity and wave vector v_{F} and k_{F}. With this, one can see that a peak in the MDC is expected for

$$k_0 = k_{\mathrm{F}} + \frac{E - \operatorname{Re}\Sigma}{v_{\mathrm{F}}} \quad . \tag{4.20}$$

In a typical routine where every EDC and/or MDC of an ARPES spectrum is fitted to a suitable function of roughly 4 to 8 parameters, this effectively results in a ratio of fitting parameters per datapoints

in the order of 1/60. Li *et al.* have proposed an alternative approach that fits the whole 2D spectrum at once by actually simulating the expected spectrum based on the energy dependent self-energy and the bare band dispersion [88]. Their routine starts by constructing the real part of the self-energy from the imaginary one by virtue of the Kramers-Kronig transformation, equation (3.16), and thereby implicitly ensures that the resulting self-energy fulfills causality. Additionally, the number of free parameters for fitting the whole spectrum comes down to 14, which gives a ratio of fitting parameters to datapoints of 1/6000, two orders of magnitude better than conventional EDC and MDC fitting. An example of the construction of a full spectrum from the imaginary part of the self-energy, a bare band dispersion and a gap function is shown in figure 4.7. The precise mechanism is elaborated on in section C.3 of appendix C.

Self-energy for Fermi liquids

A proper determination of the self-energy Σ from ARPES data requires an underlying model for the functional form of $\Sigma(\mathbf{k}, E)$. As the exact calculation of the self-energy is very difficult, reasonable approximations have to be used. A very common one is that of a Fermi liquid, which is also discussed in section 3.3.3. The self-energy for a Fermi liquid, Σ_{FL}, is characterized by a real part that is proportional to the energy E and an imaginary part proportional to E^2, as we can see in equation (3.19). It should be stressed here that the Fermi liquid description is only valid in the vicinity of the Fermi level E_{F} and breaks down beyond a critical energy E_{c}.

The *normal* Fermi liquid description has been found to be unable to explain many properties of cuprate high-temperature superconductors (HTSCs). An alternate, phenomenological model has been proposed, specifically for the case of the cuprates: the *marginal* Fermi liquid [89,

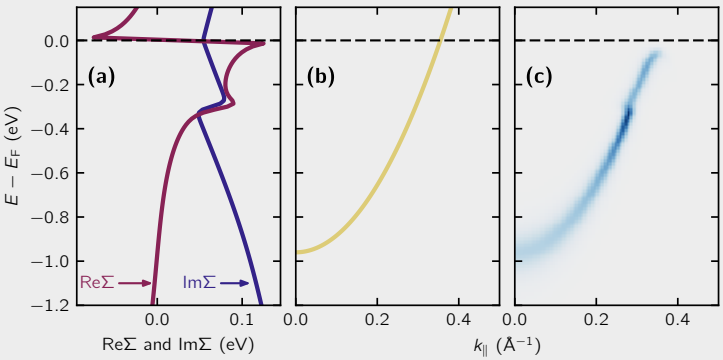

Figure 4.7: Example of spectrum construction for 2D fitting. **(a)** Real and imaginary parts of the self-energy. $\mathrm{Im}\,\Sigma$ is constructed according to a reasonable model [88] and $\mathrm{Re}\,\Sigma$ is found through the Kramers-Kronig transform. **(b)** A quadratic bare band dispersion $E_{\mathrm{bare}} = \hbar^2\mathbf{k}^2/(2m^*)$. **(c)** The complex self-energy and the bare band from panels (a) and (b) are used to construct the spectral function shown in this panel. The difference between a measured ARPES spectrum and the so constructed spectral function can serve as the optimization target in a fitting routine. See section C.3 for details.

90]. The self-energy for such a marginal Fermi liquid takes the form [38]

$$\Sigma_{\mathrm{MFL}}(\mathbf{k}, E) = \lambda(\mathbf{k}) \left[E \ln \frac{x(E,T)}{E_c} - i\frac{\pi}{2} x(E,T) \right] \quad . \tag{4.21}$$

with

$$x \approx \max(|E|, k_B T) \tag{4.22}$$

a coupling constant λ and a cutoff energy E_c. Notably, and as opposed to the *normal* Fermi liquid, the imaginary part is now approximately proportional to E while the real part goes as $E \ln E$. The marginal

Fermi liquid description has been used to describe the line-shapes in ARPES spectra of $Bi_2Sr_2CaCu_2O_{8+\delta}$ [91].

4.3 Live multidimensional data analysis

During an experimental session at a synchrotron beamline such as ARPES, tools for fast data inspection are of outmost importance. As will be layed out in section 4.3.1, it turns out that this necessity is found in many situations across various disciplines. This observation has motivated us to provide a solution that will hopefully be able to support people of diverse backgrounds in their endeavours. The result, the `data-slicer` package, is described in sections 4.3.2 and 4.3.3.

4.3.1 Evolution of data throughput

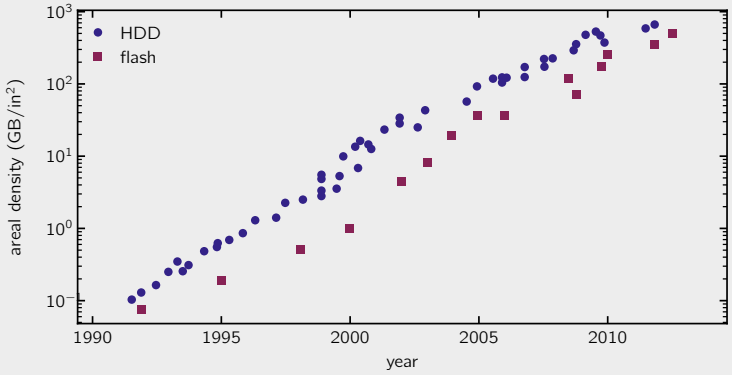

Figure 4.8: Exponential evolution of hard disk drive (HDD) and flash drive areal memory density over time. After [92] (CC BY-SA 3.0)

.

The digital revolution and the exponential growth in the capacity of technologies that are associated with it has had and continues to exert a tremendous impact on all aspects of human endeavours. Moore's law [94] that was originally formulated in terms of the number of electrical components that could be *crammed*[3] onto a given area, has shown to be applicable to a variety of developments. One example is the increase in data storage capacity per area, as shown in figure 4.8. Detection and processing electronics are affected, too, and most measurement techniques undergo steady improvements in acquisition times and resolution. As a result, the sheer data throughput is continually increasing for most analytical and observational disciplines. In the example of solid state physics, this development is accompanied by the tremendous improvements found in large scale facilities, such as synchrotrons, as is discussed in section 2.2.1 and highlighted in figure 2.2. A consequence of this convergence is that in many techniques the typical data output has evolved from being one dimensional (1D) to three dimensional (3D).[4] This is shown in figure 4.9, exemplified by spectra from ARPES [32, 95], scanning tunneling spectroscopy (STS) [27, 96] and inelastic neutron scattering (INS) [97–99] measurements.

More data per time being available should certainly accelerate the research process. However, a bottleneck arises in the human capacity to process and digest such large datasets. Particularly in time-limited synchrotron measurement sessions, where on the fly decisions about the direction of the ongoing experiment have to be made based on a fast preliminary analysis of the just acquired data, scientists require a means of quick data inspection. Many of the existing powerful and versatile visualization tools [100–103] are not well suited for this purpose and cannot easily support the specific and often changing needs of a given discipline. The result is that each community ends up developing their

[3]Wording by the original author Gordon E. Moore.

[4]In a private conversation, Eli Rotenberg has pointed to this development from a different perspective: "50 years ago you could publish with just one or two spectra. 20 years ago you would publish with a few hundreds of spectra. Nowadays, you need to measure in the order of 10 000 spectra to get a paper."

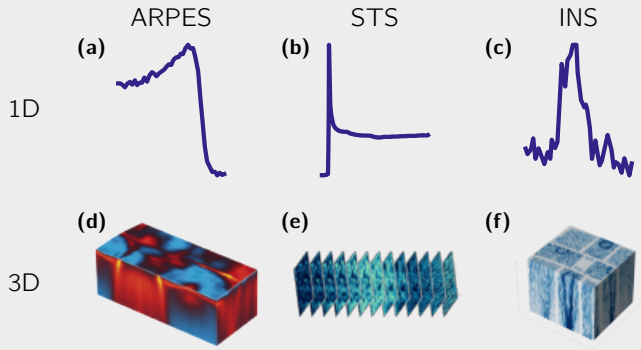

Figure 4.9: Evolution of typical data output from 1D to 3D for ARPES, STS and INS. The spectra are shown without any axis as their only use here is to exemplify the difference between published results from 40 to 60 years past [(a) [32], (b) [96] and (c) [97]] to more recent results [(d) [95], (e) [27] and (f) [98, 99]].

own solutions to the problem of quick data visualization and inspection, e.g. MJOLNIR [104] or PyARPES [105]. Since these implementations are usually intertwined and entangled with the community-specific parts, however, such solutions are typically not transferrable across different disciplines or experimental methodologies. Additionally, at the time of writing, many of the tools widely used in the ARPES community lack a means of centralized version control. This leads to the situation where various different, sometimes incompatible versions are present, making it difficult for the many brilliant individual contributions and improvements to spread and become available to other users. This problem is additionally enhanced in those cases where the tools rely on proprietary software, making sharing difficult due to licensing reasons.

4.3.2 The data-slicer package

The issues described in the previous section have motivated me to develop a solution that accounts for the identified need to offer fast live visualization at a general scope, i.e. without any assumptions about the meaning of the underlying data, but that would allow to be easily adjusted, tuned and/or extended for the specific problems at hand. Additionally, the exchange of fixes, improvements and enhancements should be facilitated by use of modern version control practices and the use of open-source standards. As a result, I have produced a piece of software by the name of `data-slicer`. It is publicly available online [106] and a corresponding paper has been published in the Journal of Open Source Software [5].

`data-slicer` is a python package that contains several functions and classes which provide modular widgets, tools and utilities for the visualization of 3D datasets. As an example, there is a widget that shows an interactive view of the xy-, xz- and yz-cutting planes through the data cube. The planes can be dragged to access different cuts. In another widget, only the xy-plane and a plane perpendicular to it are shown. The perpendicular plane, however, can be freely dragged and rotated to create non-rectangular cuts.

These building blocks can be combined freely to create new applications, specific to the problems a user may wish to solve, as schematically depicted in figure 4.10. Furthermore, the package already ships with one pre-assembled application made up from these building blocks. It is a graphical user interface (GUI) for rather general 3D data visualization and manipulation: the Python Image Tool (PIT).

PIT: The python image tool

PIT consists of a number of dynamic plot figures which allow browsing through 3D data by selecting slices of variable thickness from the data cube in real-time and to cute them up further. Two core features of PIT should be explicitly mentioned. The first is the ability to create

slices of the 3D data cube along arbitrary angles in real time. This is facilitated on the GUI side through a simple draggable line to select the slice direction. Internally, optimized functions enable the superior speed of this operation. The second feature worth mentioning is the inclusion of an ipython console which is aware of the loaded data as well as of all GUI elements. The console enables users to run any analysis routine suitable to their respective needs. This includes the ability to run python commands in a workflow familiar to pylab or Jupyter [107] notebook users. It also allows for running scripts from the console by use of ipython's line magic functions. Effectively, this design is central in empowering users to accomplish any task imaginable — as long as it is possible to achieve with python.

It is clear that it can get complicated and tedious to run certain types of data processing or analysis from the ipython console, as described in the previous paragraph. For such cases, PIT provides an additional level of customizability and control through its plugin system. Plugins for PIT are regular python packages that can be loaded from within PIT and enhance it with new functionality. A plugin can interact with all elements in PIT via the same interfaces as can be done through the built-in ipython console. Creating a plugin therefore requires little programming skills and no further knowledge of the inner workings of PIT. In this manner, different communities of users can create and share their field-specific plugins which allow them to customize PIT to their needs.

As an example, we mention the `ds-arpes-plugin` [108], which provides basic functionalities for loading of ARPES datasets and handles for typical analysis functions, customized and taylored to be used from within PIT.

4.3.3 Summary

In summary, with the `data-slicer` package [5] I hope to solve the problem of offering the right scope – neither too specialized that it

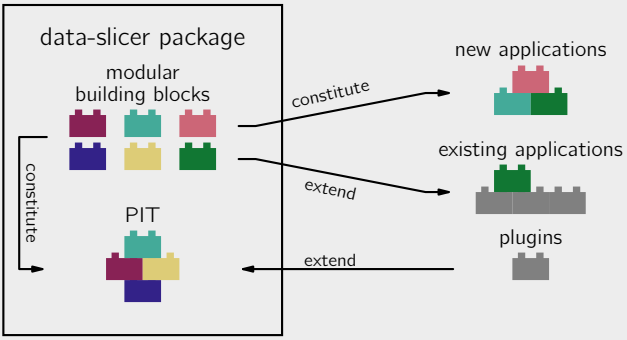

Figure 4.10: Schematic representation of the `data-slicer` package and the potential interactions with external software.

can only be used by a narrow community nor too bloated such that it becomes hard to do specific operations – by offering a variety of methods for users of varying backgrounds to get exactly the tools they need:

- On the first and most general level, PIT offers a ready-to-use GUI for quick 3D data visualization without any need of programmatic user input.

- Users can satisfy their more specific needs either through use of the console or by implementing a plugin, which can both be accomplished with little programming knowledge.

- On the last, most specific level users can use and arrange the building blocks contained in the package to create completely new applications or even embed PIT or other parts of the `data-slicer` package into an existing application.

The relation between different elements of the package and external software is schematically depicted in figure 4.10.

Chapter 5: Electronic structure of overdoped cuprate superconductors

During his time in the Laboratory for Quantum Matter Research (LQMR) [109], Christian Matt *et al.* discovered the $d_{3z^2-r^2}$ band in the cuprate high-temperature superconductor (HTSC) compound and realized that it affects the Fermi surface through hybridization with the

$d_{x^2-y^2}$ band. This discovery has sparked a number of subsequent experiments and investiagtions on the cuprate HTSCs within the LQMR group that have led to a number of related new insights, such as the identification of a type-II Dirac cone, the three-dimensionality of the band dispersion in the thought to be quasi two dimensional La-based cuprate systems and a methodology for predicting the experimental band structure of overdoped cuprates through density functional theory. The present chapter aims at giving an overview over the conducted studies and results.

We start by giving a short introduction into the cuprate HTSC family with a focus on the compounds used here in section 5.1 and a review of the discovery of the $d_{3z^2-r^2}$ band in section 5.2. Sections 5.2.2, 5.2.3 and 5.3 are dedicated to the presentation of the conducted studies and the discussion of the new observations. The chapter concludes with a summary in section 5.4.

The works presented in this chapter have been published in peer-reviewed journals. For section 5.2.2 [1] and section 5.2.3 [2] I have obtained co-authorship through participation and help with the experiments and by contributing to discussions. For the publication corresponding to section 5.3 [3] I have additionally taken a lead in the manuscript creation and data analysis, which is reflected by first authorship.

5.1 Introduction

The identification of $La_{2-x}Ba_xCuO_4$ (LBCO)[1] as a superconducting material [18] whose properties could not be described by Bardeen-Cooper-Schrieffer (BCS) theory gave birth to a series of discoveries of related copper based compounds. This family of materials is exhibits relatively high superconducting transition temperatures T_c and its members are now commonly known as the cuprate high-temperature superconductors (HTSCs), often simply referred to as *cuprates*.

Cuprate HTSCs crystallize in the Ruddlesden-Popper layered perovskite arrangement [110]. Their structures are characterized by the Cu atoms that find themselves embedded in octahedra (or squares, if the top and bottom *apical* corners are missing) of O atoms. These CuO_2 plaquettes form a planar arrangement that is repeated n times along the out-of-plane direction, where typically $n \in \{1, 2, 3, 4\}$. Stacks of n such CuO_2 planes are separated by layers of relatively large atoms. Figure 5.6 shows the crystal structures for four single-layer ($n = 1$) representatives of the cuprate family. The superconducting transition temperature T_c has been found to increase with the number of neighboring layers n, but only up to $n = 3$. For $n = 4$ it is found to decrease again [111, 112]. The common denominator in these compounds are the CuO_2 planes, and it is therefore believed that the relevant physics for HTSC must take place there, and that it therefore exhibits a quasi-two dimensional (2D) nature, especially for $n = 1$.

The physics of cuprate superconductors (SCs) has been a subject of intense investigations for more than three decades [113–115]. Researchers have discovered a plethora of phases and states of matter that can be realized in the cuprates when tuning the temperature, charge carrier concentration by means of electron or hole doping, ex-

[1] The actual composition of LBCO was not known at the time. The original publication incorrectly assumes the chemical formula $Ba_xLa_{5-x}Cu_5O_{5(3-y)}$. This comment is not meant to diminish the value of Bednorz' and Müllers work, but rather to serve as a gentle reminder of the likely incompleteness of our current knowledge.

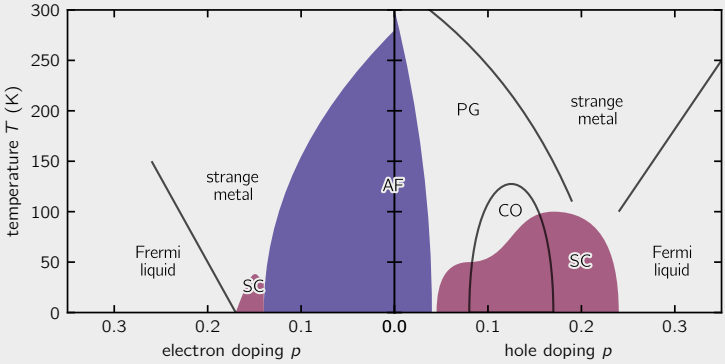

Figure 5.1: Schematic doping-temperature phase diagram of electron- (left) and hole-doped (right) cuprate HTSCs. These compounds host a large number of different phases. The undoped parent compound is an antiferromagnetic (AF) Mott insulator. The charachteristic superconducting (SC) domes emerge for certain doping regimes. Beyond said regimes, in the *overdoped* situation a *normal* Fermi liquid is found. Additional complications are present for the hole-doped phase diagram, where the elusive pseudogap (PG) phase and charge order (CO) appear in the vicinity of the SC domes, raising the question of whether or not the relation between these states of matter is of competitive, constructive or indifferent nature. Adapted from [113] and [114].

ternal pressure and others. A schematic of the famous temperature versus doping phase diagram is depicted in figure 5.1. Despite these tremendous efforts and the detailed mapping out of the phase diagram, some of the most fundamental questions related to high-temperature superconductivity still remain open. For example, consensus on the mechanism underpinning cuprate superconductivity is still missing: Is the interaction that leads to the formation of Cooper pairs phonon mediated, like in BCS theory, or is it electron mediated or even something

else entirely? Related to this is the question of the defining parameters for the transition temperature T_c [76, 116–120], and how to optimize it. After all, the major motivation behind the research on HTSCs is the hope for the discovery of a room-temperature SC.

5.2 Cuprate electronic band structure

Starting point for most theoretical approaches to superconductivity is an (effective) electronic band structure along with the interactions that are relevant for driving a pairing mechanism. The former is typically obtained through density functional theory (DFT). However, because DFT cannot describe all relevant aspects of the electronic structure (such as the Mott insulating phase out of which superconductivity emerges upon hole or electron doping [121], see also description of figure 5.1) it is commonly viewed as too simplistic of an approach in the context of the cuprates [122]. Another widespread assumption is that effective models for cuprates can be constructed solely based on the $d_{x^2-y^2}$ band structure, i.e. on the single band crossing the Fermi level alone. This latter assumption has recently been challenged and it has been proposed that hybridization between the $d_{x^2-y^2}$ and the $d_{3z^2-r^2}$ bands could be the reason for the strong material dependence of T_c in the cuprates [118, 123].

5.2.1 From a single- to a multiband picture

The great majority of spectroscopic studies on the cuprate HTSCs have focused on the intriguing low energy phenomena, such as the characteristic *kinks* in the dispersion of the $d_{x^2-y^2}$ states that are due to band renormalization effects from strong electronic correlations [38] (self-energy effects, see section 3.3). Matt *et al.*, on the other hand, have studied the band structure of overdoped $La_{2-x}Sr_xCuO_4$ (LSCO) to higher binding energies, up to 2.5 eV with angle-resolved photoemission spectroscopy (ARPES). They discovered a $d_{3z^2-r^2}$ derived band

between 1 eV and 1.5 eV binding energy and are able to measure a finite dispersion of this band along k_z. Their observations reveal that the $d_{x^2-y^2}$ band hybridizes with this newly discovered $d_{3z^2-r^2}$ band. As a result, it is proposed that the usual single band tight binding (TB) model that is employed to model the single layer cuprate band structure should be replaced by a two band model that allows for exchange between the $d_{x^2-y^2}$ and $d_{3z^2-r^2}$ bands [76]. Said model is presented in appendix A.

A summary of their result is presented in figure 5.2. Different bands are clearly identified and their dispersions are well described by the two band TB model. The model predicts that no hybridization takes place along the direction ΓM, where the two states show opposite mirror symmetry. On the other hand, along ΓX, contributions of the $d_{3z^2-r^2}$ state can be found in the dispersion crossing the Fermi level. As mentioned before, such a hybridization has been argued to be unfavourable for superconducting pairing [118, 123]. The observation could therefore provide an explanation for the comparatively low value of T_c in LSCO (see also table 5.3).

This discovery has motivated our group to carry out a series of ARPES investigations into the higher energy band structures of the cuprates. These studies have yielded a tetralogy of results that shall be discussed in the following:

- Idenitification of a 2D type-II Dirac cone in LSCO [1], section 5.2.2.

- Three-dimensionality of the FS in overdoped La-based cuprates [2], section 5.2.3.

- A universal methodology for DFT based electronic structure calculations across hole- and electron-overdoped cuprates [3], section 5.3.

- Universality in the Fermi liquid picture across oxide compounds from a spectroscopic viewpoint. As this work is thematically

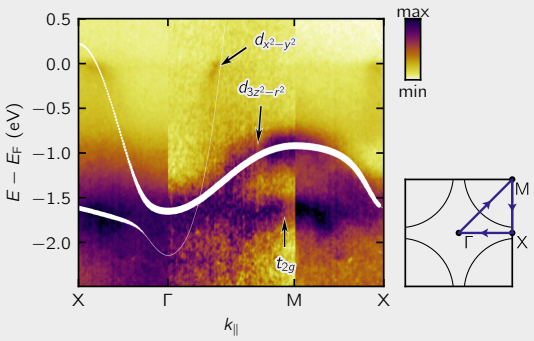

Figure 5.2: ARPES energy distribution maps (EDMs) of LSCO along high symmetry directions of the in-plane Fermi surface (FS) as indicated in the schematic to the right. Overlayed are the $d_{x^2-y^2}$ and $d_{3z^2-r^2}$ bands as predicted by a two band TB model. The marker thickness is proportional to the predicted $d_{3z^2-r^2}$ weight. While no $d_{3z^2-r^2}$ weight is found on the $d_{x^2-y^2}$ branch along ΓM, the two bands show appreciable mixing along ΓX, extending up to the Fermi level. Figure from [76].

distinct from the previous three which all link to qualitative electronic structure, it will be discussed separately in chapter 6.

5.2.2 Two-dimensional type-II Dirac fermions

We have seen in the previous section (and through the two band TB model of appendix A) that the crossing of the $d_{x^2-y^2}$ and $d_{3z^2-r^2}$ bands in LSCO is protected along the nodal (π, π) direction, because the bands do not hybridize along this line due to opposite mirror symmetries. Based on this fact and supported by additional measurements, we were able to show that this crossing constitutes an interesting topological state: a type-II Dirac cone [1].

Dirac fermions manifest themselves as touching points of an electron-like and a hole-like band, forming a cone-like shape. The presence of a Dirac point in the vicinity of the Fermi level leads to distinct physical properties, many of which originate from a variation of the density of states (DOS). One of the most prominent examples of a Dirac point is found in graphene [124]. Dirac fermions are classified into types I and II according to the degree of Lorentz-invariance breaking [125, 126]. In more practical terms, in a type-I Dirac cone, the electron- and hole-like sheets respectively are clearly located either below or above the energy of the touching point. They can be separated by a constant energy plane. In a type-II Dirac cone, on the other hand, the cone axis can be seen as *tilted* with respect to the energy axis in E-$\mathbf{k}$-space. As a consequence, while the DOS vanishes at the touching point for a type-I Dirac fermion, it remains finite in the type-II case. Confer figure 5.3 for a schematic representation of the two types.

Besides the famous case of graphene, a variety of systems has been found to host type-I Dirac fermions, for example topological insulators [127], semimetals such as Na_3Bi [128], Cd_3As_2 [129] and black phosphorus [130, 131]. Meanwhile, type-II Dirac fermions seem to be less common. Even though their existence has been predicted theoretically in transition-metal icosagenides [132], dichalcogenide semimetals [133], and photonic crystals [134], only recently have three-dimensional type-II Dirac fermions been identified experimentally in $PtTe_2$ [135], $PtSe_2$[136] and $PdTe_2$ [137].

The identification of this type-II cone in LSCO is therefore of great interest. What makes this discovery even more intriguing, however, is the observation that – due to the dispersion of the $d_{3z^2-r^2}$ band – the type-II Dirac cone in LSCO is 2D: While we can visualize it as a cone in E-k_x-k_y-space, the touching point has to be thought of as a line in the full E-$\mathbf{k}$-space, with a finite dispersion along k_z. This is in contrast to the other mentioned examples. Out of the known type-I Dirac fermions, only the one in graphene exhibits a similar 2D nature. In all other compounds, the touching point of the Dirac cone, be it

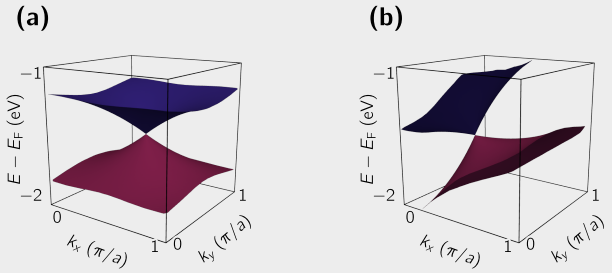

Figure 5.3: Schematic representation of Dirac cones in E-k_x-k_y-space. **(a)** Type-I and **(b)** type-II Dirac cones can be thought of as two sheets of electronic dispersions touching at one point. While the cone axis is parallel to the energy axis in the type-I case shown in (a), the axis is tilted for a type-II Dirac cone.

type-I or type-II, is a single point in E-**k**-space. To our knowledge, our discovery therefore presents the first demonstration of a 2D type-II Dirac cone (confer table 5.1).

Table 5.1: Examples of experimentally identified Dirac fermions classified by dimensionality and type.

	Type-I	Type-II
2D	Graphene [124]	LSCO [1]
3D	Na_3Bi [128], Cd_3As_2 [129]	$PtTe_2$ [135]

Tuning the Dirac cone location

As has been mentioned above, interesting physical properties manifest if a Dirac cone is located in the vicinity of the Fermi level. The crossing between the $d_{x^2-y^2}$ and $d_{3z^2-r^2}$ bands, however, occurs around 1.5 eV binding energy. We therefore discuss experimental routes to control the energy position of the Dirac point. The energy of the $d_{3z^2-r^2}$ band is controlled by the distance between the apical oxygen and the CuO_2 plane, as shall be laid out in detail in section 5.3. A smaller c-axis lattice parameter would thus push the $d_{3z^2-r^2}$ band and hence the Dirac point closer to E_F. Such a c-axis compression could be implemented through uniaxial pressure on a bulk crystal or substrate-induced tensile strain for thin films. Another possibility would be to induce chemical pressure by partial substitution of La for Eu, which would reduce c as a consequence of the smaller atomic volume of Eu compared to La. It has been estimated that a 20 % substitution could push the $d_{3z^2-r^2}$ band about 200 meV closer to E_F [76]. Similar procedures have been proposed for $Ir_{1-x}Pt_xTe_2$, which hosts three dimensional (3D) type-II Dirac fermions [138].

Knowing that DFT calculations can reliably predict gross band structure features (section 5.3), we have identified an even better starting point for obtaining a Dirac point near the Fermi level in an oxide: The isostructural nickelate sister compound $Eu_{2-x}Sr_xNiO_4$ (ESNO). Our DFT calculations on ESNO predict a qualitatively very similar electronic structure to LSCO, but shifted to lower binding energies. In fact, we find that the Dirac cone lies just a few 100 meV above E_F, consistent with a soft x-ray ARPES (SX-ARPES) study that detects the $d_{x^2-y^2}$ and $d_{3z^2-r^2}$ bands, but not their crossings [139]. Through the measures described above, it might be possible to bring that crossing down to the Fermi level. We thus propose oxides and related compounds to be promising candidates to realise novel and intresting topologically protected states.

5.2.3 Three-dimensional Fermi surface of La-based cuprates

Due to the quasi-2D nature of the CuO_2 planes in the single layered cuprate HTSCs (section 5.1), it had been widely assumed that their electronic structures would also be quasi-2D and not show any appreciable k_z dispersion of the FS. This expectation has been confirmed by several observations, for example that of quantum oscillation (QO) and ARPES measurements on $Tl_2Ba_2CuO_{6+\delta}$ (Tl2201), where a single large FS sheet is found. Up to the time when the here presented study was conducted, no ARPES measurement had provided any information about a possible three-dimensionality of the FS. Still, due to the limited intrinsic accuracy along k_z (k_z broadening), a 3D nature could not be excluded. In fact, the observation of a discernible k_z dispersion of the $d_{3z^2-r^2}$ band by Matt *et al.* combined with the fact that its hybridization with the $d_{x^2-y^2}$ affects the FS, led us to believe that a 3D FS could be expected.

Knowing the clear answer to the question of 2D versus 3D, however, would be key in solving some of the puzzles in cuprate phenomenology. For example, two scenarios have been proposed as explanations for the divergence of the specific heat coefficient γ at critical doping p^*: (i) It might be explained through DOS enhancement resulting from a vicinity of the van Hove singularity (VHS) to E_F at critical doping. (ii) Alternatively, the specific heat divergence could be a signature of quantum criticality due to the vanishing pseudogap phase. Explanation (i) is expected to be significant for quasi-2D band structures [140]. One could therefore exclude this scenario in the case of a 3D FS with implications to quantum criticality and pseudogap physics.

Motivated by these facts and the recent discoveries layed out in section 5.2.1, we have conducted an SX-ARPES study on LSCO ($x = 0.22$, $T_c = 22\,K$), $La_{2-x-y}Eu_xSr_yCuO_4$ (Eu-LSCO) ($x = 0.21$, $T_c = 15\,K$) and Tl2201 ($T_c = 20\,K$). The use of soft x-rays minimizes the problem of k_z broadening [141] and the three materials exhibit properties that are beneficial for such a study. Since $p > p^*$ for the used LSCO sample, it does not display any pseudogap physics and

the FS is well defined. Secondly, the three compounds crystallize in a body-centered tetragonal (BCT) structure and therefore avoid the orthorombic band folding that can otherwise complicate the picture, as is the case in $Bi_{2-x}Pb_{x+y}Sr_{2-y}CuO_{6+\delta}$ (Bi2201) [142, 143].

Methods

Single crystals of LSCO, Eu-LSCO and Tl2201 were grown by the floating zone and self-flux techniques. In- and out-of-plane lattice constants a and c, respectively, of the different compounds are listed in table 5.2. In the following, we will make use of the effective layer spacing in the BCT crystal structure $c' = c/2$. The samples have been characterized and their high quality has been established by previously conducted experiments on the same batch of crystals [144–147]. The presented data was obtained at the SX-ARPES end station of the ADRESS beam line [148, 149] at the Swiss Light Source (SLS) of the Paul Scherrer Institute (PSI). ARPES spectra were recorded at a temperature $T = 12\,\mathrm{K}$ with circularly polarized photons of 300 eV to 600 eV energy. The energy and momentum resolutions (full width at half maximum (FWHM)) are in the order of 90 meV and $0.02\,\pi/a$ respectively, though the exact values vary slightly depending on the incident photon energy. Pristine surfaces were realized using the standard top post method or a dedicated cleaving tool [47].

Experimental results

Figure 5.4 shows a representative in-plane Fermi surface map (FSM) obtained with 362 eV photons, corresponding to a value of $k_z = 21\,\pi/c'$. The map covers several Brillouin zones (BZs) and the positions of the BCT high symmetry Γ and Z points are labeled, while simple tetragonal BZ boundaries are indicated. A strong k_z dispersion could be identified by comparing such an FSM with one recorded with a photon energy corresponding to a different value of k_z. However, for a subtle effect such as the one we expect here, it is much clearer to extract a k_z

Table 5.2: Lattice constants (in Å) and TB parameters (in units of the respective nearest neighbor (NN) hopping parameter t) of compounds referred to in section 5.2.3.

		LSCO ($x = 0.22$)	Eu-LSCO ($x = 0.21$)	Tl2201 ($T_c = 20\,\mathrm{K}$)
$a = b$	(Å)	3.76	3.79	3.87
$c = 2c'$	(Å)	13.22	13.14	23.20
t'	(t)	-0.12	-0.14	-0.28
t''	(t)	0.06	0.07	0.14
μ	(t)	0.93	0.95	1.44
t_z	(t)	0.07	0.07	< 0.015

dispersion by FS mapping directly along k_z. This is done by recording the same $k_\parallel$-E EDM over a range of incident photon energies. The two cut directions, namely the *nodal* or (π, π) cut and the *antinodal* or $(\pi, 0)$ cut are indicated by thick lines in figure 5.4.

The resulting out-of-plane $k_\parallel$-k_z FSMs for the representative case of LSCO are shown in figure 5.5. The data extends across more than two full BZs along k_z or more than five units of π/c', corresponding to photon energies ranging from 425 eV to 600 eV. Across this range, no appreciable dispersion is identified along the nodal (π, π) direction [panel (a) in figure 5.5]. In the antinodal $(\pi, 0)$ direction, on the other hand, a clear periodic dispersion is found [panel (b)]. The dispersion flows parallel to the BCT BZ boundary that is indicated as a zig-zag line above $k_x = \pi/a$. The same observation is made in Eu-LSCO. Tl2201, meanwhile, shows no discernible k_z dispersion along either direction. For the sake of space and conciseness, I refrain from showing the datasets for these two compounds here and refer the interested reader instead to the published version [2].

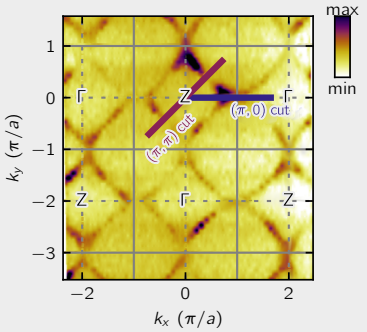

Figure 5.4: In-plane FS map of LSCO. The data has been obtained using SX-ARPES at a temperature $T = 12\,\mathrm{K}$ and the shown electron intensities have been integrated in a region of $\pm 20\,\mathrm{meV}$ around the Fermi level. The used photon energy is $h\nu = 362\,\mathrm{eV}$ corresponding to a value of $k_z = 21\,\pi/c'$ at the zone center. Thick lines indicate the directions of the out-of-plane cuts shown in figure 5.5.

Three dimensional tight binding model

Despite the previously described discovery of hybridization between $d_{x^2-y^2}$ and $d_{3z^2-r^2}$ bands, we find that the k_z dispersion can be adequately parametrized by a single band TB model that allows for out-of-plane hopping:

$$\varepsilon_{3D}(k_x, k_y, k_z) = \varepsilon_{2D}(k_x, k_y) + \varepsilon_z(k_x, k_y, k_z) \quad , \tag{5.1}$$

with the in-plane single band ($d_{x^2-y^2}$) contribution

$$\begin{aligned} \varepsilon_{2D}(k_x, k_y) = &-\mu + 2t[\cos(k_x a) + \cos(k_y a)] \\ &+ 4t' \cos(k_x a)\cos(k_y a) \\ &+ 2t''[\cos(2k_x a) + \cos(2k_y a)] \end{aligned} \tag{5.2}$$

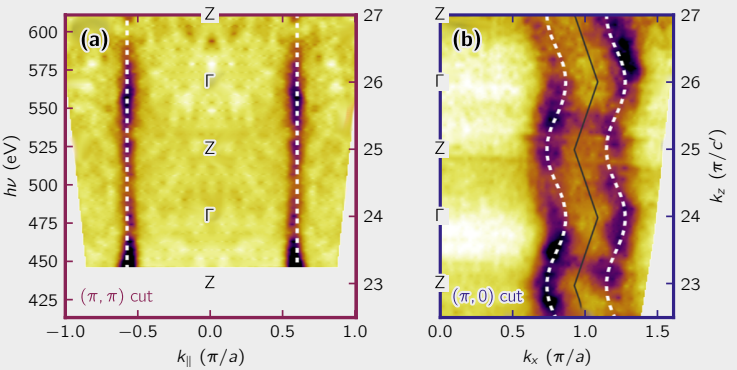

Figure 5.5: Out-of-plane FSMs of LSCO along the directions indicated in figure 5.4. **(a)** corresponds to the (π, π) direction while **(b)** shows the (π, 0) cut. Experimental and processing parameters and colormap are identical to the ones used in said figure. Dashed lines show the dispersions as predicted by the 3D TB model.

and the out-of-plane dispersion

$$\varepsilon_z(k_x, k_y, k_z) = 2t_z\sigma(k_x, k_y)[\cos(k_x a) - \cos(k_y a)]^2 \cos(k_z c') \quad . \tag{5.3}$$

In above equations, μ denotes the chemical potential. t, t' and t'' represent first, second and third NN hopping parameters and t_z stands for the interlayer hopping. The factor

$$\sigma(k_x, k_y) = \cos(k_x a/2)\cos(k_y a/2) \tag{5.4}$$

is a result of the BCT characteristic offset of successive CuO_2 planes by $\mathbf{r}_{\parallel} = (a/2, a/2)$ [140].

The experimentally observed band structure is fitted by this model with parameters as in table 5.2. The results are plotted above the data as dashed lines in figure 5.5.

Implications of the observed out-of-plane dispersion

The obtained band structure can be used to calculate the DOS, which can in turn be translated into a value for the electronic specific heat coefficient (Sommerfeld constant γ) via

$$\gamma = \frac{\pi^2 k_B^2}{3} \mathrm{DOS}(E_F) \quad . \tag{5.5}$$

We calculate the DOS as a function of doping for LSCO and Eu-LSCO. To this end we assume that all the hopping parameters are independent of doping. This assumption is experimentally verified for the in-plane parameters and we extend it to the out-of-plane hopping t_z with the argument that the lattice constants do not change significantly with doping. Under this assumption, the only parameter of our 3D TB model that varies is the chemical potential μ.

Comparison of the so calculated Sommerfeld constant as a function of doping between the obtained 3D model and a 2D model ($k_z = 0$) reveals that a divergent γ can indeed only be expected for the 2D case. The obtained values from the 3D case can only account for less than half of the directly measured γ. These findings clearly rule out the VHS scenario (i) that was presented as a possible explanation for the diverging specific heat in the introduction of section 5.2.3. Instead, effects beyond band structure need to be considered and scenario (ii) — quantum criticality emerging from the collapse of the pseudogap phase — provides a plausible explanation.

5.3 Comprehensive band structure study

The intriguing proposition that the influence of the $d_{3z^2-r^2}$ band on the electronic structure at the Fermi level could be a deciding factor for superconductivity has motivated us to extend the search for the $d_{3z^2-r^2}$ band to other cuprate systems. In the following, we provide and discuss our systematic ARPES and DFT study of the electronic

d-band structure across single layer cuprate SCs. Five different hole- and electron-overdoped superconducting systems [Eu-LSCO ($x = 0.2$, $y = 0.21$), LSCO ($x = 0.23$), Bi2201 ($x = 0.26$, $y = 0.12$), Tl2201, and $Pr_{2-x-y}La_xCe_yCuO_4$ (PLCCO) ($x = 0.7$, $y = 0.15$)] have been investigated experimentally. A selection of physical properties of these compounds can be found in table 5.3.

Table 5.3: Selection of physical properties of the HTSCs used in this work. a and c denote the in- and out-of-plane lattice constants of the simple tetragonal unit cell respectively. d_A is the apical oxygen atom separation as in figure 5.13. t and t' are nearest and next-nearest neighbor hopping parameters for a TB model. T_c and T_c^* are the superconducting transition temperatures at the present and optimal dopings respectively.

	a Å	c Å	d_A Å	t'/t 1	T_c K	T_c^* K
LSCO	3.77	15.26	2.42	0.18	37	37
Bi2201	3.82	24.5	2.58	0.28	40	130
Tl2201	3.87	23.23	2.72	0.35	85	140
PLCCO	3.98	12.2	∞	−0.19	19	27

5.3.1 Methods

Experiments and Data Processing

Single crystals of Eu-LSCO, LSCO, Bi2201, Tl2201 and PLCCO were grown by floating zone or flux growth techniques. Both ultraviolet (20 eV to 200 eV) and soft x-ray (200 eV to 600 eV) ARPES experiments were carried out at the SIS [150] and ADRESS [149] beamlines at the Swiss Light Source. All data was recorded at a temperature of approximately 20 K. Electrons were analyzed through a slit oriented

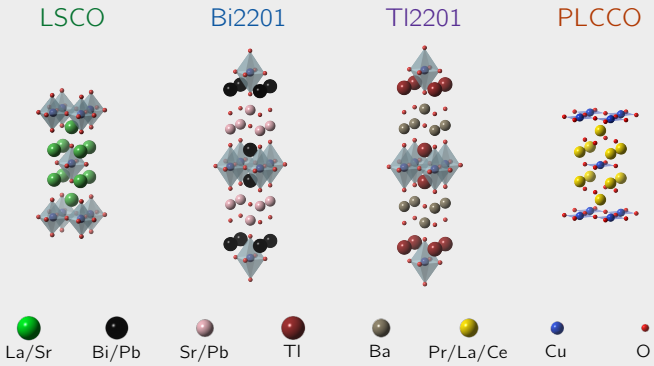

Figure 5.6: Crystal structures of the measured compounds. Shown is one tetragonal unit cell. The typical Cu-O octahedra (or Cu-O planes for PLCCO) are highlighted by blue translucent planes.

within the photoemission mirror plane [38]. Light polarization perpendicular (parallel) to the mirror plane is denoted as σ (π) (see also section 2.3.2).

The background in the ARPES spectra is subtracted using Matt's method described in section 4.1.3 and illustrated on datasets from the present chapter in figure 4.6. We repeat here the shortcoming of this background subtraction routine which is that it would completely suppress nondispersive, flat features. We therefore only apply the background subtraction in figures 5.9 and 5.10 to enhance the visibility of dispersive bands.

DFT Calculations

Predicting the correct energies for the electronic bands is a notorious problem for DFT in many materials, which is mostly due to the unknown form of the exchange-correlation functional (see section 3.2).

Improvements over local density approximations are commonly obtained using hybrid functionals which mix in an amount $0 \leq \alpha \leq 1$ of exact exchange from Hartree-Fock theory [151]. While α is a free parameter in general, we find good agreement between the theoretical and experimental band structures for all compounds studied by fixing $\alpha = 0.1$. We thus propose this value as generically suited for cuprate SCs.

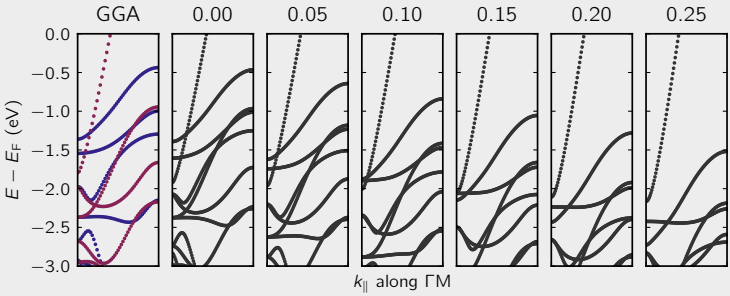

Figure 5.7: Nodal DFT band structure for LSCO for different values of the mixing parameter α, as indicated above the panels. The leftmost panel shows the generalized gradient approximation (GGA) results that should correspond to $\alpha = 0$ with color coded even or odd mirror eigenvalues.

A hypothetical tetragonal structure of LSCO with lattice parameters corresponding to overdoped LSCO was used and the chemical potential adjusted to match the actual hole-filling. Similarly, for Bi2201, Tl2201 and PLCCO stochiometric tetragonal crystal structures were used as a starting point for the DFT calculations. See figure 5.6 for the different compounds' crystal structures. We ensured, on the example of Bi2201, that using an orthorhombic crystal structure leads to essentially the same results after downfolding the calculated band structure to the tetragonal Brillouin zone.

Although some of the systems studied have orthorhombic structures, we represent all data in tetragonal notation [38], using the CuO_2

plaquette Brillouin zone nomenclature. Therefore M and X, respectively, denote the zone corner $(1, 1)$ and boundary $(1, 0)$ in units of π/a with a being the tetragonal in-plane lattice parameter [figure 5.8 (c), inset].

5.3.2 Results

ARPES measurements

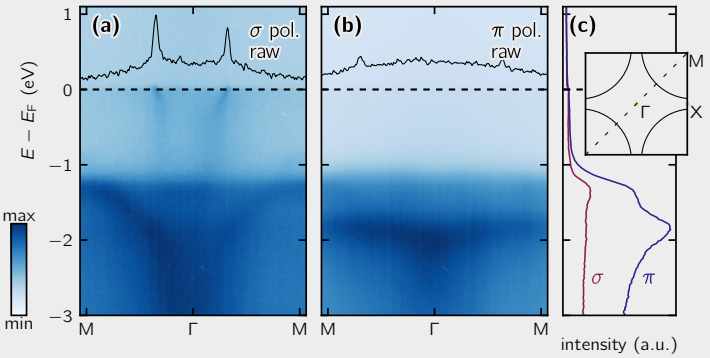

Figure 5.8: Nodal soft x-ray ARPES spectra recorded on Bi2201 with 420 eV incident photons of different linear polarizations, as indicated. **(a),(b)** Recorded ARPES spectra along the line $\overline{\mathrm{M\Gamma M}}$ (dashed line in the inset of (c)) for σ- and π-polarized light, respectively. Depicted at the top are momentum distribution curves taken at the Fermi level E_F. **(c)** energy distribution curves (EDCs) taken at the M points of the spectra in (a) and (b). Inset: schematic of the FS with the diagonal (nodal) direction indicated as a dashed line.

We start by examining the nodal spectra recorded on overdoped Bi2201 using linearly polarized soft x-rays, see figure 5.8. The photoemission intensities of the observed band structure are highly dependent on the incident light polarization. Three distinct bands are identified.

(i) The intensely-studied nodal quasiparticle (QP) dispersion [146, 152, 153] crossing the Fermi level E_F, which is observed with σ-polarized light only. This fact can be appreciated both from the energy distribution maps (EDMs) and the momentum distribution curves (MDCs) at the Fermi level [figure 5.8 (a),(b)]. (ii) A second dispersive band with energy maximum of -1.3 eV at the M-point and band bottom at the Γ-point. At the M-point, this band is featured in both the σ and π channels, as can be seen from the EDCs at M in figure 5.8 (c). Notice that in comparison to previous studies of Bi2201, our data displays extremely weak (π, π)-folded replica bands [143, 154]. As a result and in contrast to references [155] and [156], this dispersive band is not found at the (π, π)-folded equivalent Γ-point. (iii) The π-channel features an additional weakly dispersive band at energy -1.8 eV [figure 5.8 (b)]. This band, which to the best of our knowledge has not been reported previously, is completely suppressed in the σ-sector.

Nodal ARPES spectra recorded in σ and π polarization on LSCO, Bi2201, Tl2201 and PLCCO are shown in figures 5.9 and 5.10. For all four compounds, the band crossing the Fermi level is visible (suppressed) in the σ (π) channel. Interestingly, the bottom of this band varies significantly, from -2 eV in LSCO to -1.25 eV in Tl2201. In the π channel an additional band feature appears for LSCO, Bi2201 and PLCCO. The position and band width of this σ-suppressed band differs for the three compounds. In LSCO, it disperses from -0.9 eV at the M-point to -1.5 eV at the zone center, while for Bi2201 and PLCCO the π-branches found at -1.8 eV and -2.5 eV respectively, are quasi non-dispersive. Meanwhile, for Tl2201 no band unique to the π channel was identified down to -3 eV.

DFT calculated band structure

The DFT band structure of LSCO, Bi2201, Tl2201 and PLCCO as overlayed in figures 5.9 and 5.10 has been calculated as described in section 5.3.1. In addition to the band dispersions, their expected

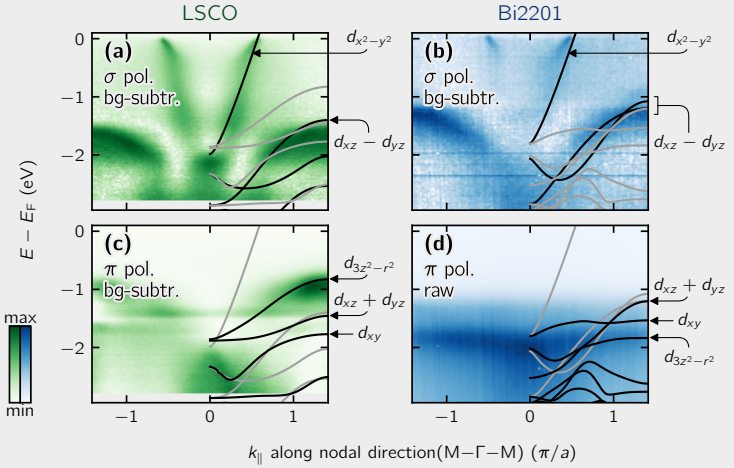

Figure 5.9: Nodal ARPES spectra and DFT band structure calculations for the single-layer cuprates LSCO and Bi2201. **(a)**–**(d)** Nodal ARPES spectra recorded using polarized light as indicated. The calculated DFT band structure is overlaid with solid lines where black and light grey colors indicate finite or zero matrix elements, respectively. The labeling of the orbital character is only valid at the M point for the cases of d_{xz}, d_{xy} and d_{yz}. See figure 5.11 for a full orbital character assignment.

photoemission matrix elements are indicated according to their mirror eigenvalues. To first order, photoemission matrix elements can be understood through simple symmetry considerations [38, 56], as is explained in section 2.3.2. The situation in the concrete case at hand is as follows: The experimental setup has a mirror plane defined by the incident photon beam and the electron analyzer, as discussed in section 2.3.2 of chapter 2. With respect to this plane, the electromagnetic field **A** has even (odd) parity for parallel (perpendicular) π (σ) polarization (figure 2.5). Meanwhile, the photoemitted electron

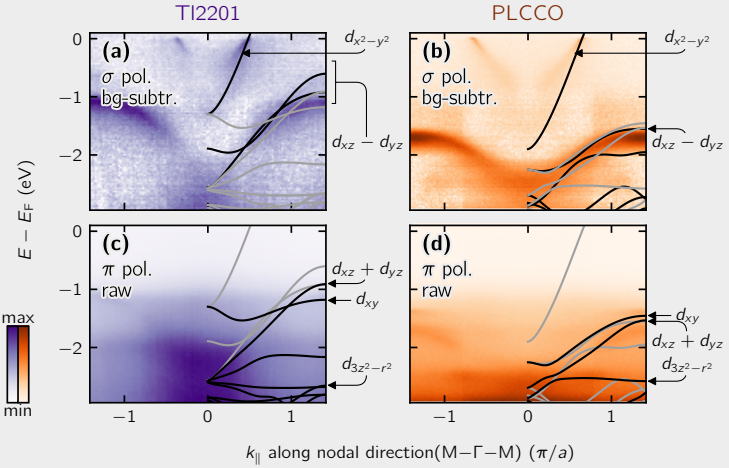

Figure 5.10: Nodal ARPES spectra and DFT band structure calculations for the single-layer cuprates Tl2201 and PLCCO. Refer to the caption of figure 5.9 for further explanations.

wave function has even parity. The mirror eigenvalues of the ($d_{x^2-y^2}$, $d_{3z^2-r^2}$, d_{xy}, $d_{xz}+d_{yz}$, $d_{xz}-d_{yz}$) orbital states are (-1, 1, 1, 1, -1), respectively (table 5.4). Therefore, $d_{3z^2-r^2}$ and d_{xy} states will be suppressed in the σ channel while $d_{x^2-y^2}$ states cannot appear under π illumination. Since d_{xz} and d_{yz} orbitals are not eigenstates of the mirror operator, electronic states along $\overline{\Gamma M}$ are formed by even ($d_{xz} + d_{yz}$) and odd ($d_{xz} - d_{yz}$) linear combinations and will thus be visible under both polarizations. In figures 5.9 and 5.10, bands with vanishing matrix element are colored light grey, while bands with nonzero matrix element remain black.

For LSCO, the $d_{3z^2-r^2}$ band width is roughly 0.5 eV with a band maximum at the M-point (-0.8 eV). The crossing of the $d_{3z^2-r^2}$ and

Table 5.4: Connection between the orbital mirror symmetries and photoemission matrix elements. The first row gives the eigenvalues with respect to a mirror at the nodal plane M_{xy} for the d-orbitals in a basis in which M_{xy} is diagonal. The last two rows contain the photoemission matrix element as a function of d-orbital and incident light polarization. A denotes the magnitude of the electromagnetic vector potential. The polarization vector $\boldsymbol{\epsilon}_\sigma$ ($\boldsymbol{\epsilon}_\pi$) is perpendicular (parallel) to the analyzer plane and thus corresponds to σ-polarized (π-polarized) light of *odd* (*even*) character. The final state $\langle f|$ is assumed to be a plane wave of *even* character.

j	x^2-y^2	$3z^2-r^2$	xy	$xz+yz$	$xz-yz$
$\langle d_j\vert M_{xy}\vert d_j\rangle$	-1	$+1$	$+1$	$+1$	-1
Character	odd	even	even	even	odd
$\langle f\vert A\boldsymbol{\epsilon}_\sigma\vert d_j\rangle$	$\neq 0$	0	0	0	$\neq 0$
$\langle f\vert A\boldsymbol{\epsilon}_\pi\vert d_j\rangle$	0	$\neq 0$	$\neq 0$	$\neq 0$	0

$d_{x^2-y^2}$ bands, constituting a type-II Dirac line node, is protected by mirror symmetry [1, 157] (see also section 5.2.2). For Bi2201 and Tl2201, the $d_{3z^2-r^2}$ band is pushed to lower energies and an overall smaller $d_{3z^2-r^2}$ band width is found. As a result, the nodal crossing of the $d_{3z^2-r^2}$ and $d_{x^2-y^2}$ bands is not found for Bi2201 and Tl2201. The type-II Dirac line node is thus unique to LSCO [1]. We also notice that in LSCO, the $d_{3z^2-r^2}$ band lies above the t_{2g} bands whereas the opposite is true for Bi2201 and Tl2201. Finally, in comparison to LSCO, the bottom of the $d_{x^2-y^2}$ band is closer to the Fermi level in Tl2201.

5.3.3 Discussion

We list the following three main obvservations: (i) clear identification of the $d_{3z^2-r^2}$ band position in three of the mentioned compounds,

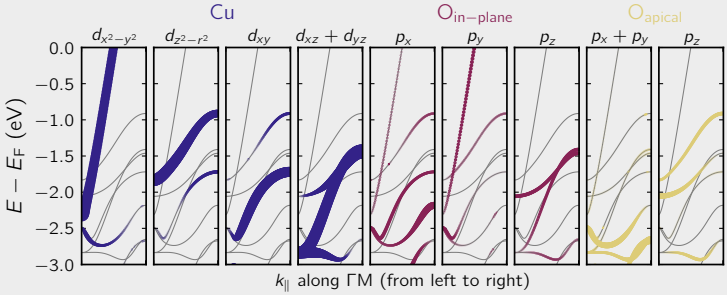

Figure 5.11: Nodal DFT band structure for LSCO with orbital character assignments. There is one panel for each contributing orbital from the Cu, apical and in-plane O atoms, as indicated. The marker area (linewidth) is proportional to the weight of the respective orbital.

(ii) compound dependence of the $d_{x^2-y^2}$ band bottom positions and (iii) the t_{2g} (d_{xy}, d_{xz} and d_{yz}) band positions at the zone corner. These experimental observations are quantified as a function of apical oxygen distance d_A and compared directly to DFT calculations. Generally, excellent quantitative agreement between DFT and experimental band structures is found. It is therefore concluded that even though DFT does not capture low-energy self-energy effects, it is successfully describing the global band structure of the cuprates.

The polarization dependence of the band which crosses the Fermi level allows us to assign it uniquely to the $d_{x^2-y^2}$ orbital in all studied compounds. For Bi2201, the next band below the Fermi level is found in both the σ and π channels and hence can be assigned to the d_{xz}, d_{yz} orbitals. The flat band found around -1.8 eV in the π channel has to have either d_{xy} or $d_{3z^2-r^2}$ character. For a unique orbital assignment we stress the following facts: (i) Resonant inelastic x-ray scattering (RIXS) measurements of the dd-excitations have found the $d_{3z^2-r^2}$ states at -2 eV and below the d_{xy}, d_{xz}, d_{yz} states [158]. (ii) As the

d_{xy} orbital extends purely in the xy-plane, the d_{xy} band is generally expected to disperse strongly along the nodal direction. This is indeed confirmed by our DFT calculations. Combined, this lets us assign the -1.8 eV band in Bi2201 to the $d_{3z^2-r^2}$ orbital. As previously discussed in referece [76] and shown in figures 5.9 and 5.11 the $d_{3z^2-r^2}$ band is clearly identified in La-based cuprates. In the case of Tl2201, by contrast, no evidence for the $d_{3z^2-r^2}$ band is found down to -3 eV. Therefore, either the $d_{3z^2-r^2}$ band in Tl2201 is pushed to even lower binding energies or this band is too faint to be observed. The latter scenario is supported by the fact that in PLCCO with no apical oxygen, the $d_{3z^2-r^2}$ band is found at around -2.5 eV [see figure 5.9 (h)]. We thus conclude that the $d_{3z^2-r^2}$ band in Tl2201 is either of very low intensity or pushed to even lower energies.

We plot the observed $d_{3z^2-r^2}$ band position at the M-point as a function of the compound dependent ratio between apical oxygen distance d_A and in-plane lattice constant a (figure 5.12). Furthermore, the $d_{x^2-y^2}$ band bottoms and the energies of the t_{2g} bands at the zone corner M are plotted alongside their respective positions found from our DFT calculations. One can see that the calculations capture the most salient band structure trends: (i) DFT correctly predicts how the $d_{3z^2-r^2}$ band position — with respect to the Fermi level — evolves as a function of d_A/a. (ii) DFT yields the right trends for the band widths of both the $d_{3z^2-r^2}$ and $d_{x^2-y^2}$ bands. For example, the $d_{3z^2-r^2}$ band width is gradually reduced when going through the series LSCO $\rightarrow$ Bi2201 $\rightarrow$ Tl2201. The ARPES data on LSCO and Bi2201 supports that trend. For the $d_{x^2-y^2}$ band, ARPES only reveals the occupied part. Instead of band width, it thus makes more sense to consider the band bottom. It turns out that the $d_{x^2-y^2}$ band minimum is varying across LSCO, Bi2201, and Tl2201 and the positions agree between DFT and experiment. (iii) The t_{2g} band position at the zone corner also follows the trend of moving closer to E_F with increasing d_A/a, both in experiment and the DFT calculations. However, we stress that because the DFT methodology does not include electron interactions,

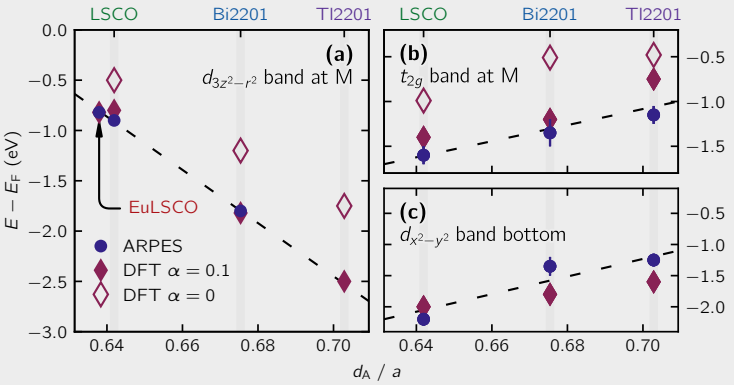

Figure 5.12: Band structure characteristics versus ratio between apical oxygen distance and (tetragonal) in-plane lattice constant d_A/a. Blue points represent the ARPES experiments whereas results from our DFT calculations are indicated by red diamonds. The empty diamonds show how regular DFT is not able to quantitatively describe the band structure. The includsion of 10 % of exact exchange ($\alpha = 0.1$, filled diamonds) reproduces the experimental observation for all studied compounds. Dashed lines represent guides to the eye. **(a)** $d_{3z^2-r^2}$ band position at the M point versus d_A/a. **(b)** Position of the t_{2g} band at the zone corner M versus d_A/a. Mean values of the d_{xy}, $d_{xz}+d_{yz}$ and d_{xz}-d_{yz} band positions at M are taken for the DFT points. **(c)** $d_{x^2-y^2}$ band bottom as function of d_A/a.

it cannot capture self-energy effects such as the much discussed nodal waterfall structure [159–161].

The observed trends that were just discussed can be intuitively understood by considering the influence of the crystal electric field (CEF) on the electronic states at the Cu sites. The Cu atoms are embedded in an octahedral environment by their nearest neighbor O

atoms (figure 5.6). The situation in PLCCO can be understood as an octahedral environment where the apical O atoms are infinitely far away. The relevant orbitals for our consideration are $d_{x^2-y^2}$ and $d_{3z^2-r^2}$. The spatial extent of these orbitals differs radically, as can be seen in figure 5.13 (a) and (b). While the *lobes* of the $d_{x^2-y^2}$ orbital are directed towards the in-plane nearest neighbor oxygen atoms, the $d_{3z^2-r^2}$ orbital points along the z axis at the apical oxygen atoms. With this consideration in mind it is immediately clear that any change in the apical oxygen distance d_A — while keeping the in-plane lattice constant fixed — will have a more pronounced effect on $d_{3z^2-r^2}$ orbital as it is more directly subjected to the electrostatic repulsion of the apical oxygen's electrons. This is why an increase in d_A/a allows $d_{3z^2-r^2}$ to relax to lower energies (higher binding energies), as is schematically sketched in figure 5.13 (c).

As for the t_{2g} orbitals, the situation is less easily explained using this simple picture. The spatial extent of d_{xz} and d_{yz} is most prominent towards the edges of the octahedron, meaning that a value of d_A/a increasingly different from 1 exposes them to an increasingly asymmetric CEF, which is energetically less favourable. Actually going through the CEF calculation confirms this expectation and the experimentally observed result.

5.4 Conclusions

The new results that have been discussed in this chapter show that even after decades of research on cuprate HTSCs, there is still a lot to learn. The discovery of the $d_{3z^2-r^2}$ band in LSCO and its interplay with the $d_{x^2-y^2}$ band that crosses the Fermi level has opened the door to a set of new realizations. The subsequent studies, have shown that oxides may host Dirac fermions and that the band structures of LSCO and Eu-LSCO are in fact not quasi-2D but show finite k_z-dispersions. Furthermore, we have carried out a comprehensive ARPES and DFT study of the band structure across single layer cuprate SCs.

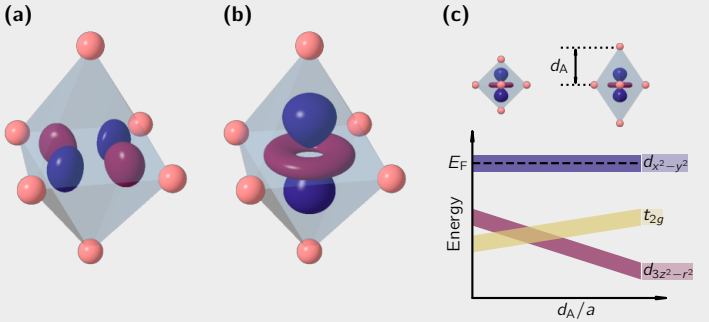

Figure 5.13: Influence of the CEF on different electronic states. **(a)** CuO_2 octahedron with oxygen atoms (bright red) at the corners, connected by transparent planes as guides to the eye. At the Cu site, the spatial distribution of the $d_{x^2-y^2}$ orbital is drawn in a typical manner where the different colors stand for different signs of the wave function. **(b)** $d_{3z^2-r^2}$ orbital inside the CuO_2 octahedron. While the lobes of $d_{x^2-y^2}$ point towards the in-plane nearest neighbors, those of $d_{3z^2-r^2}$ are directed at the apical oxygen atoms. **(c)** Schematic energy level diagram depicting the influence of d_A/a in the d orbitals.

Through light polarization analysis, we were able to identify both the e_g ($d_{x^2-y^2}$ and $d_{3z^2-r^2}$) and t_{2g} bands and their band positions and band widths were compared to DFT calculations. The observed results match the expectations from crystal field theory considerations and the relative position between the $d_{x^2-y^2}$ and $d_{3z^2-r^2}$ bands may be partially responsible for the variation of the superconducting transition temperature T_c within this family of compounds.

The excellent agreement between DFT and experimental results led us to conclude that the DFT methodology with proper choice of mixed in exchange-correlation functional does capture the global electronic

structure of the overoped cuprates. Furthermore, the paramater α for the mixing in of the exchange-correlation energy appears to be a constant across all measured compounds, which allows us to propose that this value might be universally constant across overdoped cuprate SCs, shaking the previous paradigm that DFT was unfit to describe the cuprates.

Chapter 6: Spectroscopic Fermi liquid universality in oxides

The broad range of studies on cuprate high-temperature superconductors presented and discussed in chapter 5 has reveiled numerous new aspects on this heavily investigated material family. Beside the previously layed out results, a striking difference in certain physical properties is observed between the electron-doped and the hole-doped sibling . While chapter 5 was focused on the overall electronic structure, the present chapter takes a closer look at

some of these differences with a focus on the self-energy. After an introduction and a technical review of the used methods in sections 6.1 and 6.2, we present the results of our experiments and analysis in section 6.3. The following discussion in section 6.4 culminates in the formulation of a spectroscopic version of the Kadowaki-Woods relation, before the chapter is summarized in section 6.5.

The results presented in this chapter have been published in a peer-reviewed journal [4]. My contributions as a second author to that publication include collaboration in the preparation and execution of the experiments, inputs to the manuscript and discussions about the self-energy analysis and results.

6.1 Introduction

The Kadowaki-Woods relation reviewed in section 3.3.3 connects the quasiparticle (QP) scattering rate (or inverse lifetime) to the effective mass in a unifying manner across correlated systems of different material families. It is usually formulated in terms of the Sommerfeld constant γ and the coefficient A in the resistivity which appear in the electronic specific heat and resistivity, as in equations (3.20) and (3.21). As such, the relation is a statement about macroscopic experimental observables. As these observables are a result of collective microscopic phenomena, one could imagine to detect a more direct signature of the underlying physics through microscopic probes such as angle-resolved photoemission spectroscopy (ARPES). In particular, while resistivity and specific heat measurements yield k-space integrated results, ARPES might unveil a potential k dependence of the relation. Despite its k resolution capability and direct access to the self-energy (section 4.2), no such spectroscopic evidence of the Kadowaki-Woods relation has been established. This lack of progress stems from a chain of challenges that have been partially mentioned in earlier chapters: (i) Photoemission spectroscopy is best suited for two dimensional (2D) systems [38], narrowing down the range of studiable materials. (ii) Self-energy analysis of quasi 2D systems is limited by residual k_z and disorder broadening [141] in the weak coupling limit. (iii) The strong coupling limit leads to energy scales below the resolving power.

In the course of the broad range of experiments that have been carried out on cuprate high-temperature superconductors (HTSCs) within the Laboratory for Quantum Matter Research (LQMR), as has been described in chapter 5, we have uncovered first indications for a spectroscopic Kadowaki-Woods relation. In the following, we demonstrate by soft x-ray ARPES (SX-ARPES) that the electron-overdoped cuprate superconductor (SC) $Pr_{2-x-y}La_xCe_yCuO_4$ (PLCCO) has a 2D electronic structure with negligible k_z dispersion. This result justifies and enables extraction of the in-plane self-energy using with visible

to ultraviolet energies (VUV-ARPES). In contrast to hole-overdoped $La_{2-x}Sr_xCuO_4$ (LSCO), which hosts non-local interactions [147, 162], an essentially momentum-isotropic Fermi liquid self-energy is found from the nodal to antinodal region. Again in direct comparison to LSCO, much weaker electron-electron interactions are observed in PLCCO. This result is reflected both in QP lifetime τ and Fermi liquid cut-off energy scale ω_c, which is linked to the mass renormalization factor Z [which was defined in equation (3.13) of chapter 3]. Along with results on other correlated (non-superconducting) oxide systems, these findings combine to form a spectroscopic version of the Kadowaki-Woods relation where the QP scattering rate β scales with Z^{-2} over more than an order of magnitude. This relation therefore connects weakly and strongly correlated Fermi liquids via a single energy scale.

6.2 Methods

Single crystals of PLCCO with $x = 0.15$ were synthesized by the traveling-solvent floating zone method. The sample was reduction annealed using the protect-annealing method [163, 164]. After reduction annealing at 800 °C for 24 h, the present overdoped sample showed superconductivity with $T_c = 19$ K — lower than the optimal $T_c \sim 27$ K [164]. The quality of our crystal is reflected by a residual resistivity $\rho_0 = 38$ $\mu\Omega$cm.

SX-ARPES and ARPES using visible to ultraviolet energies (VUV-ARPES) experiments were carried out at the P04 and Surface/Interface Spectroscopy (SIS) beamline at DESY [165] and Swiss Light Source (SLS) [166], respectively. Samples were cleaved *in situ* under ultra high vacuum (UHV) ($p < 5 \times 10^{-11}$ Torr) conditions by employing a top-post method. Circularly polarized incident photons of energies $h\nu$ from 30 eV to 600 eV were used for both experiments. The effective energy resolution (temperature) was set to ~ 50 meV (25 K) for the SX-ARPES and 14 meV to 17 meV (18 K) for the VUV-ARPES measurements. For both setups, the angular resolution is ~ 0.15 degrees.

All data were recorded at the cleaving temperature 25 K and 18 K for the SX-ARPES and VUV-ARPES measurements, respectively.

6.3 Results

Using SX-ARPES, which provides comparatively good k_z-resolution [149], we evaluate the dimensionality of the electronic structure in PLCCO. Along the nodal and off-nodal cuts [see in-plane Fermi surface map (FSM) in figure 6.1 (a)], the Fermi surface (FS) was investigated in the k_z direction over three Brillouin zones (BZs) [figure 6.1 (b) and figure 6.2 (b)]. With a probing depth of 10 Å, the k_z broadening amounts to $\sim 0.2\,\pi/c'$ where c', as in section 5.2.3, represents the CuO_2-layer spacing ($c' = c/2$). Within experimental resolution, the FS (with $d_{x^2-y^2}$ character) has no k_z dispersion. Consistently, none of the t_{2g} and d_{z^2} bands observed at deeper binding energies (confer chapter 5 exhibit any significant dispersions along the k_z direction (not shown). These highly 2D characteristics of PLCCO are in stark contrast to the recently unveiled three dimensional (3D) electronic structure of the hole-overdoped cuprate LSCO [2, 76] (section 5.2.3). This difference stems from a reduced inter-layer hopping due to the absence of apical oxygen atoms in the electron-doped cuprates [167, 168]. The 2D nature of the electron-doped cuprates is also reflected by a large resistivity anisotropy $\rho_c/\rho_{ab} > 10\,000$ [169]. This is ten and hundred times larger than the anisotropies reported in Sr_2RuO_4 [170] and overdoped LSCO [171], respectively.

The established 2D electronic structure of PLCCO justifies use of surface-sensitive VUV light for extraction of the self-energy. The FS recorded at $h\nu = 55$ eV [figure 6.3 (a)] — essentially identical to that observed with SX-ARPES [figure 6.1 (a)] — corresponds to a filling of 15 % electron doping. While there have been extensive reports on additional electron doping by reduction annealing of electron-doped cuprates [164, 172–176], this filling is consistent with the nominal Ce concentration.

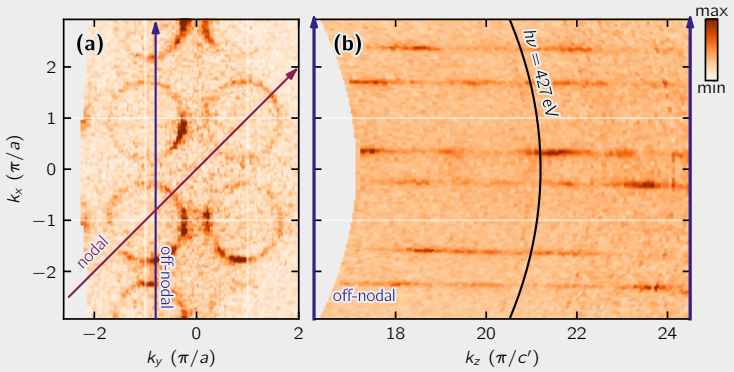

Figure 6.1: 2D FS of PLCCO ($x = 0.15$). **(a)** In-plane FSM, for the integration window $E_F \pm 30$ meV, measured at $T = 25$ K and $h\nu = 427$ eV. **(b)** Out-of-plane FSM recorded along the off-nodal direction as indicated in (a).

The 2D FS and the absence of (i) hot spots [177] and (ii) a van Hove singularity (VHS) near the FS form the basis for self-energy analysis across the entire BZ. Low-energy QP excitations were recorded along nodal and antinodal directions [see figure 6.3 (a)]. Nodal and antinodal EDMs shown in figure 6.3 (b) and (c), recorded with $h\nu = 55$ eV and 30 eV incident light, respectively, reveal sharp and dispersive QP peaks. In agreement with previous studies [178–180], both dispersions exhibit (possibly electron-phonon coupled) kinks at the binding energy of ~ 0.05 eV [figure 6.4 (a)].

Fermi velocities v_F — plotted as a function of the FS angle φ in figure 6.4 (b) — are extracted by fitting the QP dispersion up to the kink energy scale. In contrast to the strongly anisotropic v_F in overdoped LSCO ($x = 0.22$) [153], v_F is found to be almost independent of momentum in PLCCO. This marked difference is directly linked to the proximity of the VHS to the Fermi level in LSCO [181].

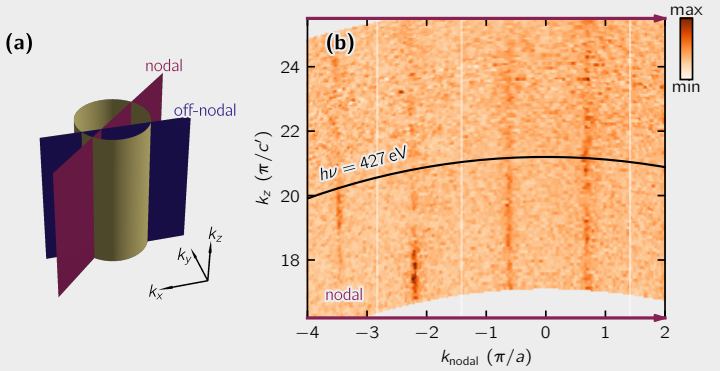

Figure 6.2: 2D FS of PLCCO (continued). **(a)** Schematic of the FS (green cylinder) and the nodal and off-nodal out-of-plane cutting planes as they appear in (b) and figure 6.1 (b), respectively. **(b)** Out-of-plane Fermi surface map recorded along the nodal direction as indicated in figure 6.1 (a).

As discussed in section 4.2, ARPES spectra contain information about the electronic self-energy $\Sigma(\mathbf{k},\omega)$ through their relation to the spectral function $A(\mathbf{k},\omega) = -1/\pi\ \mathrm{Im}[1/(\omega - \varepsilon_\mathbf{k} - \Sigma(\mathbf{k},\omega))]$ where $\varepsilon_\mathbf{k}$ is the bare band dispersion. The QP lifetime is obtained through

$$\mathrm{Im}\,\Sigma(\mathbf{k},\omega) = v_\mathbf{k}\Gamma_\mathbf{k} \tag{6.1}$$

where

$$v_\mathbf{k} = \frac{\partial\varepsilon_\mathbf{k}}{\partial\mathbf{k}} \tag{6.2}$$

is the bare band velocity and $\Gamma_\mathbf{k}$ is the MDC half width at half maximum [40, 182, 183]. In our case, the nodal MDC linewidth yields a mobility

$$\mu = e/(\hbar k_\mathrm{F}\Gamma_\mathbf{k}) = 14.3\,\mathrm{cm}^2/\mathrm{Vs} \tag{6.3}$$

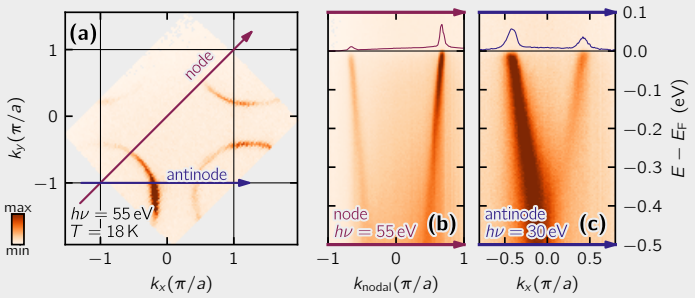

Figure 6.3: Presentation of VUV-ARPES data on PLCCO. **(a)** Fermi surface recorded at the indicated temperature and photon energy. **(b)**,**(c)** Nodal and antinodal energy distribution maps (EDMs). Different photon energies are used to enhance different matrix elements. Solid lines are the momentum distribution curves (MDCs) at the Fermi level. The MDC linewidth and Fermi velocities yield $\mathrm{Im}\,\Sigma(0) \sim 0.077\,\mathrm{eV}$ and $0.085\,\mathrm{eV}$ respectively for the nodal and antinodal direction.

(see Ref. [184]), consistent with that inferred from electron transport experiments

$$\mu = (ne\rho_0)^{-1} = 13.9\,\mathrm{cm}^2/\mathrm{Vs} \tag{6.4}$$

using $n = 1.15$ per Cu atom and residual resistivity $\rho_0 = 38\,\mu\Omega\,\mathrm{cm}$.

To estimate the bare band velocity, we fit the FS to the following single-band tight binding (TB) model:

$$\begin{aligned}\varepsilon(\mathbf{k}) =& \varepsilon_0 - 2t(\cos\, k_x a + \cos\, k_y a) \\ & - 4t'\cos\, k_x a\, \cos\, k_y a - 2t''(\cos\, 2k_x a + \cos\, 2k_y a) \quad ,\end{aligned} \tag{6.5}$$

which includes nearest (t), second-nearest (t'), and third-nearest (t'') neighbor hopping parameters. With ε_0 being the band center, we find $\varepsilon_0/t = -0.04$ and $t'/t = -0.19$ when using $t''/t' = -1/2$. Assuming $t = 0.41\,\mathrm{eV}$ based on a previous density functional theory (DFT)

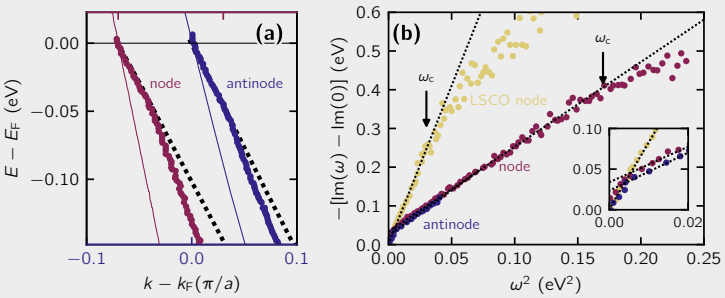

Figure 6.4: In-plane isotropic self-energy structure of PLCCO. **(a)** Nodal and antinodal band dispersions extracted from MDC analysis. Solid curves and dashed lines represent bare bands and extrapolation of low-energy dispersions, respectively. **(b)** Near nodal self-energy $-\,\mathrm{Im}\,\Sigma(\omega)$ plotted versus ω^2 for PLCCO and LSCO ($x = 0.23$) [147]. Dotted curves are fits revealing the $-\,\mathrm{Im}\,\Sigma(\omega) \propto \beta\omega^2$ dependence and black arrows mark high-energy deviation (Fermi liquid cut-off ω_c). The low-energy part is magnified in the inset.

estimate on $Nd_{2-x}Ce_xCuO_4$ [185], the full 2D bare band structure is obtained. This enables extraction of the self-energy $\mathrm{Im}\,\Sigma(\mathbf{k}, \omega)$ as illustrated for cuts through node and antinode in figure 6.4 (b). ARPES spectra were recorded up to a binding energy of 0.5 eV. However, the antinodal $\mathrm{Im}\,\Sigma(\omega)$ is plotted only for $\omega^2 < 0.04\,\mathrm{eV}^2$ as analysis above this energy scale is challenged by a VHS [186].

6.4 Discussion

Both the nodal and antinodal $\mathrm{Im}\,\Sigma(\omega)$ curves display a kink at $\omega \sim 0.06$ eV [see inset of figure 6.4 (b)], Kramers-Kronig consistently with the kink observed in the band dispersion. Below this phonon cut-off energy scale $\omega_{ph} \approx 0.06$ eV, the self-energy is expected to contain

contributions from both electron-phonon and electron-electron interactions. Probing in the $\omega \to 0$ limit allows — in principle — direct comparison to low-temperature transport properties [68, 187, 188]. With our experimental temperature and energy resolution, however, we cannot distinguish a Fermi liquid with $\mathrm{Im}\,\Sigma \propto \omega^2$ from, for example, a marginal Fermi liquid with $\mathrm{Im}\,\Sigma \propto \sqrt{\omega^2 + (\pi k_B T)^2}$ [91].

Excitations observed above the kink energy scale (0.06 eV) do not pose these limitations and hence offer direct insight into the electron-electron interactions. As electron-phonon self-energy contributions saturate for $\omega > \omega_{ph}$ the electron-phonon interactions are thus effectively filtered out of the analysis. Furthermore, our energy resolution does not limit the analysis of the QP excitations in this regime. The extracted electron-electron interacting self-energy is parametrized by $\mathrm{Im}\,\Sigma(\omega) = -\alpha - \beta\omega^2$, with α and β being constants. This parameterization implicitly assumes that different scattering channels (electron-disorder, electron-phonon and electron-electron etc.) are additive. A similar premise is used for analysis of resistivity measurements on related electron-doped cuprates [68]. As demonstrated in figure 6.4 (b), this parabolic function convincingly fits the $\mathrm{Im}\,\Sigma(\omega)$ curves over a wide energy range ($0.06\,\mathrm{eV} < \omega < 0.4\,\mathrm{eV}$).

This functional form of the self-energy is identical to a 3D Fermi liquid which displays $\mathrm{Im}\,\Sigma(\omega) - \mathrm{Im}\,\Sigma(0) = -\beta\omega^2$ below a cut-off energy ω_c [72, 147, 189, 190]. In two dimensions, a logarithmic correction [191] influences mostly the self-energy for $\omega \ll \varepsilon_F \sim 1.5\,\mathrm{eV}$ [3] and an approximate $\mathrm{Im}\,\Sigma(\omega) \propto \beta'\omega^2$ dependence remains in the considered ω range while β' is weakly overestimating β. The coefficient $\beta = \lambda/\omega_c^2$ — given by the bare scattering rate λ and ω_c — reflects the effective electron-electron interaction strength. In figure 6.5 (b), β plotted against the FS angle φ appears essentially isotropic, i.e. momentum independent. This is in strong contrast to the hole-overdoped counterpart LSCO where β is highly anisotropic and takes on much larger values already in the nodal region [see again figure 6.5 (b)]. This weaker electron correlation strength found for electron-overdoped

cuprates is consistent with theoretical proposals [192–195].

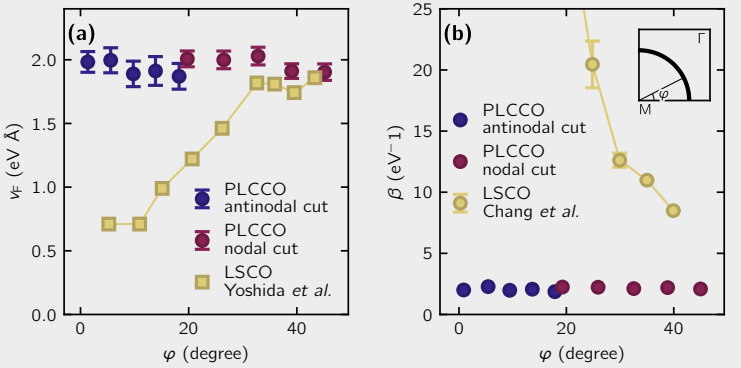

Figure 6.5: In-plane isotropic self-energy structure of PLCCO, continued. **(a)** Fermi velocity v_F of PLCCO and LSCO ($x = 0.22$) (Yoshida *et al.* [153]) plotted as a function of the FS angle φ [see inset of panel (b)]. **(b)** Coefficient β for the ω^2 term of $\mathrm{Im}\,\Sigma(\omega)$ for PLCCO and LSCO ($x = 0.23$) (Chang *et al.* [147]).

We conclude by discussing the Fermi liquid cut-off energy scale ω_c which is expected to vanish with the QP residue Z [72, 189, 190]. For the simplest Fermi liquid with isotropic $\mathrm{Im}\,\Sigma$ (a *local* Fermi liquid), the residue is given by $Z = v_F/v_b$. If $\mathrm{Im}\,\Sigma$ in addition is monotonically decaying to zero above the cut-off energy ω_c, then $Z \propto \omega_c/W$ where W is a bare band energy scale [72]. Hence the cut-off energy ω_c is an indicator of electron-electron interaction strength. The bandwidth normalization enables comparison of different material classes. However, heavy fermion systems in the limit $Z \to 0$ typically have ω_c far below the instrumental energy resolution. This concern is irrelevant for PLCCO as weak interactions manifest as a large Fermi liquid cut-off energy scale. As shown in figure 6.4 (b), $\omega_c \sim 0.4\,\mathrm{eV}$ ($\omega_c^2 \sim 0.16\,\mathrm{eV}^2$) in PLCCO is twice as large as that of the nodal region in overdoped LSCO [146,

147]. However, in LSCO the self-energy is not isotropic and for both LSCO and PLCCO, $\mathrm{Im}\,\Sigma \propto \omega$ for $\omega > \omega_c$. This implies that neither $Z = v_F/v_b$ nor $Z \propto \omega_c/W$ is expected to hold true. Instead, a Kramers-Kronig transformation of $\mathrm{Im}\,\Sigma$ suggests $Z \propto \ln^{-1}(W/\omega_c)$ in the limit $\omega_c \to 0$ [89].

From a single ARPES spectrum, it is generally not possible to determine whether Z is proportional to ω_c or $\ln^{-1}(W/\omega_c)$. We therefore resort to fundamental property of Fermi liquids underlying the Kadowaki-Woods relation. That is, QP lifetime and mass renormalization are expected to scale — at least for comparable materials. Transport and thermodynamic experiments do support the Kadowaki-Woods relation [72], though multi-band physics allows for numerous exceptional cases [196]. ARPES experiments have the advantage of extracting QP lifetime and mass renormalization not only from the same band but also from a very narrowly defined momentum region. The fact that both β and ω_c are linked to the electron-electron scattering rate and QP mass, respectively, prompts us to attempt a spectroscopic analogue to the Kadowaki-Woods relation. In doing so, we here focus on transition-metal oxides with perovskite-based crystal structures ranging from pseudo-cubic ($LaNiO_3$) [197] to tetragonal (LSCO and PLCCO) and orthorhombic ($Ca_{1.8}Sr_{0.2}RuO_4$ (CSRO)). We stress that the extremely strongly correlated regime, represented by U- and Ce-based heavy fermion systems, is expected to have $\omega_c \to 0$ falling below our energy resolution.

Within our selected material class, we are seeking a relation between the electron scattering factor β and the QP mass renormalization factor Z^{-1}. In figure 6.6, we thus plot $W\beta$ versus $\ln^2(W/\omega_c)$ with W being a quarter of the DFT bandwidth [185, 198–200] for PLCCO, LSCO, $LaNiO_3$ [197] ($d_{x^2-y^2}$ band [201]) and CSRO (d_{xz}/d_{yz} band). An overview of the self-energy analysis of CSRO is presented in figure 6.7. Combined, these correlated metals follow $W\beta \propto \ln^2(W/\omega_c)$ over more than an order of magnitude on both axes.

This spectroscopic analogue of the Kadowaki-Woods relation sug-

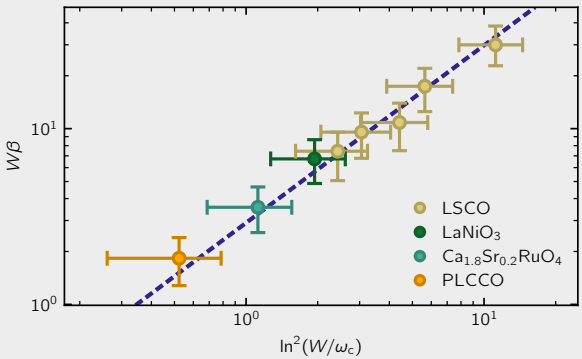

Figure 6.6: Spectroscopic Kadowaki-Woods relation. $W\beta$ versus $\ln^2(W/\omega_c)$, where β is the prefactor in $-\mathrm{Im}\Sigma(\omega) \propto \beta\omega^2$, ω_c is the Fermi liquid cut-off energy, and W is a bare energy scale for LSCO ($x = 0.23$) [147], $LaNiO_3$ [197], CSRO, and PLCCO ($x = 0.15$). See section C.4 for table values of β, ω_c, and W. The LSCO data points stem from different Fermi momenta. The dashed line is a linear fit of the plotted data. Error bars are set by assuming 20 % of uncertainty on the used bare-band velocities.

gests a logarithmic connection between the Fermi liquid cut-off energy scale and the QP mass renormalization factor Z^{-1}. The Fermi liquid properties (QP lifetime and mass) are thus set by a single energy scale; the Fermi liquid cut-off ω_c that smoothly connects weakly and strongly correlated Fermi liquids.

6.5 Conclusions

In summary, we have carried out SX-ARPES and VUV-ARPES measurements on the electron-overdoped cuprate compound PLCCO. A 2D electronic structure was revealed by SX-ARPES experiments. This

in turn enabled precise determination of PLCCO's in-plane self-energy using VUV light. In contrast to the hole-doped counterpart LSCO, PLCCO displayed weak momentum-isotropic Fermi liquid excitations. Characteristic parameters such as the scattering-rate coefficient β and the Fermi liquid cut-off energy ω_c revealed weak electron correlations compared to those reported in LSCO and CSRO, but close to $LaNiO_3$. Despite these strong contrasts, the four systems were found to satisfy a common relation that connects β to ω_c^{-1}, and hence to the mass renormalization factor Z^{-1}. Our results constitute a spectroscopic version of the Kadowaki-Woods relation $\beta \propto Z^{-2}$. We reveal how this relation emerges from the QP lifetime and mass being set by a single energy scale ω_c that characterizes all Fermi liquids.

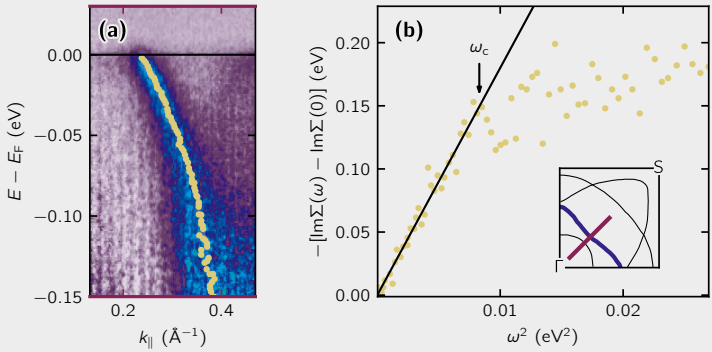

Figure 6.7: Self-energy $-\mathrm{Im}\,\Sigma(\omega)$ of CSRO. **(a)** ARPES spectrum of CSRO taken along the cut indicated in the Fermi surface schematic shown in the inset of panel (b). The highlighted band in the inset is analyzed. Points indicate peak positions in MDC fits. **(b)** Self-energy $-\mathrm{Im}\,\Sigma(\omega)$ of CSRO plotted as a function of ω^2. The Fermi liquid cut-off is marked by a black arrow.

Chapter 7: ARPES insights into the heavy fermion compound $CeRu_2Si_2$

In this chapter we present novel angle-resolved photoemission spectroscopy (ARPES) results obtained on $CeRu_2Si_2$, a representative of the heavy fermion family. Section 7.1.1 introduces this diverse family and gives a broad overview. It ends with a summary of the existing work on $CeRu_2Si_2$. Section 7.2 then lays out and discusses our ARPES data and how it has enabled us to assign clear orbital characters to the dominant conduction bands. In combination

with calculations of the orbital overlaps between conduction and f electrons we provide an explanation for the observed structures in the Fermi surface map and their temperature driven reconstruction.

We are currently in the course of preparing the content presented in this chapter for publication in a peer-reviewed journal. The results and discussions should therefore be regarded as preliminary and are subject to change. For this project, I have led the preparation and conduction of the experiments as well as the analysis of the data. Beyond the fantastic support from the Laboratory for Quantum Matter Research team, I am grateful for fruitful discussions with Daniel Mazzone, Nicolas Gauthier and Rina Tazai, who has contributed the calculations of the relevant orbital overlaps (section 7.3).

7.1 Introduction

7.1.1 Kondo lattices and heavy fermions

The electrical resistivity of metals is usually found to decrease monotonically with decreasing temperature. This can be intuitively understood, because the resistivity is typically dominated by phonon scattering, which is suppressed at low temperatures. In the early 1930's it was observed, however, that in some metals resistivity reached a minimum at a finite temperature, before it increases again when approaching absolute zero (figure 7.1). A satisfactory explanation for this behaviour could be given by Jun Kondo in 1964 [202] after significant work by Anderson [203] and others.

The proposition was that the effect was caused by impurity atoms that are randomly situated within the crystal lattice. Kondo assumed that these impurities would effectively act as local magnetic moments and that there would be an exchange interaction J between these localized moments and the conduction electrons. He showed that, to third order in perturbation theory, this interaction would lead to a diverging electronic scattering term for low T, hence explaining the rise in resistivity. In other words: There is an interaction J between the spins of conduction electrons and localized moments that is insignificant at higher temperatures because the spins are unstable due to thermal fluctuations. The fluctuations subside upon cooling and the spins become more stable for longer periods of time, which allows this spin-interaction J to manifest. The temperature below which this interaction becomes coherent is called the Kondo temperature T_K [204].

When researchers began studying alloys with rare earth elements such as Ce and Yb, the Kondo framework and extensions thereof proved to be applicable to explain many of their outstanding low temperature properties. Some of these compounds possess remarkably large specific heat coefficients that correspond to enormous effective electron masses. In fact, it is found that the electrons (which are fermions) in these compounds behave as if they were a thousand times heavier than

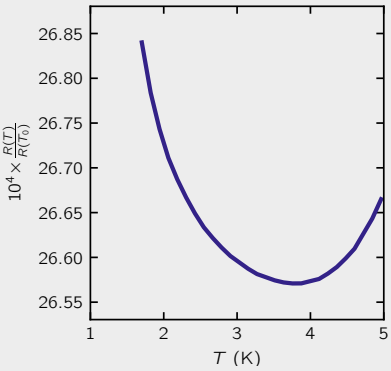

Figure 7.1: Minimum in the electrical resistivity of Au. Adapted from [205].

free electrons: $m^*/m_e \approx 1000$. For this reason, these materials have become known as *heavy fermion compounds* or sometimes as *heavy Fermi liquids* or simply *heavy fermions* [206].

It should be noted that the unifying property for materials that fall into this class really is their high effective mass. This is apparent in figure 3.2 (a), where the heavy fermion compounds are all found at the largest values of $\gamma^2 \propto (m^*)^2$. Meanwhile, there is a huge variance among other characteristics of heavy fermion compounds and the phenomenology they exhibit — they form a highly heterogeneous class [207]: Some heavy fermions order antiferromagnetically (UPt_3 [208]) while others display no long-range order at all ($CeAl_3$ [209], $CeCu_6$ [210]). Some of them are quasi two dimensional (2D) and others show non-Fermi liquid ground state properties. When the hybridization between the localized moments and the conduction electrons opens a gap at the Fermi level, the ground state becomes insulating and we speak of a *Kondo insulator*. Examples for this case are SmB_6 [211, 212], $Ce_3Bi_4Pt_3$ [213], U_2Ru_2Sn [214] and the Kondo semiconductor

YbB_{12} [215]. Other heavy fermion compounds are metamagnetic, meaning that they show an inflection point in their magnetization curve and quantum critical points (QCPs) have been observed in some heavy fermion systems, opening the door for the study of quantum phase transitions [216]. Furthermore, many of the Ce and U based representatives exhibit unconventional superconductivity.

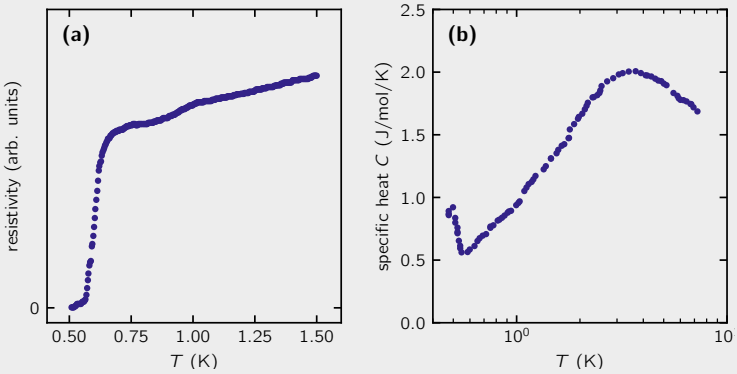

Figure 7.2: Signatures of superconductivity in a heavy fermion compound for $CeCu_2Si_2$. **(a)** Low temperature resistivity showing the drop to 0 which is characteristic for superconductivity. **(b)** Molar specific heat as a function of T with the prominent jump at low temperatures, which is typical for heavy fermion compounds. Adapted from [217].

The latter is of particular interest for two reasons [207]: (i) From a conventional Bardeen-Cooper-Schrieffer (BCS) point of view, superconductivity and magnetism would seem mutually exclusive since the magnetic moments would hinder the formation of Cooper pairs. (ii) The high effective masses m^* exclude the BCS electron-phonon interaction as the pairing mechanism. What makes this even more striking is the fact that in one of the first discovered heavy fermion superconductors, $CeCu_2Si_2$, the magnetic Ce ions that usually suppress

BCS superconductivity seem to be key to its unconventional superconductivity: Even substituting a few of the Ce ions for nonmagnetic La is enough to destroy the superconducting state in $CeCu_2Si_2$ [217].

This great variety of interesting phenomena exhibited by heavy fermion systems has motivated tremendous research effort. The hope of uncovering underlying trends across chemically and physically very different compounds and of making links to other strongly correlated electron systems, such as the cuprate high-temperature superconductors (HTSCs), has fueled countless experimental and theoretical investigations. Numerous variations and expansions of the Anderson and Kondo lattice models as well as dynamical mean field theory (DMFT) approaches have been employed to try and understand these different systems. Simultaneously, the whole toolbox of available experimental methods is being used to shed light on the intriguing problem from all angles. The work presented here constitutes one step, one torch that contributes to the illumination of the unknown.

7.1.2 $CeRu_2Si_2$

One interesting representative of heavy fermion systems is $CeRu_2Si_2$. The coefficient γ of the linear term in the specific heat $C = \gamma T$ at a comparatively small value of $350\,\mathrm{mJ\,mol^{-1}\,K^2}$ [218] corresponds to a large effective mass in the range of $100\,m_e$, similar to that of $CeCu_2Si_2$. However neither superconductivity nor magnetic ordering have been found in $CeRu_2Si_2$ [219, 220]. Still, it has attracted a lot of attention due to its laboratory accessible metamagnetic transition [221, 222] which is believed to be accompanied by an abrupt change of the f electron itineracy [223–225].

Like the related compounds of the family CeX_2Si_2 with $X \in \{Ru, Cu, Rh, Pd, Au\}$ (Ce-122 family), $CeRu_2Si_2$ crystallizes in the body-centered tetragonal (BCT) I/4mmm structure, as drawn in figure 7.3. The corresponding BCT Brillouin zone (BZ) is shown in figure 7.4 (b) and (e).

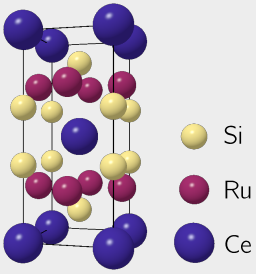

Figure 7.3: Unit cell of the body centered tetragonal crystal structure of $CeRu_2Si_2$. The lattice parameters are $a = b = 4.195\,\text{Å}$ and $c = 9.798\,\text{Å}$.

The members of the Ce-122 series can be sorted according to the level of delocalization or itineracy of the f electrons. Experimentally, this has been achieved by comparing the contributions of the $4f^0$ excitations to the total spectral weight in x-ray absorption spectroscopy (XAS) data [226]. Within that series, $CeRu_2Si_2$ holds the special position of hosting the most itinerant f electrons. Furthermore, it is interesting to note that $CeRu_2Si_2$ is found in close vicinity of $CeCu_2Si_2$ in the J versus T phase diagram [227]. The latter compound hosts unconventional superconductivity while the former does not. Comparing their electronic structure may therefore reveal the key ingredients for this type of unconventional superconductor (SC).

When the Kondo state develops coherence, the hybridization of the nondispersive f states with the conduction electrons (cf hybridization) leads to a bending of the conduction bands. As a consequence, the Fermi wavevector k_F changes, affecting the size of the Fermi surface (FS): Above T_K, the FS is *small* and does not contain the f electrons. A *large* FS that includes the f electrons is formed once the Kondo

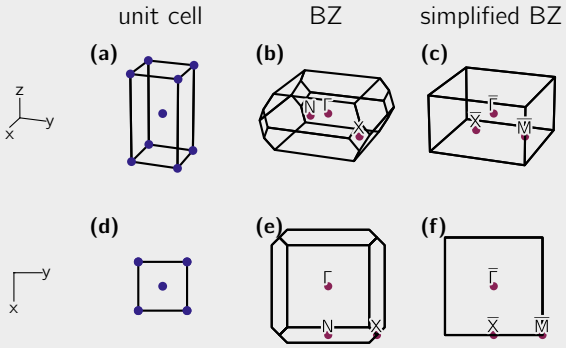

Figure 7.4: Unit cell, body centered and simplified tetragonal Brillouin zones for the I/4 m m m structure with the lattice parameters of $CeRu_2Si_2$ ($a = b = 4.195\,\text{Å}, c = 9.798\,\text{Å}$). The bottom row [(d), (e), (f)] shows the same structures structures as in the upper row [(a), (b), (c)] but seen from the top. from an angular view

state has become fully coherent below T_K. Detailed understanding of this large-to-small FS change is believed to be central in understanding the physics of the Ce-122 compounds [204].

A Compton scattering study has reported indirect evidence for the majority of the FS change taking place near the zone corner $\overline{M}$ [228]. Angle-resolved photoemission spectroscopy (ARPES) and quantum oscillation (QO) measurements provide more direct probes of the FS. However, QO measurements [225] are limited to lowest temperatures and are therefore unfit to observe a FS reconstruction with temperature. Furthermore, these measurements can only account for 20 % of the mass from specific heat experiments [225]. The existing ARPES studies, meanwhile, have only used temperatures far above or in the vicinity of T_K. Our study is therefore motivated by the goal of identifying a temperature driven change in FS topology.

7.2 New ARPES results on $CeRu_2Si_2$

We have conducted ARPES measurements on $CeRu_2Si_2$ crystals at the Cassiopee beamline [229] of SOLEIL synchrotron and the I05 beamline [230] at Diamond Light Source (DLS). In our experiments, we have used a combination of resonant and light polarization dependent ARPES to elucidate the orbital nature of the heavy fermions in $CeRu_2Si_2$. In contrast to earlier ARPES studies [231, 232], we use high-resolution instrumentation to probe the Ce 121 eV Fano resonance [58, 232] (see section 2.3.3) above and below T_K. Strong hybridization between localized f states and conduction bands (cf hybridization) is found around the BZ corner. Furthermore, we observe that the low temperature f electronic spectral weight is strongly suppressed above $tkondo \sim 25\,K$. By exploiting the photoemission matrix element dependence on light polarization, we infer that the cf hybridization occurs predominantly with the e_g states of the Ru sites. In the follwing we will present the obtained data and lay out our line of arguments that has led us to this conclusion.

7.2.1 Methods

High quality single crystals were grown using the Czochralski technique and previously used for magnetoresistance measurements [224, 233]. The crystals were cleaved using a standard top post. Due to the size of the available crystals in the order of $\sim$100 µm and their relative hardness, many iterations were necessary to optimize a sample preparation technique that would lead to reproducible cleaving successes. It is known that cleaving these Ce-122 compounds can lead to Si- or transition metal-terminated surfaces. Surface terminations are distinguished following the spectroscopic experience with related compounds [234]. According to that, the outermost layer of Si atoms in the Si-terminated surface is enough for the Ce $4f$ electrons to be considered in their bulk states. Conversely, in the Ce-terminated surface ARPES effectively probes Ce surface states. A spectroscopic signature of the difference

between the terminations is a stronger enhancement effect of th Ce $4f$ states when going to the 121 eV Fano resonance for Ce termination. Furthermore, in the case of $CeRh_2Si_2$ [234], the dispersion of a Rh derived state around the BZ center $\overline{\Gamma}$ steeply crosses the Fermi level in the Si-terminated surface, while it does not in the other case.

Electrical contact between the crystal and the cryostat was optained using EpoTek H20E Ag epoxy. Incident photon energies of 90 eV (off-resonance) and 121 eV (on-resonance) were used in combination with linear horizontal and vertical light polarizations. A vertical analyser slit configuration was used throughout this work. Data analysis and visualization were carried out using the PIT software package [5].

Following previous ARPES works on Ce-122 systems [235], we are going to label special points according to the projected simple tetragonal BZ boundaries as shown in figure 7.4 (c) and (f).

7.2.2 Data overview

On- and off-resonance ARPES spectra collected along high symmetry directions on a Ce-terminated surface, shown in figure 7.5 (a-c) and (e-g), reveal a rich band structure. Numerous dispersive bands are observed along with the non-dispersive Ce $4f_{7/2}$ state at 0.3 eV binding energy [best seen in figure 7.5 (g)]. The associated on- and off-resonance FSs are displayed in figure 7.5 (d) and (h). Figure 7.6, panels (a) and (e) show on-resonance data along the $\overline{\Gamma}\overline{M}$ direction for a Si-terminated surface and for both, σ and π polarizations. Panels (b) and (f) show the same data at a higher temperature $T_1 = 36$ K. The remaining panels (c), (d), (g) and (h) show intensity difference maps between the ARPES spectra at the temperatures $T_0 = 9$ K and T_1.

Several FS sheets can be identified: a circular pocket around the BZ center $\overline{\Gamma}$ and a flower-shaped feature around the zone corner $\overline{M}$ which is highlighted in panel (h) of figure 7.5. We label the bands that make up these FS sheets as γ (pocket at $\overline{\Gamma}$) and α and β (flower at $\overline{M}$). These bands display a strong dependence on light polarization,

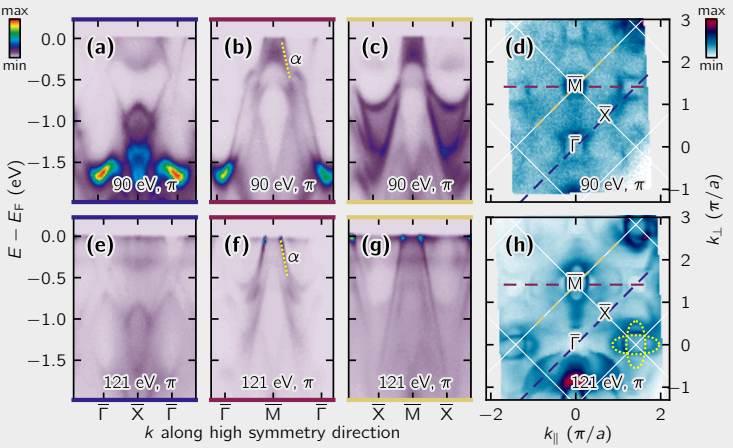

Figure 7.5: High symmetry band structure and FS of $CeRu_2Si_2$ from a Ce-terminated surface. The top row shows obtained off-resonance and the bottom row shows the same regions in k-space but recorded on-resonance, with photon energies as indicated. **(a)**–**(c)** and **(e)**–**(g)** ARPES spectra along high symmetry directions. **(d)**, **(h)** Fermi surface maps (FSMs) with simple tetragonal BZ boundaries overlayed as white lines. Colored dashed lines indicate the high symmetry directions along which band structure is displayed in panels (a-c) and (e-g). Data in this figure was recorded at 13 K.

resonance condition and temperature, as shall be systematically laid out for each band in the following.

The α feature

The dispersive α band displays a pronounced polarization dependence for measurement along the diagonal $\overline{\Gamma}\overline{M}$ direction — it is only visible in the π channel while completely suppressed under σ illumination

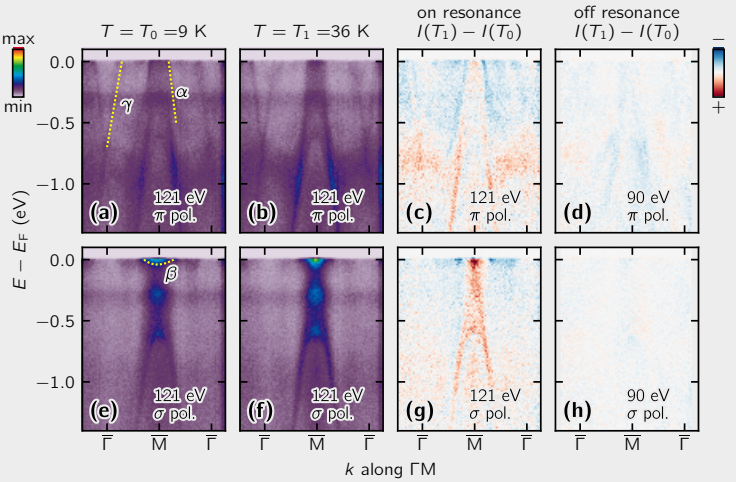

Figure 7.6: Zone corner band structure of $CeRu_2Si_2$ from a Si-terminated FS. **(a)**, **(b)**, **(e)**, **(f)** On-resonance band structure along the $\overline{\Gamma M}$ direction recorded with linear horizontal (π) and vertical (σ) light polarization for temperatures above and below the Kondo temperature T_K. **(c)**, **(d)**, **(g)**, **(h)** Intensitiy differences obtained by subtracting the data at $T_0 = 9\,K$ from the corresponding $T_1 = 36\,K$ data. The color scale is organized such that white indicates no difference. Features that show higher intensity at the higher temperature T_1 appear red while regions of higher intensity at lower temperature T_0 appear blue.

[compare figure 7.6, panels (a) and (e)]. The band therefore must have even character with respect to the diagonal mirror plane. The band also displays a pronounced enhancement under 121 eV illumination, in particular in the vicinity of the Fermi level. To see this, compare panels (b) and (c) of figure 7.5 with panels (f) and (g).

From comparing panels (a) and (b) of figure 7.6 one can already get a hint that the intensity of the α band seems to decrease upon

heating from T_0 to T_1. This is confirmed more clearly in panel (c), where the feature can still be clearly traced and is colored blue, which indicates higher intensity at low temperature. This loss of spectral weight when going from T_0 to T_1 is also visible in the momentum distribution curves (MDCs) at the Fermi level, which are displayed in figure 7.8 (b) and (c).

The β feature

The small pocket β is limited to the σ channel and thus only visible in panels (e) and (f) of figure 7.6. The band bottom is found only $\sim 0.1\,\mathrm{eV}$ below the Fermi level and it crosses E_F just slightly further away from $\overline{\mathrm{M}}$ than the α band. Its strong polarization dependence allows us to assign to it a clear odd character with respect to the diagonal mirror plane.

Like the α band, the Fermi level spectral weight of the β band decreases when the temperature is changed from T_0 to T_1, as is evident from the two blue hot spots in the pseudocolormap of figure 7.6 (g). It is even more clearly visible in the MDCs of figure 7.8 (e) and (f).

The γ feature

An electron pocket is found around the zone center $\overline{\Gamma}$ point. It is visible in the Si termination as the band labeled γ in figure 7.6 (a). The fact that it is not found in the Ce-terminated data parallels the absence of a Rh derived feature in Ce-terminated ARPES spectra for $CeRh_2Si_2$ [234]. The γ band forms a cone like structure around the $\overline{\Gamma}$ point, at a binding energy of $\sim 0.8\,\mathrm{eV}$. Like the α and β bands, this band is also highly polarization dependent, as it is completely suppressed in the σ channel. It thus has even mirror character along the diagonal. We also stress that this band does not display any significant resonance effects. It does therefore not seem to hybridize with the f electronic states.

7.3 Analysis

7.3.1 Orbital assignments and cf hybridization

We now turn to an analysis of the *cf* hybridization that is dictated by symmetry and the extent of orbital overlap. Generally, the conduction electrons can hybridize with the Ce $f_{5/2}$ states, which due to the crystal electric field (CEF) and spin-orbit coupling (SOC) are split according to figure 7.7 into three levels (see also appendix B):

$$|0\pm\rangle = a\,|J_z = \pm 5/2\rangle + b\,|J_z = \mp 3/2\rangle \quad , \tag{7.1}$$

$$|1\pm\rangle = |J_z = \pm 1/2\rangle \quad , \tag{7.2}$$

$$|2\pm\rangle = a\,|J_z = \mp 3/2\rangle - b\,|J_z = \pm 5/2\rangle \quad , \tag{7.3}$$

with $a^2 + b^2 = 1$. We will sometimes drop the $\pm$ signs for simplicity of notation. From XAS we know that $a = 0.8$ and 0.6 for $CeRu_2Si_2$ [226]. A similar mixing ratio is observed for $CeRh_2Si_2$, hence some generality across the Ce-122 family is expected.

We have seen that the conduction bands display strong light polarization dependence, and thus have significant even and odd orbital character with respect to the photoemission mirror plane. Si *p* orbitals do not have the required symmetry to show this behaviour. In what follows, we therefore assume the band structure to stem predominately from Ru *d* orbitals. We shortly repeat the discussion of the mirror eigenvalues of *d* orbitals that we have seen in table 5.4 of chapter 5. The e_g states $d_{x^2-y^2}$ and $d_{3z^2-r^2}$ have, respectively, odd and even mirror symmetry with respect to the diagonal. Meanwhile, in the t_{2g} sector, d_{xy} is even whereas d_{xz} and d_{yz} do not display a well defined character. However, the linear combination $d_{xz} + d_{yz}$ is even while $d_{xz} - d_{yz}$ is odd.

In order to get a measure for the *cf* hybridization strength, we have to consider the $\langle d|0\rangle$ and $\langle d|2\rangle$ overlaps. We have calculated these terms and the values of their norms are summarized in table 7.1. A complete tabulation of results can be found in tables B.1 to B.5 of

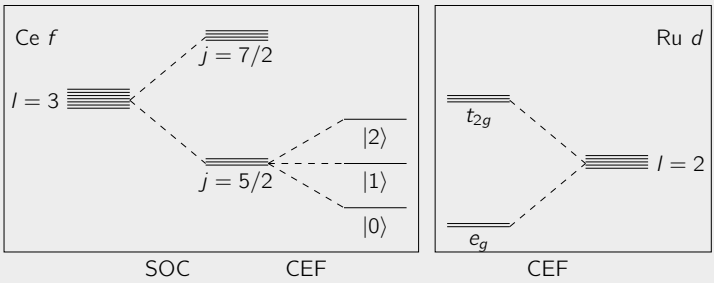

Figure 7.7: Schematic of involved f and d energy levels on the Ce and Ru sites. The fourteen-fold degenerate Ce $4f$ levels are separated into two sets of six ($4f_{5/2}$) and eight ($4f_{7/2}$) levels through SOC. These states are further split through the tetragonal CEF. For the $4f_{5/2}$ states, this results in the $|0\rangle$, $|1\rangle$ and $|2\rangle$ states. The ten-fold degenerate Ru $3d$ orbitals are split under the influence of the tetragonal CEF in the well known fashion into t_{2g} and e_g states.

appendix B. Strikingly, the only d state that shows no overlap with the f derived states is the d_{xy} orbital. We can therefore clearly assign the non-hybridizing, even γ band to d_{xy}.

The effect of the tetrahedral CEF on the Ru atoms leads to a level splitting of the d states into e_g ($d_{x^2-y^2}$ and $d_{3z^2-r^2}$) and t_{2g} (d_{xy}, d_{xz}, d_{yz}) states. In contrast to the case of an octahedral CEF encountered in the cuprates (see chapter 5, figure 5.13), here the e_g states end up at lower energy than the t_{2g} levels. The situation is depicted in figure 7.7. The Ru atoms are found at a mixed valence of Ru^{2+} and Ru^{3+}, which corresponds to a $4d^6$ or $4d^5$ electronic configuration respectively. Combining these two facts, we realize that the four (accounting for spin) e_g states have to be completely occupied and the t_{2g} sector partially filled. We can therefore complete the assignment of orbital character by identifying the even α with $d_{3z^2-r^2}$ and the odd

Table 7.1: Norms of overlap integrals $|\langle d|f\rangle|$ in units of the coupling parameter $t_{df\sigma}$ for $k_z = \pi/c'$. Confer appendix B for the full results.

	$\|0\pm\rangle$	$\|2\pm\rangle$
$\langle x^2 - y^2\|$	0.67	0.37
$\langle z^2\|$	0.4	0.2
$\langle xy\|$	0	0
$\langle xz + yz\|$	0.84	0.073
$\langle xz - yz, \uparrow_\downarrow\|$	2.7	3.0
$\langle xz - yz, \downarrow_\uparrow\|$	0.84	0.073

β with $d_{x^2-y^2}$.

7.3.2 Flower-shaped Fermi surface structure

The calculations of the orbital overlaps $\langle d|0\pm\rangle$ and $\langle d|1\pm\rangle$ reveal sinusoidal k dependencies for the $d_{x^2-y^2}$ and $d_{3z^2-r^2}$ orbitals (confer tables B.1 and B.2). The fact that the hybridization strength varies as a function of the parallel **k** components provides an explanation for the origin of the flower shaped structures at the $\overline{\mathrm{M}}$ point of the in-plane Fermi surface (as highlighted in figure 7.5 and enlarged in figure 7.8): Stronger hybridization leads to stronger bending of the bands which in turn shifts k_F to different values.

$CeCu_2Si_2$ shows a temperature dependence for the relative occupations of the f derived $|0\pm\rangle$ and $|2\pm\rangle$: While the occupation at base temperature lies almost completely on the side of $|0\pm\rangle$, the situation changes when heating above 25 K, whereafter $|0\pm\rangle$ remains almost completely unoccupied in favour of $|2\pm\rangle$ [236]. Given that the Ce atoms live in a comparable environment in $CeRu_2Si_2$, it is reasonable to expect this temperature dependent occupation to hold here as well.

The hybridization calculation results reveal a reduction of hybridiza-

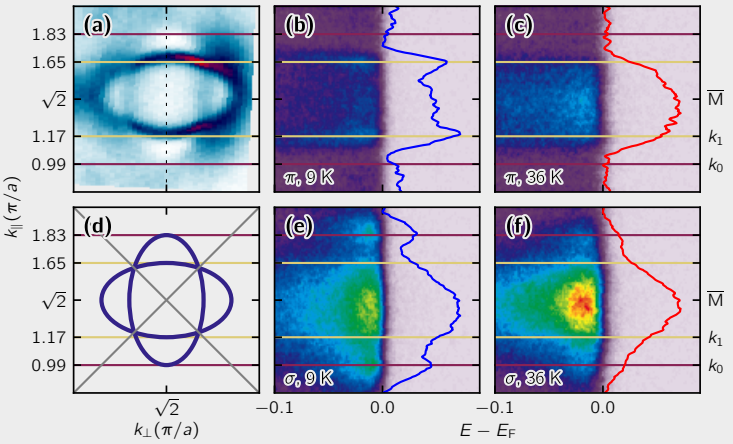

Figure 7.8: Evolution of the flower-shaped FS structure with temperature. **(a)** Zoom of the FSM shown in figure 7.5 (d) around $\overline{\mathrm{M}}$. **(d)** Schematic of the data in (a). **(b)**, **(c)**, **(e)**, **(f)** Low and high temperature energy distribution maps (EDMs) for different polarizations as indicated. The cuts are along the vertical dashed line in (a). Lines above spectra represent normalized MDCs integrated by ±10 meV around E_F. Horizontal lines in all panels serve as guides to the eye to point out how different features in the FSM and MDCs are related. Colorscales as in figures 7.5 and 7.6.

tion strength by roughly 50 % for $\langle d|2\rangle$ compared to $\langle d|0\rangle$ for the $d_{x^2-y^2}$ and $d_{3z^2-r^2}$ orbitals (see table 7.1). With the change in occupation of $|0\rangle$ and $|2\rangle$ when we heat from zero to above 25 K, this would imply that the overall amount of cf hybridization should decrease. To put it simply: Below 25 K we have a predominant occupation of $|0\rangle$ which hybridizes strongly with the conduction electrons. Above 25 K, the majority of this hybridization pathway is lost as the occupation of $|0\rangle$ is reduced in favor of $|2\rangle$. The newly opened pathway of hybridizing with $|2\rangle$ is only about 50 % as efficient. Consequently, the intensity

of the *flower shape* should decrease when heating from below 20 K to above it. This is indeed exactly what we observe: As shown in figure 7.8 the intensities at the respective k_Fs are reduced by factors of 0.7 and 0.8 respectively.

If we denote the relative occupations of $|0\rangle$ and $|2\rangle$ by $n_0(T)$ and $n_2(T) = 1 - n_0(T)$, respectively, and their hybridization strengths by t_0 and $t_2 \approx t_0/2$, we can estimate the expected change in hybridization $m(T)$ when going from low temperature T_0 to the higher temperature T_1 as

$$\frac{m(T_1)}{m(T_0)} = \frac{n_0(T_1) \cdot t_0 + [1 - n_0(T_1)] \cdot t_2}{n_0(T_0) \cdot t_0 + [1 - n_0(T_0)] \cdot t_2} \approx \frac{1 + n_0(T_1)}{1 + n_0(T_0)} \quad . \qquad (7.4)$$

Using values for $n_0(T)$ in the order given for $CeCu_2Si_2$ [236], this results in a reduction of hybridization strength by a factor of 0.7, in perfect agreement with the experimentally observed changes in intensity.

7.4 Summary and discussion

State-of-the-art ARPES experiments on the heavy fermion compound $CeRu_2Si_2$ have revealed FS and band structure data of unprecedented quality. This has enabled us to make a series of new observations on the electronic structure of that system.

Firstly, Si and Ce terminated surfaces can be distinguished by the relative strength of the resonant enhancement effect and by the presence or absence of a dispersive Ru d_{xy} derived state at the $\overline{\Gamma}$ point. Secondly, through symmetry and CEF splitting based arguments we were able to identify the orbital characters of the Ru derived conduction bands. The relevant bands stem from the Ru e_g ($d_{x^2-y^2}$ and $d_{3z^2-r^2}$) orbitals.

Armed with this knowledge, we have carried out computations of the orbital overlaps relevant to cf hybridization. The resulting harmonic k dependencies of the hybridization strengths provide an explanation for the formation of the flower-shaped FS structure observed around

the $\overline{\mathrm{M}}$ point. Furthermore, the temperature dependence of the relative occupations between Ce f states allow us to propose a scenario in which this flower shape would disappear with increasing intensity. This latter scenario is directly supported by our experimental observation of decreasing spectral weight with temperature.

The result of a measurable temperature dependence of band features near the Fermi level can be interpreted as a direct observation of the formation (or breaking up) of composite quasiparticles (QPs) upon cooling below (heating above) a temperature $T \approx 25\,\mathrm{K}$. These QPs are composed of mobile Ru d_x or Ru d_z and localized Ce $4f$ electrons, in line with the Kondo picture and the fact that the associated FS change is expected to mostly take place near the zone corner $\overline{\mathrm{M}}$ [228]. From this viewpoint, the observed hybridization is a direct consequence of the cf spin interaction becoming coherent at low enough temperatures (see section 7.1.1).

Here, however, the formation of this composite QP has a directly observalbe consequence on the FS. Spectral weight is transferred from the *bare* conduction bands to larger k_Fs. In other words: the bands are bent outwards, leading to a change in FS size. Due to a k dependence of the different hybridization channels, the band bendings are not isotropic and lead to the formation of a flower structure in the FS.

The symmetry properties of this flower shape, or rather the symmetry of the k dependence of the cf hybridization strengths are of particular interest. The hybridization exhibits nodes along the BZ diagonals — similar to the symmetry of a d-wave SC. Given the vicinity of the unconventional SC $CeCu_2Si_2$ in the JT phase diagram [227], our observation might shed light onto to question of why one of the compounds is a SC while the other is not or onto the nature of the superconductivity in $CeCu_2Si_2$ itself.

Appendix A: Two band tight binding model

The two band tight binding (TB) model employed by Matt *et al.* [76] to describe the observed dispersion of $La_{2-x}Sr_xCuO_4$ (LSCO) is briefly laid out and discussed in the following.

We will use the second quantization basis

$$\begin{pmatrix} c_{\sigma,\mathbf{k},x^2-y^2} \\ c_{\sigma,\mathbf{k},z^2} \end{pmatrix} \tag{A.1}$$

where the operator $c_{\sigma,\mathbf{k},\alpha}$ annihilates an electron with momentum $\mathbf{k}$ and spin σ from an e_g orbital d_i with $i \in \{x^2-y^2, z^2\}$. In this basis, the Hamiltonian of our two band tight binding (TB) model can be compactly written as

$$H_\sigma(\mathbf{k}) = \begin{pmatrix} M_{x^2-y^2}(\mathbf{k}) & M_{\text{mix}}(\mathbf{k}) \\ M_{\text{mix}}(\mathbf{k}) & M_{z^2}(\mathbf{k}) \end{pmatrix} \tag{A.2}$$

where the M_i denote the intra-orbital hopping matrix elements while M_{mix} represents the inter-orbital mixing term between the $d_{x^2-y^2}$ and $d_{3z^2-r^2}$ states. The intra-orbital hopping terms are given as

$$\begin{aligned} M_{x^2-y^2}(\mathbf{k}) =& \mu + 2t_\alpha \left[\cos(k_x a) + \cos(k_y b)\right] \\ &+ \sum_{\kappa=\pm1} 2t'_\alpha \cos(\mathbf{Q}^\kappa \cdot \mathbf{k}) \end{aligned} \tag{A.3}$$

and

$$\begin{aligned} M_{z^2}(\mathbf{k}) =& -\mu + 2t_\beta \left[\cos(k_x a) + \cos(k_y b)\right] \\ &+ \sum_{\kappa=\pm1} 2t'_\beta \cos(\mathbf{Q}^\kappa \cdot \mathbf{k}) \\ &+ \sum_{\kappa_{1,2}=\pm1} \Big\{ 2t_{\beta z} \cos(\mathbf{R}^{\kappa_1,\kappa_2} \cdot \mathbf{k}) \\ &+ 2t'_{\beta z} \left[\cos(\mathbf{T}_1^{\kappa_1,\kappa_2} \cdot \mathbf{k}) + \cos(\mathbf{T}_2^{\kappa_1,\kappa_2} \cdot \mathbf{k})\right] \Big\} \quad , \end{aligned} \tag{A.4}$$

where the following terms were used for compactness of notation:

$$\mathbf{Q}^{\kappa} = \begin{pmatrix} a \\ \kappa b \\ 0 \end{pmatrix} \quad , \qquad \mathbf{R}^{\kappa_1,\kappa_2} = \frac{1}{2} \begin{pmatrix} \kappa_1 a \\ \kappa_1\kappa_2 b \\ c \end{pmatrix} \quad , \tag{A.5}$$

$$\mathbf{T}_1^{\kappa_1,\kappa_2} = \frac{1}{2} \begin{pmatrix} 3\kappa_1 a \\ \kappa_1\kappa_2 b \\ c \end{pmatrix} \quad , \qquad \mathbf{T}_2^{\kappa_1,\kappa_2} = \frac{1}{2} \begin{pmatrix} \kappa_1 a \\ 3\kappa_1\kappa_2 b \\ c \end{pmatrix} \quad . \tag{A.6}$$

The inter-orbital mixing term, meanwhile, is given by:

$$M_{\text{mix}}(\mathbf{k}) = 2t_{\alpha\beta}\left[\cos(k_x a) - \cos(k_y b)\right] \quad . \tag{A.7}$$

In equations (A.3) to (A.7), μ denotes the chemical potential and t_α and t'_α characterize the nearest neighbor (NN) and next nearest neighbor (NNN) intra-orbital in-plane hopping strengths between $d_{x^2-y^2}$ orbitals. Similarly, t_β and t'_β are the NN and NNN in-plane hopping strengths between $d_{3z^2-r^2}$ orbitals while $t_{\beta z}$ and $t'_{\beta z}$ refer to NN and NNN out-of-plane hopping between $d_{3z^2-r^2}$ orbitals. Finally, the hopping parameter $t_{\alpha\beta}$ characterizes inter-orbital in-plane hopping between $d_{x^2-y^2}$ and $d_{3z^2-r^2}$ orbitals and a and c are the in- and out-of-plane lattice parameters, respectively.

Through diagonalization of the Hamiltonian in equation (A.2) we find two bands:

$$\begin{aligned} \varepsilon_{\pm}(\mathbf{k}) = & \frac{1}{2}\left[M_{x^2-y^2}(\mathbf{k}) + M_{z^2}(\mathbf{k})\right] \\ & \pm \sqrt{\left[M_{x^2-y^2}(\mathbf{k}) - M_{z^2}(\mathbf{k})\right]^2 + 4M_{\text{mix}}(\mathbf{k})^2} \quad . \end{aligned} \tag{A.8}$$

It is interesting to note that along the nodal lines, where $k_x = \pm k_y$, $M_{\text{mix}}(\mathbf{k})$ vanishes and the two bands along these lines are just:

$$\varepsilon_+(\mathbf{k}) = M_{x^2-y^2}(\mathbf{k}) \quad \text{and} \quad \varepsilon_-(\mathbf{k}) = M_{z^2}(\mathbf{k}) \quad , \tag{A.9}$$

i.e. without any mixing between the two. It should be pointed out that the absence of mixing along the nodal line is not an artifact of the finite

range of hopping processes in the model but rather a consequence of opposite mirror eigenvalues for the two orbitals along this line.

Appendix B: cf hybridization calculation results

Here we review and present the corner points of our calculations of the hybridization between $4f^1$ electrons and d electronic states. The results are given in several tables.

We have seen that the $4f^1_{5/2}$ states split into the $|0\rangle$, $|1\rangle$ and $|2\rangle$ states according to equations (7.1) to (7.3). These can also be written in L_z-basis $|L_z, S_z\rangle$ as

$$
\begin{aligned}
|0+\rangle &= a\left[\sqrt{\frac{1}{7}}\,|2,\uparrow\rangle - \sqrt{\frac{6}{7}}\,|3,\downarrow\rangle\right] + b\left[\sqrt{\frac{5}{7}}\,|-2,\uparrow\rangle - \sqrt{\frac{2}{7}}\,|-1,\downarrow\rangle\right] ,\\
|0-\rangle &= a\left[\sqrt{\frac{6}{7}}\,|-3,\uparrow\rangle - \sqrt{\frac{1}{7}}\,|-2,\downarrow\rangle\right] + b\left[\sqrt{\frac{2}{7}}\,|1,\uparrow\rangle - \sqrt{\frac{5}{7}}\,|2,\downarrow\rangle\right] ,\\
|1+\rangle &= a\left[\sqrt{\frac{1}{7}}\,|2,\uparrow\rangle - \sqrt{\frac{6}{7}}\,|3,\downarrow\rangle\right] - b\left[\sqrt{\frac{5}{7}}\,|-2,\uparrow\rangle - \sqrt{\frac{2}{7}}\,|-1,\downarrow\rangle\right] ,\\
|1-\rangle &= a\left[\sqrt{\frac{6}{7}}\,|-3,\uparrow\rangle - \sqrt{\frac{1}{7}}\,|-2,\downarrow\rangle\right] - b\left[\sqrt{\frac{2}{7}}\,|1,\uparrow\rangle - \sqrt{\frac{5}{7}}\,|2,\downarrow\rangle\right] .
\end{aligned}
\tag{B.1}
$$

Here the $\uparrow$ and $\downarrow$ symbols denote a pseudo spin for distinguishing the Kramers-doublets. With that, the calculation of the hybridization strength comes down to a calculation of the orbital overlaps $\langle d|L_z\rangle$.

The results will generally have some k_z dependence. The following tables therefore present the different results for specific cases of $k_z = 0$ and $k_z = \pi/c'$ with the values for $CeRu_2Si_2$ of $a = 0.8$ and $b = 0.6$ [226] plugged in. Absolute strengths are subject to the unknown coupling parameter $t_{df\sigma}$.

Table B.1: Orbital overlap $\langle d_{x^2-y^2}|f\rangle$.

$\lvert f\rangle$	$k_z = 0$	$k_z = \pi/c'$
$\lvert 0\pm\rangle$	$\mp 0.41\left(\sin\frac{k_y}{2} \mp i\sin\frac{k_x}{2}\right) t_{df\sigma}$	$\pm 0.67i\left(\cos\frac{k_y}{2} + \cos\frac{k_x}{2}\right) t_{df\sigma}$
$\lvert 2\pm\rangle$	$\pm 0.036\left(\sin\frac{k_y}{2} \pm i\sin\frac{k_x}{2}\right) t_{df\sigma}$	$\mp 0.37i\left(\cos\frac{k_y}{2} + \cos\frac{k_x}{2}\right) t_{df\sigma}$

Table B.2: Orbital overlap $\langle d_{3z^2-r^2}|f\rangle$.

$\|f\rangle$	$k_z = 0$	$k_z = \pi/c'$
$\|0\pm\rangle$	$\pm 0.2\left(\sin\frac{k_y}{2} \pm i\sin\frac{k_x}{2}\right) t_{df\sigma}$	$\pm 0.4i\left(\cos\frac{k_y}{2} - \cos\frac{k_x}{2}\right) t_{df\sigma}$
$\|2\pm\rangle$	$\pm 0.044\left(\sin\frac{k_y}{2} \pm i\sin\frac{k_x}{2}\right) t_{df\sigma}$	$\mp 0.2i\left(\cos\frac{k_y}{2} - \cos\frac{k_x}{2}\right) t_{df\sigma}$

Table B.3: Orbital overlap $\langle d_{xy}|f\rangle$. The hybridization vanishes within σ-coupling.

$\|f\rangle$	$k_z = 0$	$k_z = \pi/c'$
$\|0\pm\rangle$	0	0
$\|2\pm\rangle$	0	0

Table B.4: Orbital overlap $\langle d_{xz} + d_{yz}|f\rangle$. No k_z dependence.

$\|f\rangle$	k_z-independent
$\|0\pm\rangle$	$0.84 \cdot (i \pm 1)\sin\frac{k_y}{2}\cos\frac{k_x}{2}\, t_{df\sigma}$
$\|2\pm\rangle$	$-0.073 \cdot (i \pm 1)\sin\frac{k_y}{2}\cos\frac{k_x}{2}\, t_{df\sigma}$

Table B.5: Orbital overlap $\langle d_{xz} - d_{yz}|f\rangle$ in units of the coupling parameter $t_{df\sigma}$. This overlap shows no k_z dependence. However, there is a difference for the possible spin distributions.

$\|f\rangle$	$\langle d_{xz} - d_{yz}, \uparrow_\downarrow\|$	$\langle d_{xz} - d_{yz}, \downarrow_\uparrow\|$
$\|0\pm\rangle$	$\mp 2.7i\cos\frac{k_y}{2}\sin\frac{k_x}{2}$	$\mp 0.84 \cdot (1 \mp i)\sin\frac{k_y}{2}\cos\frac{k_x}{2}$
$\|2\pm\rangle$	$\pm 3.0i\cos\frac{k_y}{2}\sin\frac{k_x}{2}$	$\pm 0.073 \cdot (1 \mp i)\sin\frac{k_y}{2}\cos\frac{k_x}{2}$

Appendix C: Miscellaneous

The following sections contain short notes and technical details that were left out of the main text for the sake of conciseness.

C.1 Green's functions for interacting electrons

We introduce the second quantization operators

$$\mathbf{\Psi}^{+}(\mathbf{x}) \quad , \quad \mathbf{\Psi}(\mathbf{x}) \quad , \tag{C.1}$$

that when acting upon the N particle system $|N\rangle$, create and destroy a particle at point $\mathbf{x}$. Furthermore, we remember how time evolution of second quantized operators in the *Heisenberg representation* is achieved:

$$\mathbf{O}(t) = e^{i\mathbf{H}t/\hbar}\mathbf{O}(0)e^{-i\mathbf{H}t/\hbar} \quad . \tag{C.2}$$

The Green's function G for a system of N interacting electrons in groundstate $|N\rangle$ with energy E_N^0 describes the time evolution of an extra particle added above or of a hole created below the Fermi level. In terms of the just defined quantities, this is given as

$$G(\mathbf{x}, t; \mathbf{x}', t') = -\frac{i}{\hbar}\left\langle N\right| T\left[\mathbf{\Psi}(\mathbf{x}, t)\mathbf{\Psi}^{+}(\mathbf{x}', t')\right]\left|N\right\rangle \quad , \tag{C.3}$$

where the time-ordering operator T arranges its arguments according to the times, with the earliest time farthest to the right and the latest at the very left. This expression can be interpreted as generating a particle (hole) at coordinate $\mathbf{x}'$ ($\mathbf{x}$) at time t' (t) with the operator furthest to the right and then look at it at the point $\mathbf{x}$ ($\mathbf{x}'$) at the later time t (t'). Writing out the time evolution this reads as

$$G(\mathbf{x}, t; \mathbf{x}', t') = \begin{cases} -i/\hbar\left\langle N\right|\mathbf{\Psi}(\mathbf{x})e^{-i(\mathbf{H}-E_N)(t-t')/\hbar}\mathbf{\Psi}^{+}(\mathbf{x}')\left|N\right\rangle & , \quad t' < t \\ i/\hbar\left\langle N\right|\mathbf{\Psi}^{+}(\mathbf{x}')e^{+i(\mathbf{H}-E_N)(t-t')/\hbar}\mathbf{\Psi}(\mathbf{x})\left|N\right\rangle & , \quad t' > t \end{cases} \tag{C.4}$$

where the minus sign in the $t' > t$ case disappeared due to the anticommutation relation of fermion operators.

We can now introduce complete sets of eigenstates of the $(N+1)$ and $(N-1)$ particle systems,

$$\left\{\left|N \pm 1; s\right\rangle, E_{N\pm1}^{s}, s = 0, 1, \dots\right\} \quad , \tag{C.5}$$

and define the *quasiparticle amplitudes* f_s

$$f_s(\mathbf{x}) = \begin{cases} \langle N| \, \mathbf{\Psi}(\mathbf{x}) \, |N+1; s\rangle & , \quad \varepsilon_s > E_\mathrm{F} \\ \\ \langle N-1| \, \mathbf{\Psi}(\mathbf{x}) \, |N; s\rangle & , \quad \varepsilon_s < E_\mathrm{F} \end{cases} \tag{C.6}$$

and the quasiparticle or excitation energies ε_s as

$$\varepsilon_s = \begin{cases} E^s_{N+1} - E^0_N & , \quad \varepsilon_s > E_\mathrm{F} \\ E^0_N - E^s_{N-1} & , \quad \varepsilon_s < E_\mathrm{F} \end{cases} \quad . \tag{C.7}$$

These allow us to write the Green's function in a more compact form ($\tau = t - t'$):

$$\begin{aligned} G(\mathbf{x}; \mathbf{x}'; \tau) = &- \frac{i}{\hbar} \sum_s f_s(\mathbf{x}) f_s^*(\mathbf{x}') e^{-i\varepsilon_s \tau/\hbar} \\ &\cdot [\theta(\tau)\theta(\varepsilon_s - E_\mathrm{F}) - \theta(-\tau)\theta(E_\mathrm{F} - \varepsilon_s)] \quad , \end{aligned} \tag{C.8}$$

with

$$\theta(x) = \begin{cases} 1 & \text{if } x \geq 0 \\ 0 & \text{if } x < 0 \end{cases} \quad . \tag{C.9}$$

Finally, we take the Fourier transform of equation (C.8) to find an expression in energy space:

$$\begin{aligned} G(\mathbf{x}; \mathbf{x}'; E) = &\int_{-\infty}^{\infty} G(\mathbf{x}; \mathbf{x}'; \tau) e^{iE\tau/\hbar} \mathrm{d}\tau \\ = &\frac{i}{\hbar} \sum_s f_s(\mathbf{x}) f_s^*(\mathbf{x}') \\ &\cdot \left[-\theta(\varepsilon_s - E_\mathrm{F}) \int_0^{\infty} e^{i(E-\varepsilon_s)\tau/\hbar} \mathrm{d}\tau \right. \\ &\left. + \theta(E_\mathrm{F} - \varepsilon_s) \int_{-\infty}^{0} e^{i(E-\varepsilon_s)\tau/\hbar} \mathrm{d}\tau \right] \end{aligned} \quad . \tag{C.10}$$

The integrals are undefined for $\tau \to \pm\infty$ but can be brought to convergence by introducing a complex positive infinitesimal $i\Delta$ and substituting as follows:

$$\varepsilon_s \to \begin{cases} \varepsilon_s + i\Delta & \text{for } \varepsilon_s < E_\mathrm{F} \\ \varepsilon_s - i\Delta & \text{for } \varepsilon_s > E_\mathrm{F} \end{cases} \quad . \tag{C.11}$$

Which leads to the converged result presented in equation (3.6):

$$G(\mathbf{x}, \mathbf{x}'; E) = \sum_s \frac{f_s(\mathbf{x}) f_s^*(\mathbf{x}')}{E - \varepsilon_s + i\Delta\,\mathrm{sgn}(\varepsilon_s - E_\mathrm{F})} \quad . \tag{C.12}$$

The quasiparticle amplitudes $f_s(\mathbf{x})$ are matrix elements of field operators between many body states [equation (C.6)] and the factor $\mathrm{sgn}(\varepsilon_s - E_\mathrm{F})$ reflects the fact that we are in the presence of a filled Fermi sea.

C.2 Application of rotation matrices

Equation (C.13) shows how we apply rotation matrices to move from the lab- to the sample frame for the conversion from photoemission angle to crystal momentum, as described in section 4.1.1.

$$
\begin{aligned}
\mathbf{k}_1^{\text{sample}} =& [R_x(\alpha)R_y(\beta)]^{-1}\mathbf{k}_1^{\text{lab}} = R_y^{-1}(\beta)R_x^{-1}(\alpha)\mathbf{k}_1^{\text{lab}} \\
=& k_1 R_y^{-1}(\beta) \begin{pmatrix} 1 & 0 & 0 \\ 0 & \cos\alpha & \sin\alpha \\ 0 & -\sin\alpha & \cos\alpha \end{pmatrix} \begin{pmatrix} \sin\theta_k \sin\gamma_0 \\ \sin\theta_k \cos\gamma_0 \\ \cos\theta_k \end{pmatrix} \\
=& k_1 \begin{pmatrix} \cos\beta & 0 & \sin\beta \\ 0 & 1 & 0 \\ -\sin\beta & 0 & \cos\beta \end{pmatrix} \cdot \\
& \begin{pmatrix} \sin\theta_k \sin\gamma_0 \\ \sin\theta_k \cos\alpha \cos\gamma_0 + \cos\theta_k \sin\alpha \\ -\sin\theta_k \sin\alpha \cos\gamma_0 + \cos\theta_k \cos\alpha \end{pmatrix} \quad .
\end{aligned} \tag{C.13}
$$

C.3 Spectral function construction for 2D fitting

In the following we shortly review the construction of the full spectral function as proposed in [88]. The interested reader is referred in particular to the supplementary material of that reference. The core for their construction is the imaginary part of the self-energy $\operatorname{Im}\Sigma$. From it, the real part is found by means of the Kramers-Kronig relations. The goal is then to construct the spectral function as the imaginary part of the Nambu-Gorkov form of the Green's function G_{11}:

$$
G_{11}(\mathbf{k}, E) = \frac{E - \Sigma(E) + E_{\text{bare}}(\mathbf{k})}{[E - \Sigma(E)]^2 - E_{\text{bare}}(\mathbf{k})^2 - [Z(E)\Delta(\mathbf{k})]^2} \quad . \tag{C.14}
$$

$E_{\text{bare}} = \hbar^2\mathbf{k}^2/(2m^*)$ describes a bare band dispersion with effective mass m^* (here taken to be constant that allows for differently dispersing bare bands). $Z(E)$ is the dynamical renormalization factor that can be found from $\operatorname{Re}\Sigma$ and $\Delta(\mathbf{k})$ is the superconducting pairing gap.

The proposed model for $\mathrm{Im}\,\Sigma$ is essentially that of a marginal Fermi liquid. It is extended by extra terms that empirically improve the fitting convergence. Of course, different forms are imaginable and Li *et al.* have experimented and compared a number of reasonable functional forms in order to verify that the exact choice of terms does not affect the converged results significantly. The form used here in the creation of figure 4.7 is:

$$\begin{aligned}\mathrm{Im}\,\Sigma(E) =& \lambda\sqrt{E^2 + (\pi k_\mathrm{B} T)^2} + I_0 \\ &+ I_1 \left[\exp\left(\frac{E - E_1}{W_1} + 1\right)\right]^{-1} \\ &+ I_2 \exp\left(\frac{(E - E_2)^2}{2W_2^2}\right) \quad ,\end{aligned} \tag{C.15}$$

i.e. the additional terms are a Gaussian step at E_1 and a Gaussian bell curve centered at E_2. The eight fit parameters for this function are the weights λ, I_0, I_1 and I_2, the feature positions E_1 and E_2 and their widths W_1 and W_2. Together with the parameters from the bare band (band bottom E_bottom and m^*), the superconducting gap Δ (taken to be **k**-independent) and two terms for energy and momentum broadening (instrumental resolution) this amounts to a total of 13 parameters. The values used in the creation of figure 4.7 are listed in table C.1.

Table C.1: Parameters used in figure 4.7.

parameter	λ	Δ	m^*	E_bottom	I_0	
unit	1	eV	m_e	eV	eV	
value	0.08	0.01	1	-0.96	0	
parameter	I_1	E_1	W_1	I_2	E_2	W_2
unit	1	eV	eV	1	eV	eV
value	-0.04	-0.3	0.01	0.02	-0.9	0.5

C.4 Tabulated values for figure 6.6

Table C.2: Data shown in the spectroscopic Kadowaki-Woods plot (figure 6.6). Bare band widths $4W$ from density functional theory (DFT) calculations together with the experimentally extracted values of β and ω_c for the materials as indicated.

	LSCO ($x = 0.23$)	CSRO	$LaNiO_3$	PLCCO ($x = 0.15$)
$4W$ (eV)	3.44 [198]	1.44 [200]	3.10 [199]	3.28 [185]
β (eV^{-1})	8.60 [147][a]	17.9 [4]	4.65 [197]	2.25 [4]
ω_c (meV)	180 [147][a]	93 [4]	270 [197]	400 [4]

[a] Measured at the node.

C.5 Visualizations of f orbitals

While real space representations of the *d* orbitals are frequently found in high school textbooks, the slightly more complicated *f* orbitals are shown less often. Figure C.1 shows isosurfaces in three dimensional (3D) real space that correspond to the *real f* orbitals, as indicated. The isosurfaces are drawn such that they enclose a volume wherein one has a 90 % probability of finding the respective *f* electron. The color of the surfaces represents the complex phase of the wave function. Since in the real representation, the orbital wave functions do not have an imaginary part, the phase is identical to the sign in this case.

The same kind of representation is used for the spin-orbit coupling (SOC) and crystal electric field (CEF) split $|0\pm\rangle$ and $|2\pm\rangle$ states in figure C.2. As these states ultimately are superpositions of the *complex* spherical harmonics, they do not show a clean separation into *positive* and *negative* lobes.

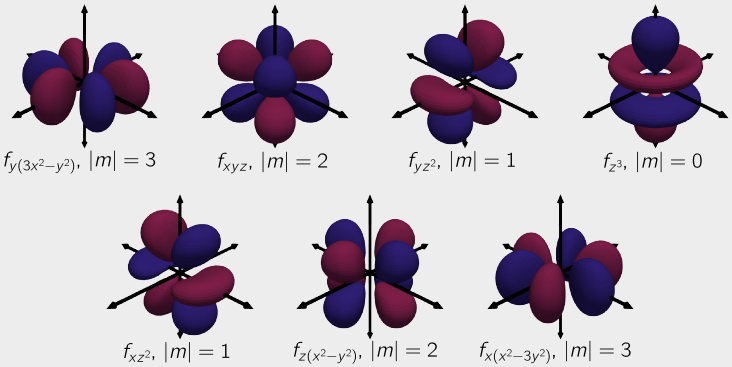

Figure C.1: Depiction of the f orbitals labeled by their corresponding values of m.

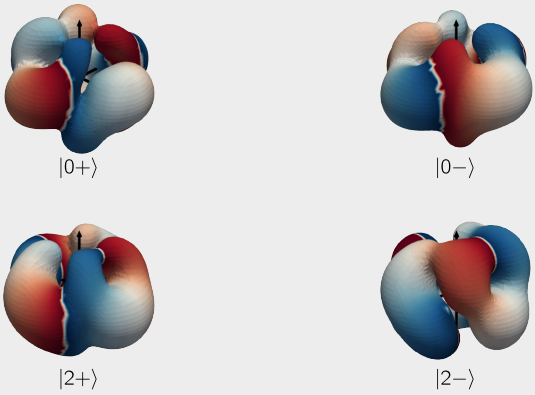

Figure C.2: Real space representation of a subset of the SOC and CEF split f orbitals. These orbitals are defined in equations (7.1) and (7.3). Colour indicates the complex phase.

Bibliography

[1] M. Horio et al. "Two-Dimensional Type-II Dirac Fermions in Layered Oxides". In: *Nat Commun* 9.1 (Aug. 14, 2018), pp. 1–7. ISSN: 2041-1723. DOI: 10.1038/s41467-018-05715-2. URL: https://www.nature.com/articles/s41467-018-05715-2 (visited on 01/13/2020) (cit. on pp. I, 87, 102, 106, 107, 109, 124).

[2] M. Horio et al. "Three-Dimensional Fermi Surface of Overdoped La-Based Cuprates". In: *Phys. Rev. Lett.* 121.7 (Aug. 17, 2018), p. 077004. DOI: 10.1103/PhysRevLett.121.077004. URL: https://link.aps.org/doi/10.1103/PhysRevLett.121.077004 (visited on 01/13/2020) (cit. on pp. I, 102, 106, 113, 135).

[3] K. P. Kramer et al. "Band Structure of Overdoped Cuprate Superconductors: Density Functional Theory Matching Experiments". In: *Phys. Rev. B* 99.22 (June 17, 2019), p. 224509. DOI: 10.1103/PhysRevB.99.224509. URL: https://link.aps.org/doi/10.1103/PhysRevB.99.224509 (visited on 06/18/2019) (cit. on pp. I, 102, 106, 140).

[4] M. Horio et al. "Oxide Fermi Liquid Universality Revealed by Electron Spectroscopy". In: *Phys. Rev. B* 102.24 (Dec. 31, 2020), p. 245153. DOI: 10.1103/PhysRevB.102.245153. URL: https://link.aps.org/doi/10.1103/PhysRevB.102.245153 (visited on 01/20/2021) (cit. on pp. I, 132, 179).

[5] Kevin Kramer and Johan Chang. "Visualization of Multi-Dimensional Data – The Data-Slicer Package". In: *Journal of Open Source Software* 6.60 (Apr. 16, 2021), p. 2969. ISSN: 2475-9066. DOI: 10.21105/joss.02969. URL: https://joss.theoj.org/papers/10.21105/joss.02969 (visited on 04/19/2021) (cit. on pp. I, 74, 96, 97, 154).

[6] M. Horio et al. "Electronic Reconstruction Forming a C 2 -Symmetric Dirac Semimetal in Ca 3 Ru 2 O 7". In: *npj Quantum Materials* 6.1 (1 Mar. 19, 2021), pp. 1–7. ISSN: 2397-4648. DOI: 10.1038/s41535-021-00328-3. URL: https://www.nature.com/articles/s41535-021-00328-3 (visited on 05/21/2021) (cit. on p. I).

[7] Yuval Noah Harari. *Sapiens: A Brief History of Humankind*. Israel: Dvir Publishing House, 2011. ISBN: 978-0-06-231609-7. URL: https://en.wikipedia.org/wiki/Sapiens:_A_Brief_History_of_Humankind (cit. on p. 23).

[8] *The Nobel Prize in Physics 2011*. NobelPrize.org. URL: https://www.nobelprize.org/prizes/physics/2011/schmidt/facts/ (visited on 09/23/2021) (cit. on p. 25).

[9] *Challenges at the Frontiers of Matter and Energy: Transformative Opportunities for Discovery Science*. U.S. Department of Energy, 2015. URL: https://science.osti.gov/-/media/bes/besac/pdf/Reports/Challenges_at_the_Frontiers_of_Matter_and_Energy_rpt.pdf?la=en&hash=93DADAB468987BB52900D3EA96F5021EE03ED66A (cit. on p. 26).

[10] Hsinhan Tsai et al. "Light-Induced Lattice Expansion Leads to High-Efficiency Perovskite Solar Cells". In: *Science* 360.6384 (2018), pp. 67–70. ISSN: 0036-8075. DOI: 10.1126/science.aap8671. eprint: https://science.sciencemag.org/content/360/6384/67.full.pdf. URL: https://science.sciencemag.org/content/360/6384/67 (cit. on p. 26).

[11] Denis Sheptyakov et al. "Stroboscopic Neutron Diffraction Applied to Fast Time-Resolved Operando Studies on Li-Ion Batteries (d-LiNi0.5Mn1.5O4vs. Graphite)". In: *J. Mater. Chem. A* 8.3 (2020), pp. 1288–1297. DOI: 10.1039/C9TA11826H. URL: http://dx.doi.org/10.1039/C9TA11826H (cit. on p. 26).

[12] Valeska P. Ting et al. "Direct Evidence for Solid-like Hydrogen in a Nanoporous Carbon Hydrogen Storage Material at Supercritical Temperatures". In: *ACS Nano* 9.8 (2015), pp. 8249–8254. DOI: 10.1021/acsnano.5b02623. eprint: https://doi.org/10.1021/acsnano.5b02623. URL: https://doi.org/10.1021/acsnano.5b02623 (cit. on p. 26).

[13] *The Nobel Prize in Physics 1913*. NobelPrize.org. URL: https://www.nobelprize.org/prizes/physics/1913/onnes/facts/ (visited on 09/20/2021) (cit. on p. 27).

[14] Michel Van Camp et al. "Geophysics From Terrestrial Time-Variable Gravity Measurements". In: *Reviews of Geophysics* 55.4 (2017), pp. 938–992. ISSN: 1944-9208. DOI: 10.1002/2017RG000566. URL: https://onlinelibrary.wiley.com/doi/abs/10.1002/2017RG000566 (visited on 09/20/2021) (cit. on pp. 27, 30).

[15] W. L. McMillan. "Transition Temperature of Strong-Coupled Superconductors". In: *Phys. Rev.* 167.2 (Mar. 10, 1968), pp. 331–344. DOI: 10.1103/PhysRev.167.331. URL: https://link.aps.org/doi/10.1103/PhysRev.167.331 (visited on 09/20/2021) (cit. on p. 28).

[16] N. W. Ashcroft. "Metallic Hydrogen: A High-Temperature Superconductor?" In: *Phys. Rev. Lett.* 21.26 (Dec. 23, 1968), pp. 1748–1749. DOI: 10.1103/PhysRevLett.21.1748. URL: https://link.aps.org/doi/10.1103/PhysRevLett.21.1748 (visited on 09/20/2021) (cit. on p. 28).

[17] A. P. Drozdov et al. "Conventional Superconductivity at 203 Kelvin at High Pressures in the Sulfur Hydride System". In: *Nature* 525.7567 (7567 Sept. 2015), pp. 73–76. ISSN: 1476-4687. DOI: 10.1038/nature14964. URL: https://www.nature.com/articles/nature14964 (visited on 09/20/2021) (cit. on p. 28).

[18] J. G. Bednorz and K. A. Müller. "Possible highTc Superconductivity in the Ba-La-Cu-O System". In: *Z. Physik B - Condensed Matter* 64.2 (June 1, 1986), pp. 189–193. ISSN: 1431-584X. DOI: 10.1007/BF01303701. URL: https://doi.org/10.1007/BF01303701 (visited on 01/21/2019) (cit. on pp. 28, 103).

[19] A. Schilling et al. "Superconductivity above 130 K in the Hg–Ba–Ca–Cu–O System". In: *Nature* 363.6424 (6424 May 1993), pp. 56–58. ISSN: 1476-4687. DOI: 10.1038/363056a0. URL: https://www.nature.com/articles/363056a0 (visited on 09/25/2021) (cit. on p. 28).

[20] Pia Jensen Ray. "Structural Investigation of La2–xSrxCuO4+y - Following Staging as a Function of Temperature". MA thesis. Copenhagen, Denmark: University of Copenhagen, Nov. 2015. URL: DOI:10.6084/m9.figshare.2075680.v2 (cit. on p. 29).

[21] *Creative Commons — Attribution-ShareAlike 4.0 International*. Version 4.0. URL: https://creativecommons.org/licenses/by-sa/4.0/deed.en (visited on 04/28/2021) (cit. on pp. 29, 46).

[22] *Magnets*. ITER. URL: http://www.iter.org/mach/magnets (visited on 09/22/2021) (cit. on p. 30).

[23] Md. Rabiul Islam, Youguang Guo, and Jianguo Zhu. "A Review of Offshore Wind Turbine Nacelle: Technical Challenges, and Research and Developmental Trends". In: *Renewable and Sustainable Energy Reviews* 33 (May 1, 2014), pp. 161–176. ISSN: 1364-0321. DOI: 10.1016/j.rser.2014.01.085. URL: https://www.sciencedirect.com/science/article/pii/S1364032114001087 (visited on 09/22/2021) (cit. on p. 30).

[24] Philip Varghese and Kwa-Sur Tam. "Structures for Superconductive Magnetic Energy Storage". In: *Energy* 15.10 (Oct. 1, 1990), pp. 873–884. ISSN: 0360-5442. DOI: 10.1016/0360-5442(90)90069-E. URL: https://www.sciencedirect.com/science/article/pii/036054429090069E (visited on 06/25/2021) (cit. on p. 30).

[25] *Chūō Shinkansen*. In: *Wikipedia*. Sept. 28, 2021. URL: https://en.wikipedia.org/w/index.php?title=Ch%C5%AB%C5%8D_Shinkansen&oldid=1046952044 (visited on 10/04/2021) (cit. on p. 31).

[26] P. W. Anderson. "More Is Different". In: *Science* 177.4047 (Aug. 4, 1972), pp. 393–396. ISSN: 0036-8075, 1095-9203. DOI: 10.1126/science.177.4047.393. pmid: 17796623. URL: https://science.sciencemag.org/content/177/4047/393 (visited on 06/05/2021) (cit. on pp. 31, 32).

[27] Yi Zhang et al. "Machine Learning in Electronic-Quantum-Matter Imaging Experiments". In: *Nature* 570.7762 (7762 June 2019), pp. 484–490. ISSN: 1476-4687. DOI: 10.1038/s41586-019-1319-8. URL: https://www.nature.com/articles/s41586-019-1319-8 (visited on 11/25/2020) (cit. on pp. 33, 94, 95).

[28] *Deciphering Life's Enigma Code. NobelPrize.Org. Nobel Media AB 2021. Mon. 18 Jan 2021.* URL: https://www.nobelprize.org/prizes/medicine/1962/speedread/ (cit. on p. 33).

[29] *The Nobel Prize in Physics 1970. NobelPrize.Org. Nobel Media AB 2021. Sun. 17 Jan 2021.* URL: https://www.nobelprize.org/prizes/physics/1970/summary/ (cit. on p. 33).

[30] J. Osterwalder. "Fermi Surface Mapping by Photoemission". In: *Surf. Rev. Lett.* 04.02 (Apr. 1, 1997), pp. 391–408. ISSN: 0218-625X. DOI: 10.1142/S0218625X97000390. URL: https://www.worldscientific.com/doi/abs/10.1142/S0218625X97000390 (visited on 08/19/2021) (cit. on p. 33).

[31] Andrea Damascelli. "Probing the Electronic Structure of Complex Systems by ARPES". In: *Phys. Scr.* 2004.T109 (Jan. 1, 2004), p. 61. ISSN: 1402-4896. DOI: 10.1238/Physica.Topical.109a00061. URL: https://iopscience.iop.org/article/10.1238/Physica.Topical.109a00061/meta (visited on 09/22/2021) (cit. on p. 33).

[32] B. O. Wells et al. "Evidence for K-Dependent, in-Plane Anisotropy of the Superconducting Gap in $Bi_2Sr_2CaCu_2O_{8+ffi}$". In: *Phys. Rev. B* 46.18 (Nov. 1, 1992), pp. 11830–11834. DOI: 10.1103/PhysRevB.46.11830. URL: https://link.aps.org/doi/10.1103/PhysRevB.46.11830 (visited on 11/25/2020) (cit. on pp. 33, 94, 95).

[33] Z. -X. Shen et al. "Photoemission Studies of High-Tc Superconductors: The Superconducting Gap". In: *Science* 267.5196 (Jan. 20, 1995), pp. 343–350. DOI: 10.1126/science.267.5196.343. URL: https://www.science.org/doi/abs/10.1126/science.267.5196.343 (visited on 09/22/2021) (cit. on p. 33).

[34] H. Hertz. "Ueber Einen Einfluss Des Ultravioletten Lichtes Auf Die Electrische Entladung". In: *Annalen der Physik* 267.8 (1887), pp. 983–1000. ISSN: 1521-3889. DOI: 10.1002/andp.18872670827. URL: https://onlinelibrary.wiley.com/doi/abs/10.1002/andp.18872670827 (visited on 04/09/2021) (cit. on p. 36).

[35] Wilhelm Hallwachs. "Ueber Den Einfluss Des Lichtes Auf Electrostatisch Geladene Körper". In: *Annalen der Physik* 269.2 (1888), pp. 301–312. ISSN: 1521-3889. DOI: 10.1002/andp.18882690206. URL: https://onlinelibrary.wiley.com/doi/abs/10.1002/andp.18882690206 (visited on 04/09/2021) (cit. on p. 36).

[36] Max Planck. "Ueber Das Gesetz Der Energieverteilung Im Normalspectrum". In: *Annalen der Physik* 309.3 (1901), pp. 553–563. ISSN: 1521-3889. DOI: 10.1002/andp.19013090310. URL: https://onlinelibrary.wiley.com/doi/abs/10.1002/andp.19013090310 (visited on 04/27/2021) (cit. on p. 36).

[37] A. Einstein. "Über Einen Die Erzeugung Und Verwandlung Des Lichtes Betreffenden Heuristischen Gesichtspunkt". In: *Annalen der Physik* 322.6 (1905), pp. 132–148. ISSN: 1521-3889. DOI: 10.1002/andp.19053220607. URL: https://onlinelibrary.wiley.com/doi/abs/10.1002/andp.19053220607 (visited on 01/21/2019) (cit. on p. 36).

[38] Andrea Damascelli, Zahid Hussain, and Zhi-Xun Shen. "Angle-Resolved Photoemission Studies of the Cuprate Superconductors". In: *Rev. Mod. Phys.* 75.2 (Apr. 17, 2003), pp. 473–541. DOI: 10.1103/RevModPhys.75.473. URL: https://link.aps.org/doi/10.1103/RevModPhys.75.473 (visited on 02/22/2018) (cit. on pp. 36, 47, 90, 92, 105, 118, 119, 122, 133).

[39] Jonathan A. Sobota, Yu He, and Zhi-Xun Shen. "Angle-Resolved Photoemission Studies of Quantum Materials". In: *Rev. Mod. Phys.* 93.2 (May 26, 2021), p. 025006. DOI: 10.1103/RevModPhys.93.025006. URL: https://link.aps.org/doi/10.1103/RevModPhys.93.025006 (visited on 08/19/2021) (cit. on pp. 36, 47, 76).

[40] T. Valla et al. "Evidence for Quantum Critical Behavior in the Optimally Doped Cuprate $Bi_2sr_2CaCu_2o_{8+\delta}$". In: *Science* 285.5436 (1999), pp. 2110–2113. URL: http://www.sciencemag.org/content/285/5436/2110.abstract (cit. on pp. 37, 137).

[41] Mattia Cattelan and Neil A. Fox. "A Perspective on the Application of Spatially Resolved ARPES for 2D Materials". In: *Nanomaterials* 8.5 (5 May 2018), p. 284. DOI: 10.3390/nano8050284. URL: https://www.mdpi.com/2079-4991/8/5/284 (visited on 04/27/2021) (cit. on p. 38).

[42] Xingjiang Zhou et al. "New Developments in Laser-Based Photoemission Spectroscopy and Its Scientific Applications: A Key Issues Review". In: *Rep. Prog. Phys.* 81.6 (Apr. 11, 2018), p. 062101. ISSN: 0034-4885. DOI: 10.1088/1361-6633/aab0cc. URL: https://iopscience.iop.org/article/10.1088/1361-6633/aab0cc/meta (visited on 04/27/2021) (cit. on pp. 38, 39, 47).

[43] S. Hellmann et al. "Time-Resolved x-Ray Photoelectron Spectroscopy at FLASH". In: *New J. Phys.* 14.1 (Jan. 2012), p. 013062. ISSN: 1367-2630. DOI: 10.1088/1367-2630/14/1/013062. URL: https://doi.org/10.1088/1367-2630/14/1/013062 (visited on 05/11/2021) (cit. on p. 39).

[44] Philip. Willmott. "Introduction to Synchrotron Radiation : Techniques and Applications". In: *Introduction to Synchrotron Radiation Techniques and Applications*. Hoboken: Wiley, 2011. ISBN: 1-119-97286-8 (cit. on pp. 41, 42).

[45] P. L. Wincott et al. "Angle-Resolved Photoemission Studies of the \g̅G Shockley Surface State on Ordered Cu(111) Overlayers on TiO2(110)". In: *Surface Science*. European Conference on Surface Science 377–379 (Apr. 20, 1997), pp. 242–246. ISSN: 0039-6028. DOI: 10.1016/S0039-6028(96)01367-2. URL: https://www.sciencedirect.com/science/article/pii/S0039602896013672 (visited on 08/19/2021) (cit. on p. 43).

[46] F. Baumberger, T. Greber, and J. Osterwalder. "Step-Induced One Dimensional Surface State on Cu(332)". In: *Phys. Rev. B* 62.23 (Dec. 15, 2000), pp. 15431–15434. DOI: 10.1103/PhysRevB.62.15431. URL: https://link.aps.org/doi/10.1103/PhysRevB.62.15431 (visited on 08/19/2021) (cit. on p. 43).

[47] Martin Månsson et al. "On-Board Sample Cleaver". In: *Rev. Sci. Instrum.* 78 (2007), p. 076103. DOI: 10.1063/1.2756754 (cit. on pp. 44, 112).

[48] M. P. Seah and W. A. Dench. "Quantitative Electron Spectroscopy of Surfaces: A Standard Data Base for Electron Inelastic Mean Free Paths in Solids". In: *Surface and Interface Analysis* 1.1 (1979), pp. 2–11. ISSN: 1096-9918. DOI: 10.1002/sia.740010103. URL: https://analyticalsciencejournals.onlinelibrary.wiley.com/doi/abs/10.1002/sia.740010103 (visited on 05/21/2021) (cit. on p. 45).

[49] Ponor. *English: Setup of an ARPES Experiment: Light Source Provides Photons That Eject Electrons from the Sample; the Electron Emission Angle and Energy Are Measured by the Hemispherical Electron Analyzer.* June 4, 2020. URL: https://commons.wikimedia.org/wiki/File:ARPES_analyzer_cross_section.svg (visited on 04/28/2021) (cit. on p. 46).

[50] *Electron Analysers - Scienta Omicron*. URL: https://scientaomicron.com/en/components/electron-analysers (visited on 08/19/2021) (cit. on p. 47).

[51] *PHOIBOS 150 — SPECS*. URL: https://www.specs-group.com/nc/specs/productseries/detail/phoibos-150/ (visited on 08/19/2021) (cit. on p. 47).

[52] Masafumi Horio. "Photoemission Studies of New Electron-Doped Cuprate High-Temperature Superconductors". PhD thesis. 2017 (cit. on p. 47).

[53] Denys Sutter. "Strong Electron Correlations in the Ruthenates". PhD thesis. 2019 (cit. on p. 47).

[54] Friedrich Reinert and Stefan Hüfner. "Photoemission Spectroscopy - from Early Days to Recent Applications". In: *New J. Phys.* 7 (Apr. 2005), pp. 97–97. ISSN: 1367-2630. DOI: 10.1088/1367-2630/7/1/097. URL: https://doi.org/10.1088/1367-2630/7/1/097 (visited on 04/09/2021) (cit. on p. 47).

[55] Jonathan A. Sobota, Yu He, and Zhi-Xun Shen. *Electronic Structure of Quantum Materials Studied by Angle-Resolved Photoemission Spectroscopy*. Aug. 5, 2020. arXiv: 2008.02378 [cond-mat]. URL: http://arxiv.org/abs/2008.02378 (visited on 05/07/2021) (cit. on p. 47).

[56] Simon Moser. "An Experimentalist's Guide to the Matrix Element in Angle Resolved Photoemission". In: *Journal of Electron Spectroscopy and Related Phenomena* 214 (Jan. 1, 2017), pp. 29–52. ISSN: 0368-2048. DOI: 10.1016/j.elspec.2016.11.007. URL: http://www.sciencedirect.com/science/article/pii/S0368204816301724 (visited on 07/27/2018) (cit. on pp. 47, 49, 122).

[57] O. Tjernberg et al. "Resonant Photoelectron Spectroscopy on NiO". In: *Phys. Rev. B* 53.15 (Apr. 15, 1996), pp. 10372–10376. DOI: 10.1103/PhysRevB.53.10372. URL: https://link.aps.org/doi/10.1103/PhysRevB.53.10372 (visited on 07/27/2021) (cit. on pp. 52, 54).

[58] Alessandra Vittorini-Orgeas and Antonio Bianconi. "From Majorana Theory of Atomic Autoionization to Feshbach Resonances in High Temperature Superconductors". In: *J Supercond Nov Magn* 22.3 (Apr. 1, 2009), pp. 215–221. ISSN: 1557-1947. DOI: 10.1007/s10948-008-0433-x. URL: https://doi.org/10.1007/s10948-008-0433-x (visited on 07/29/2021) (cit. on pp. 52, 153).

[59] U. Fano. "Effects of Configuration Interaction on Intensities and Phase Shifts". In: *Phys. Rev.* 124.6 (Dec. 15, 1961), pp. 1866–1878. DOI: 10.1103/PhysRev.124.1866. URL: https://link.aps.org/doi/10.1103/PhysRev.124.1866 (visited on 07/27/2021) (cit. on p. 52).

[60] Peter Blaha et al. "WIEN2k: An APW+lo Program for Calculating the Properties of Solids". In: *J. Chem. Phys.* 152.7 (Feb. 21, 2020), p. 074101. ISSN: 0021-9606. DOI: 10.1063/1.5143061. URL: https://aip.scitation.org/doi/10.1063/1.5143061 (visited on 07/29/2021) (cit. on p. 61).

[61] *VASP - Vienna Ab Initio Simulation Package*. URL: https://www.vasp.at/ (visited on 07/29/2021) (cit. on p. 61).

[62] L. D. Landau. "The Theory of a Fermi Liquid". In: *Zh. Eksp. Teor. Fiz.* 30.6 (1956), p. 1058 (cit. on pp. 62, 68).

[63] Lars Hedin. "On Correlation Effects in Electron Spectroscopies and theG-Wapproximation". In: *J. Phys.: Condens. Matter* 11.42 (Oct. 1999), R489–R528. ISSN: 0953-8984. DOI: 10.1088/0953-8984/11/42/201. URL: https://doi.org/10.1088/0953-8984/11/42/201 (visited on 08/05/2021) (cit. on p. 67).

[64] Lucia Reining. "The GW Approximation: Content, Successes and Limitations". In: *WIREs Computational Molecular Science* 8.3 (2018), e1344. ISSN: 1759-0884. DOI: 10.1002/wcms.1344. URL: https://onlinelibrary.wiley.com/doi/abs/10.1002/wcms.1344 (visited on 08/06/2021) (cit. on p. 67).

[65] R. Franz and G. Wiedemann. "Ueber Die Wärme-Leitungsfähigkeit Der Metalle". In: *Ann. Phys.* 165.8 (1853), pp. 497–531. DOI: 10.1002/andp.18531650802 (cit. on p. 68).

[66] R. A. Cooper et al. "Anomalous Criticality in the Electrical Resistivity of $La_{2-x}sr_xCuO_4$". In: *Science* 323.5914 (2009), pp. 603–607. DOI: 10.1126/science.1165015. URL: https://science.sciencemag.org/content/323/5914/603 (cit. on p. 69).

[67] S. Kasahara et al. "Evolution from Non-Fermi- to Fermi-Liquid Transport via Isovalent Doping in $BaFe_2(As_{1-x}P_x)_2$ Superconductors". In: *Phys. Rev. B* 81.18 (May 2010), p. 184519. DOI: 10.1103/PhysRevB.81.184519. URL: https://link.aps.org/doi/10.1103/PhysRevB.81.184519 (cit. on p. 69).

[68] K. Jin et al. "Link between Spin Fluctuations and Electron Pairing in Copper Oxide Superconductors". In: *Nature* 476 (2011), pp. 73–75. DOI: 10.1038/nature10308. URL: https://www.nature.com/articles/nature10308 (cit. on pp. 69, 140).

[69] Heike Pfau et al. "Thermal and Electrical Transport across a Magnetic Quantum Critical Point". In: *Nature* 484.7395 (Apr. 1, 2012), pp. 493–497. ISSN: 1476-4687. DOI: 10.1038/nature11072. URL: https://doi.org/10.1038/nature11072 (cit. on p. 69).

[70] M. J. Rice. "Electron-Electron Scattering in Transition Metals". In: *Phys. Rev. Lett.* 20.25 (June 17, 1968), pp. 1439–1441. DOI: 10.1103/PhysRevLett.20.1439. URL: https://link.aps.org/doi/10.1103/PhysRevLett.20.1439 (visited on 08/06/2021) (cit. on p. 70).

[71] K. Kadowaki and S. B. Woods. "Universal Relationship of the Resistivity and Specific Heat in Heavy-Fermion Compounds". In: *Solid State Communications* 58.8 (May 1, 1986), pp. 507–509. ISSN: 0038-1098. DOI: 10.1016/0038-1098(86)90785-4. URL: https://www.sciencedirect.com/science/article/pii/0038109886907854 (visited on 08/06/2021) (cit. on p. 70).

[72] A. C. Jacko, J. O. Fjærestad, and B. J. Powell. "A Unified Explanation of the Kadowaki–Woods Ratio in Strongly Correlated Metals". In: *Nature Phys* 5.6 (6 June 2009), pp. 422–425. ISSN: 1745-2481. DOI: 10.1038/nphys1249. URL: https://www.nature.com/articles/nphys1249 (visited on 08/06/2021) (cit. on pp. 71, 140–142).

[73] A. Kaminski et al. "Identifying the Background Signal in Angle-Resolved Photoemission Spectra of High-Temperature Cuprate Superconductors". In: *Phys. Rev. B* 69.21 (June 30, 2004), p. 212509. DOI: 10.1103/PhysRevB.69.212509. URL: https://link.aps.org/doi/10.1103/PhysRevB.69.212509 (visited on 11/16/2017) (cit. on pp. 83, 85).

[74] D. A. Shirley. "High-Resolution X-Ray Photoemission Spectrum of the Valence Bands of Gold". In: *Phys. Rev. B* 5.12 (June 15, 1972), pp. 4709–4714. DOI: 10.1103/PhysRevB.5.4709. URL: https://link.aps.org/doi/10.1103/PhysRevB.5.4709 (visited on 04/27/2018) (cit. on pp. 83, 86).

[75] János Végh. "The Shirley Background Revised". In: *Journal of Electron Spectroscopy and Related Phenomena* 151.3 (May 1, 2006), pp. 159–164. ISSN: 0368-2048. DOI: 10.1016/j.elspec.2005.12.002. URL: http://www.sciencedirect.com/science/article/pii/S0368204805005220 (visited on 04/27/2018) (cit. on p. 85).

[76] C. E. Matt et al. "Direct Observation of Orbital Hybridisation in a Cuprate Superconductor". In: *Nat Commun* 9.1 (Mar. 6, 2018), pp. 1–7. ISSN: 2041-1723. DOI: 10.1038/s41467-018-03266-0. URL: https://www.nature.com/articles/s41467-018-03266-0 (visited on 01/14/2020) (cit. on pp. 85, 87, 105–107, 110, 126, 135, 165).

[77] T. Sato et al. "Observation of Dx2-Y2-Like Superconducting Gap in an Electron-Doped High-Temperature Superconductor". In: *Science* 291.5508 (Feb. 23, 2001), pp. 1517–1519. DOI: 10.1126/science.1058021. URL: https://www.science.org/lookup/doi/10.1126/science.1058021 (visited on 09/15/2021) (cit. on p. 87).

[78] J. Mesot et al. "Determination of the Fermi Surface in High-T_c Superconductors by Angle-Resolved Photoemission Spectroscopy". In: *Phys. Rev. B* 63.22 (May 23, 2001), p. 224516. DOI: 10.1103/PhysRevB.63.224516. URL: https://link.aps.org/doi/10.1103/PhysRevB.63.224516 (visited on 09/15/2021) (cit. on p. 87).

[79] F. Ronning et al. "Evolution of a Metal to Insulator Transition in $Ca_{2-x}Na_xCuO_2Cl_2$ as Seen by Angle-Resolved Photoemission". In: *Phys. Rev. B* 67.16 (Apr. 2, 2003), p. 165101. DOI: 10.1103/PhysRevB.67.165101. URL: https://link.aps.org/doi/10.1103/PhysRevB.67.165101 (visited on 09/15/2021) (cit. on p. 87).

[80] T. Sato et al. "Evolution of Metallic States from the Hubbard Band in the Two-Dimensional Mott System $BaCo_{1-x}Ni_xS_2$". In: *Phys. Rev. B* 64.7 (July 13, 2001), p. 075103. DOI: 10.1103/PhysRevB.64.075103. URL: https://link.aps.org/doi/10.1103/PhysRevB.64.075103 (visited on 09/15/2021) (cit. on p. 87).

[81] H.-B. Yang et al. "Fermi Surface Evolution and Luttinger Theorem in Na_xCoO_2: A Systematic Photoemission Study". In: *Phys. Rev. Lett.* 95.14 (Sept. 27, 2005), p. 146401. DOI: 10.1103/PhysRevLett.95.146401. URL: https://link.aps.org/doi/10.1103/PhysRevLett.95.146401 (visited on 09/15/2021) (cit. on p. 87).

[82] D. Qian et al. "Complete *d*-Band Dispersion Relation in Sodium Cobaltates". In: *Phys. Rev. Lett.* 97.18 (Nov. 3, 2006), p. 186405. DOI: 10.1103/PhysRevLett.97.186405. URL: https://link.aps.org/doi/10.1103/PhysRevLett.97.186405 (visited on 09/15/2021) (cit. on p. 87).

[83] B. J. Kim et al. "Distinct Spinon and Holon Dispersions in Photoemission Spectral Functions from One-Dimensional SrCuO2". In: *Nature Phys* 2.6 (6 June 2006), pp. 397–401. ISSN: 1745-2481. DOI: 10.1038/nphys316. URL: https://www.nature.com/articles/nphys316 (visited on 09/15/2021) (cit. on p. 87).

[84] Wentao Zhang et al. "High Energy Dispersion Relations for the High Temperature $Bi_2Sr_2CaCu_2O_8$ Superconductor from Laser-Based Angle-Resolved Photoemission Spectroscopy". In: *Phys. Rev. Lett.* 101.1 (July 2, 2008), p. 017002. DOI: 10.1103/PhysRevLett.101.017002. URL: https://link.aps.org/doi/10.1103/PhysRevLett.101.017002 (visited on 09/15/2021) (cit. on p. 87).

[85] P. Richard et al. "Observation of Dirac Cone Electronic Dispersion in $BaFe_2As_2$". In: *Phys. Rev. Lett.* 104.13 (Mar. 29, 2010), p. 137001. DOI: 10.1103/PhysRevLett.104.137001. URL: https://link.aps.org/doi/10.1103/PhysRevLett.104.137001 (visited on 09/15/2021) (cit. on p. 87).

[86] P. Zhang et al. "A Precise Method for Visualizing Dispersive Features in Image Plots". In: *Review of Scientific Instruments* 82.4 (Apr. 1, 2011), p. 043712. ISSN: 0034-6748. DOI: 10.1063/1.3585113. URL: https://aip.scitation.org/doi/10.1063/1.3585113 (visited on 08/12/2020) (cit. on p. 89).

[87] P. Schwaller et al. "Structure and Fermi Surface Mapping of a Modulation-Free PbBiSrCaCuO High-Temperature Superconductor". In: *Journal of Electron Spectroscopy and Related Phenomena*. Proceedings of the Sixth International Conference on Electron Spectroscopy 76 (Dec. 29, 1995), pp. 127–132. ISSN: 0368-2048. DOI: 10.1016/0368-2048(95)02415-8. URL: https://www.sciencedirect.com/science/article/pii/0368204895024158 (visited on 08/13/2021) (cit. on p. 90).

[88] Haoxiang Li et al. "Coherent Organization of Electronic Correlations as a Mechanism to Enhance and Stabilize High- T C Cuprate Superconductivity". In: *Nature Communications* 9.1 (Jan. 2, 2018), p. 26. ISSN: 2041-1723. DOI: 10.1038/s41467-017-02422-2. URL: https://www.nature.com/articles/s41467-017-02422-2 (visited on 12/10/2018) (cit. on pp. 91, 92, 177).

[89] C. M. Varma et al. "Phenomenology of the Normal State of Cu-O High-Temperature Superconductors". In: *Phys. Rev. Lett.* 63.18 (Oct. 1989), pp. 1996–1999. DOI: 10.1103/PhysRevLett.63.1996. URL: https://link.aps.org/doi/10.1103/PhysRevLett.63.1996 (cit. on pp. 91, 142).

[90] C. M. Varma et al. "Erratum: Phenomenology of the Normal State of Cu-O High-Temperature Superconductors [Phys. Rev. Lett. 63, 1996 (1989)]". In: *Phys. Rev. Lett.* 64.4 (Jan. 22, 1990), pp. 497–497. DOI: 10.1103/PhysRevLett.64.497. URL: https://link.aps.org/doi/10.1103/PhysRevLett.64.497 (visited on 09/15/2021) (cit. on p. 91).

[91] Elihu Abrahams and C. M. Varma. "What Angle-Resolved Photoemission Experiments Tell about the Microscopic Theory for High-Temperature Superconductors". In: *PNAS* 97.11 (May 23, 2000), pp. 5714–5716. ISSN: 0027-8424, 1091-6490. DOI: 10.1073/pnas.100118797. pmid: 10811895. URL: https://www.pnas.org/content/97/11/5714 (visited on 09/15/2021) (cit. on pp. 93, 140).

[92] Bruno Marchon et al. "The Head-Disk Interface Roadmap to an Areal Density of Tbit/In2". In: *Advances in Tribology* 2013 (Mar. 20, 2013), e521086. ISSN: 1687-5915. DOI: 10.1155/2013/521086. URL: https://www.hindawi.com/journals/at/2013/521086/ (visited on 06/29/2021) (cit. on p. 93).

[93] *Creative Commons — Attribution 3.0 Unported — CC BY 3.0*. Version 3.0. URL: https://creativecommons.org/licenses/by/3.0/ (visited on 06/29/2021) (cit. on p. 93).

[94] Gordon E. Moore. "Cramming More Components onto Integrated Circuits, Reprinted from Electronics, Volume 38, Number 8, April 19, 1965, Pp.114 Ff." In: *IEEE Solid-State Circuits Society Newsletter* 11.3 (Sept. 2006), pp. 33–35. ISSN: 1098-4232. DOI: 10.1109/N-SSC.2006.4785860 (cit. on p. 94).

[95] D. E. Shai et al. "Quasiparticle Mass Enhancement and Temperature Dependence of the Electronic Structure of Ferromagnetic $SrRuO_3$ Thin Films". In: *Phys. Rev. Lett.* 110.8 (Feb. 22, 2013), p. 087004. DOI: 10.1103/PhysRevLett.110.087004. URL: https://link.aps.org/doi/10.1103/PhysRevLett.110.087004 (visited on 11/25/2020) (cit. on pp. 94, 95).

[96] I. Giaever, H. R. Hart, and K. Megerle. "Tunneling into Superconductors at Temperatures below 1\ifmmode\^circ\else\textdegree\fi{}K". In: *Phys. Rev.* 126.3 (May 1, 1962), pp. 941–948. DOI: 10.1103/PhysRev.126.941. URL: https://link.aps.org/doi/10.1103/PhysRev.126.941 (visited on 11/25/2020) (cit. on pp. 94, 95).

[97] A. D. B. Woods, W. Cochran, and B. N. Brockhouse. "Lattice Dynamics of Alkali Halide Crystals". In: *Phys. Rev.* 119.3 (Aug. 1, 1960), pp. 980–999. DOI: 10.1103/PhysRev.119.980. URL: https://link.aps.org/doi/10.1103/PhysRev.119.980 (visited on 11/25/2020) (cit. on pp. 94, 95).

[98] B. Dalla Piazza et al. "Fractional Excitations in the Square-Lattice Quantum Antiferromagnet". In: *Nature Physics* 11.1 (2015), pp. 62–68. DOI: 10.1038/nphys3172. URL: https://doi.org/10.1038/nphys3172 (cit. on pp. 94, 95).

[99] W Wan et al. "Temperature Dependence of the (π,0) Anomaly in the Excitation Spectrum of the 2D Quantum Heisenberg Antiferromagnet". In: *Journal of Physics: Condensed Matter* 32.37 (June 2020), p. 374007. DOI: 10.1088/1361-648x/ab757a. URL: https://doi.org/10.1088%2F1361-648x%2Fab757a (cit. on pp. 94, 95).

[100] J. Ahrens, Berk Geveci, and Charles Law. "ParaView: An End-User Tool for Large Data Visualization". In: *Visualization Handbook* (Jan. 1, 2005) (cit. on p. 94).

[101] Andriy Fedorov et al. "3D Slicer as an Image Computing Platform for the Quantitative Imaging Network". In: *Magn Reson Imaging* 30.9 (Nov. 2012), pp. 1323–1341. ISSN: 0730-725X. DOI: 10.1016/j.mri.2012.05.001. pmid: 22770690. URL: https://www.ncbi.nlm.nih.gov/pmc/articles/PMC3466397/ (visited on 12/01/2020) (cit. on p. 94).

[102] *Mayavi: 3D Scientific Data Visualization and Plotting in Python — Mayavi 4.7.2 Documentation*. URL: https://docs.enthought.com/mayavi/mayavi/ (visited on 02/25/2021) (cit. on p. 94).

[103] *VisIt — Weapons and Complex Integration*. URL: https://wci.llnl.gov/simulation/computer-codes/visit (visited on 02/25/2021) (cit. on p. 94).

[104] Jakob Lass et al. "MJOLNIR: A Software Package for Multiplexing Neutron Spectrometers". In: *SoftwareX* 12 (July 1, 2020), p. 100600. ISSN: 2352-7110. DOI: 10.1016/j.softx.2020.100600. URL: http://www.sciencedirect.com/science/article/pii/S2352711020303137 (visited on 11/13/2020) (cit. on p. 95).

[105] Conrad Stansbury and Alessandra Lanzara. "PyARPES: An Analysis Framework for Multimodal Angle-Resolved Photoemission Spectroscopies". In: *SoftwareX* 11 (Jan. 1, 2020), p. 100472. ISSN: 2352-7110. DOI: 10.1016/j.softx.2020.100472. URL: http://www.sciencedirect.com/science/article/pii/S2352711019301633 (visited on 11/04/2020) (cit. on p. 95).

[106] *Data-Slicer/Index.Rst at Master · Kuadrat/Data-Slicer*. GitHub. URL: https://github.com/kuadrat/data-slicer (visited on 08/26/2021) (cit. on p. 96).

[107] *Jupyter and the Future of IPython — IPython*. URL: https://ipython.org/ (visited on 11/09/2020) (cit. on p. 97).

[108] *Ds_arpes_plugin's Documentation — Ds_arpes_plugin Documentation*. URL: https://ds-arpes-plugin.readthedocs.io/en/latest/index.html (visited on 12/02/2020) (cit. on p. 97).

[109] *LQMR*. URL: https://www.physik.uzh.ch/groups/chang/ (visited on 09/13/2021) (cit. on p. 101).

[110] S. N. Ruddlesden and P. Popper. "The Compound Sr3Ti2O7 and Its Structure". In: *Acta Cryst* 11.1 (1 Jan. 10, 1958), pp. 54–55. ISSN: 0365-110X. DOI: 10.1107/S0365110X58000128. URL: //scripts.iucr.org/cgi-bin/paper?a02171 (visited on 09/02/2021) (cit. on p. 103).

[111] S. S. P. Parkin et al. "Model Family of High-Temperature Superconductors: $Tl_mCa_{n-1}Ba_2Cu_nO_{2(n+1)+m}$ ($m = 1, 2$; $n = 1, 2, 3$)". In: *Phys. Rev. B* 38.10 (Oct. 1, 1988), pp. 6531–6537. DOI: 10.1103/PhysRevB.38.6531. URL: https://link.aps.org/doi/10.1103/PhysRevB.38.6531 (visited on 09/02/2021) (cit. on p. 103).

[112] P. Haldar et al. "Bulk Superconductivity at 122 K in {T1 $(Ba,Ca)_2$ Ca_3 Cu_4 $O_{10.5+\delta}$} with Four Consecutive Copper Layers". In: *Science* (Sept. 2, 1988). URL: https://www.science.org/doi/abs/10.1126/science.241.4870.1198 (visited on 09/02/2021) (cit. on p. 103).

[113] D. J. Scalapino. "A Common Thread: The Pairing Interaction for Unconventional Superconductors". In: *Rev. Mod. Phys.* 84.4 (Oct. 8, 2012), pp. 1383–1417. DOI: 10.1103/RevModPhys.84.1383. URL: https://link.aps.org/doi/10.1103/RevModPhys.84.1383 (visited on 06/17/2021) (cit. on pp. 103, 104).

[114] B. Keimer et al. "From Quantum Matter to High-Temperature Superconductivity in Copper Oxides". In: *Nature* 518.7538 (Feb. 2015), pp. 179–186. ISSN: 1476-4687. DOI: 10.1038/nature14165. URL: https://www.nature.com/articles/nature14165 (visited on 01/31/2019) (cit. on pp. 103, 104).

[115] Patrick A. Lee, Naoto Nagaosa, and Xiao-Gang Wen. "Doping a Mott Insulator: Physics of High-Temperature Superconductivity". In: *Rev. Mod. Phys.* 78.1 (Jan. 6, 2006), pp. 17–85. DOI: 10.1103/RevModPhys.78.17. URL: https://link.aps.org/doi/10.1103/RevModPhys.78.17 (visited on 06/17/2021) (cit. on p. 103).

[116] J. A. Slezak et al. "Imaging the Impact on Cuprate Superconductivity of Varying the Interatomic Distances within Individual Crystal Unit Cells". In: *PNAS* 105.9 (Mar. 4, 2008), pp. 3203–3208 (cit. on p. 105).

[117] Michael R. Norman. "Modulated Pairs in Superconducting Cuprates". In: *PNAS* 105.9 (Mar. 4, 2008), pp. 3173–3174 (cit. on p. 105).

[118] Hirofumi Sakakibara et al. "Two-Orbital Model Explains the Higher Transition Temperature of the Single-Layer Hg-Cuprate Superconductor Compared to That of the La-Cuprate Superconductor". In: *Phys. Rev. Lett.* 105.5 (July 30, 2010), p. 057003. DOI: 10.1103/PhysRevLett.105.057003. URL: https://link.aps.org/doi/10.1103/PhysRevLett.105.057003 (visited on 09/01/2021) (cit. on pp. 105, 106).

[119] C. Weber et al. "Scaling of the Transition Temperature of Hole-Doped Cuprate Superconductors with the Charge-Transfer Energy". In: *EPL* 100.3 (Nov. 2012), p. 37001. ISSN: 0295-5075. DOI: 10.1209/0295-5075/100/37001. URL: https://doi.org/10.1209/0295-5075/100/37001 (visited on 06/17/2021) (cit. on p. 105).

[120] Ran Adler et al. *Correlated Material Design: Prospects and Challenges*. July 1, 2018. arXiv: 1807.00398. URL: http://arxiv.org/abs/1807.00398 (visited on 07/04/2018) (cit. on p. 105).

[121] James W. Furness et al. "An Accurate First-Principles Treatment of Doping-Dependent Electronic Structure of High-Temperature Cuprate Superconductors". In: *Communications Physics* 1.1 (Mar. 22, 2018), p. 11. ISSN: 2399-3650. DOI: 10.1038/s42005-018-0009-4. URL: https://www.nature.com/articles/s42005-018-0009-4 (visited on 03/23/2018) (cit. on p. 105).

[122] Liviu Hozoi et al. "Ab Initio Determination of Cu 3 d Orbital Energies in Layered Copper Oxides". In: *Sci Rep* 1.1 (1 Aug. 16, 2011), p. 65. ISSN: 2045-2322. DOI: 10.1038/srep00065. URL: https://www.nature.com/articles/srep00065 (visited on 06/17/2021) (cit. on p. 105).

[123] Hirofumi Sakakibara et al. "Origin of the Material Dependence of T_c in the Single-Layered Cuprates". In: *Phys. Rev. B* 85.6 (Feb. 1, 2012), p. 064501. DOI: 10.1103/PhysRevB.85.064501. URL: https://link.aps.org/doi/10.1103/PhysRevB.85.064501 (visited on 02/11/2019) (cit. on pp. 105, 106).

[124] K. S. Novoselov et al. "Two-Dimensional Gas of Massless Dirac Fermions in Graphene". In: *Nature* 438.7065 (Nov. 10, 2005), pp. 197–200. ISSN: 1476-4687. DOI: 10.1038/nature04233. pmid: 16281030 (cit. on pp. 108, 109).

[125] Yong Xu, Fan Zhang, and Chuanwei Zhang. "Structured Weyl Points in Spin-Orbit Coupled Fermionic Superfluids". In: *Phys. Rev. Lett.* 115.26 (Dec. 30, 2015), p. 265304. DOI: 10.1103/PhysRevLett.115.265304. URL: https://link.aps.org/doi/10.1103/PhysRevLett.115.265304 (visited on 09/03/2021) (cit. on p. 108).

[126] Alexey A. Soluyanov et al. "Type-II Weyl Semimetals". In: *Nature* 527.7579 (7579 Nov. 2015), pp. 495–498. ISSN: 1476-4687. DOI: 10.1038/nature15768. URL: https://www.nature.com/articles/nature15768 (visited on 09/03/2021) (cit. on p. 108).

[127] M. Z. Hasan and C. L. Kane. "Colloquium: Topological Insulators". In: *Rev. Mod. Phys.* 82.4 (Nov. 8, 2010), pp. 3045–3067. DOI: 10.1103/RevModPhys.82.3045. URL: https://link.aps.org/doi/10.1103/RevModPhys.82.3045 (visited on 09/03/2021) (cit. on p. 108).

[128] Z. K. Liu et al. "Discovery of a Three-Dimensional Topological Dirac Semimetal, Na3Bi". In: *Science* (Feb. 21, 2014). URL: https://www.science.org/doi/abs/10.1126/science.1245085 (visited on 09/03/2021) (cit. on pp. 108, 109).

[129] Madhab Neupane et al. "Observation of a Three-Dimensional Topological Dirac Semimetal Phase in High-Mobility Cd3As2". In: *Nat Commun* 5.1 (1 May 7, 2014), p. 3786. ISSN: 2041-1723. DOI: 10.1038/ncomms4786. URL: https://www.nature.com/articles/ncomms4786 (visited on 09/03/2021) (cit. on pp. 108, 109).

[130] Sergey Borisenko et al. *Experimental Realization of a Three-Dimensional Dirac Semimetal*. Version 1. Sept. 30, 2013. arXiv: 1309.7978 [cond-mat]. URL: http://arxiv.org/abs/1309.7978 (visited on 09/03/2021) (cit. on p. 108).

[131] Jimin Kim et al. "Observation of Tunable Band Gap and Anisotropic Dirac Semimetal State in Black Phosphorus". In: *Science* (Aug. 14, 2015). URL: https://www.science.org/doi/abs/10.1126/science.aaa6486 (visited on 09/03/2021) (cit. on p. 108).

[132] Tay-Rong Chang et al. "Type-II Symmetry-Protected Topological Dirac Semimetals". In: *Phys Rev Lett* 119.2 (July 14, 2017), p. 026404. ISSN: 1079-7114. DOI: 10.1103/PhysRevLett.119.026404. pmid: 28753359 (cit. on p. 108).

[133] Lukas Muechler et al. "Topological Nonsymmorphic Metals from Band Inversion". In: *Phys. Rev. X* 6.4 (Dec. 29, 2016), p. 041069. DOI: 10.1103/PhysRevX.6.041069. URL: https://link.aps.org/doi/10.1103/PhysRevX.6.041069 (visited on 09/03/2021) (cit. on p. 108).

[134] Hai-Xiao Wang et al. "Type-II Dirac Photons". In: *npj Quant Mater* 2.1 (1 Sept. 22, 2017), pp. 1–8. ISSN: 2397-4648. DOI: 10.1038/s41535-017-0058-z. URL: https://www.nature.com/articles/s41535-017-0058-z (visited on 09/03/2021) (cit. on p. 108).

[135] Mingzhe Yan et al. "Lorentz-Violating Type-II Dirac Fermions in Transition Metal Dichalcogenide PtTe2". In: *Nat Commun* 8.1 (1 Aug. 15, 2017), p. 257. ISSN: 2041-1723. DOI: 10.1038/s41467-017-00280-6. URL: https://www.nature.com/articles/s41467-017-00280-6 (visited on 09/03/2021) (cit. on pp. 108, 109).

[136] Kenan Zhang et al. "Experimental Evidence for Type-II Dirac Semimetal in $PtSe_2$". In: *Phys. Rev. B* 96.12 (Sept. 1, 2017), p. 125102. DOI: 10.1103/PhysRevB.96.125102. URL: https://link.aps.org/doi/10.1103/PhysRevB.96.125102 (visited on 09/03/2021) (cit. on p. 108).

[137] Han-Jin Noh et al. "Experimental Realization of Type-II Dirac Fermions in a $PdTe_2$ Superconductor". In: *Phys. Rev. Lett.* 119.1 (July 5, 2017), p. 016401. DOI: 10.1103/PhysRevLett.119.016401. URL: https://link.aps.org/doi/10.1103/PhysRevLett.119.016401 (visited on 09/03/2021) (cit. on p. 108).

[138] Fucong Fei et al. "Band Structure Perfection and Superconductivity in Type-II Dirac Semimetal Ir1-xPtxTe2". In: *Advanced Materials* 30.35 (2018), p. 1801556. ISSN: 1521-4095. DOI: 10.1002/adma.201801556. URL: https://onlinelibrary.wiley.com/doi/abs/10.1002/adma.201801556 (visited on 09/03/2021) (cit. on p. 110).

[139] M. Uchida et al. "Orbital Characters of Three-Dimensional Fermi Surfaces in $Eu_{2-x}Sr_xNiO_4$ as Probed by Soft-x-Ray Angle-Resolved Photoemission Spectroscopy". In: *Phys. Rev. B* 84.24 (Dec. 19, 2011), p. 241109. DOI: 10.1103/PhysRevB.84.241109. URL: https://link.aps.org/doi/10.1103/PhysRevB.84.241109 (visited on 09/03/2021) (cit. on p. 110).

[140] R. S. Markiewicz et al. "One-Band Tight-Binding Model Parametrization of the High-T_c Cuprates Including the Effect of k_z Dispersion". In: *Phys. Rev. B* 72.5 (Aug. 2005), p. 054519. DOI: 10.1103/PhysRevB.72.054519. URL: https://link.aps.org/doi/10.1103/PhysRevB.72.054519 (cit. on pp. 111, 115).

[141] V. N. Strocov. "Intrinsic Accuracy in 3-Dimensional Photoemission Band Mapping". In: *Journal of Electron Spectroscopy and Related Phenomena* 130.1 (July 1, 2003), pp. 65–78. ISSN: 0368-2048. DOI: 10.1016/S0368-2048(03)00054-9. URL: https://www.sciencedirect.com/science/article/pii/S0368204803000549 (visited on 09/02/2021) (cit. on pp. 111, 133).

[142] J Chang et al. "Electronic Structure near the 1/8-Anomaly in La-Based Cuprates". In: *New J. Phys.* 10.10 (2008), p. 103016. URL: http://stacks.iop.org/1367-2630/10/i=10/a=103016 (cit. on p. 112).

[143] P. D. C. King et al. "Structural Origin of Apparent Fermi Surface Pockets in Angle-Resolved Photoemission of $Bi_2Sr_{2-x}La_xCuO_{6+\delta}$". In: *Phys. Rev. Lett.* 106.12 (Mar. 24, 2011), p. 127005. DOI: 10.1103/PhysRevLett.106.127005. URL: https://link.aps.org/doi/10.1103/PhysRevLett.106.127005 (visited on 06/17/2021) (cit. on pp. 112, 121).

[144] O. J. Lipscombe et al. "Persistence of High-Frequency Spin Fluctuations in Overdoped Superconducting $La_{2-x}Sr_xCuO_4$ ($x = 0.22$)". In: *Phys. Rev. Lett.* 99.6 (Aug. 8, 2007), p. 067002. DOI: 10.1103/PhysRevLett.99.067002. URL: https://link.aps.org/doi/10.1103/PhysRevLett.99.067002 (visited on 03/26/2019) (cit. on p. 112).

[145] J. Chang et al. "Spin Density Wave Induced Disordering of the Vortex Lattice in Superconducting $La_{2-x}Sr_xCuO_4$". In: *Phys. Rev. B* 85.13 (Apr. 18, 2012), p. 134520. DOI: 10.1103/PhysRevB.85.134520. URL: https://link.aps.org/doi/10.1103/PhysRevB.85.134520 (visited on 06/17/2021) (cit. on p. 112).

[146] C. G. Fatuzzo et al. "Nodal Landau Fermi-Liquid Quasiparticles in Overdoped $La_{1.77}Sr_{0.23}CuO_4$". In: *Phys. Rev. B* 89.20 (May 8, 2014), p. 205104. DOI: 10.1103/PhysRevB.89.205104. URL: https://link.aps.org/doi/10.1103/PhysRevB.89.205104 (visited on 06/17/2021) (cit. on pp. 112, 121, 141).

[147] J. Chang et al. "Anisotropic Breakdown of Fermi Liquid Quasiparticle Excitations in Overdoped $La_{2-x}Sr_xCuO_4$". In: *Nature Communications* 4 (Oct. 7, 2013), p. 2559. DOI: 10.1038/ncomms3559. URL: https://www.nature.com/articles/ncomms3559 (visited on 03/28/2019) (cit. on pp. 112, 134, 139–141, 143, 179).

[148] V. N. Strocov et al. "High-Resolution Soft X-Ray Beamline ADRESS at the Swiss Light Source for Resonant Inelastic X-Ray Scattering and Angle-Resolved Photoelectron Spectroscopies". In: *J. Synchrotron Rad.* 17 (2010), pp. 631–643. DOI: 10.1107/S0909049510019862 (cit. on p. 112).

[149] V. N. Strocov et al. "Soft-X-Ray ARPES Facility at the ADRESS Beamline of the SLS: Concepts, Technical Realisation and Scientific Applications". In: *J Synchrotron Radiat* 21 (Pt 1 Jan. 2014), pp. 32–44. ISSN: 1600-5775. DOI: 10.1107/S1600577513019085. pmid: 24365914 (cit. on pp. 112, 117, 135).

[150] U. Flechsig, L. Patthey, and T. Schmidt. "Proceedings, 8th International Conference on Synchrotron Radiation Instrumentation (SRI 03)". In: *AIP Conf.Proc.* 705 (2004). Ed. by Tony Warwick et al., p. 316. URL: https://inspirehep.net/literature/662282 (visited on 06/17/2021) (cit. on p. 117).

[151] Aliaksandr V. Krukau et al. "Influence of the Exchange Screening Parameter on the Performance of Screened Hybrid Functionals". In: *J. Chem. Phys.* 125.22 (Dec. 14, 2006), p. 224106. ISSN: 0021-9606. DOI: 10.1063/1.2404663. URL: https://aip.scitation.org/doi/10.1063/1.2404663 (visited on 06/17/2021) (cit. on p. 119).

[152] X. J. Zhou et al. "Universal Nodal Fermi Velocity". In: *Nature* 423.6938 (6938 May 2003), pp. 398–398. ISSN: 1476-4687. DOI: 10.1038/423398a. URL: https://www.nature.com/articles/423398a (visited on 06/17/2021) (cit. on p. 121).

[153] T. Yoshida et al. "Low-Energy Electronic Structure of the High-Tccuprates La2-xSrxCuO4studied by Angle-Resolved Photoemission Spectroscopy". In: *J. Phys.: Condens. Matter* 19.12 (Mar. 2007), p. 125209. ISSN: 0953-8984. DOI: 10.1088/0953-8984/19/12/125209. URL: https://doi.org/10.1088/0953-8984/19/12/125209 (visited on 06/17/2021) (cit. on pp. 121, 136, 141).

[154] J. A. Rosen et al. "Surface-Enhanced Charge-Density-Wave Instability in Underdoped $Bi_2Sr_{2-x}La_xCuO_{6+\delta}$". In: *Nature Communications* 4 (July 1, 2013), p. 1977. ISSN: 2041-1723. DOI: 10.1038/ncomms2977. URL: https://www.nature.com/articles/ncomms2977 (visited on 05/07/2018) (cit. on p. 121).

[155] Jing Xia et al. "Polar Kerr-Effect Measurements of the High-Temperature $YBa_2Cu_3O_{6+x}$ Superconductor: Evidence for Broken Symmetry near the Pseudogap Temperature". In: *Phys. Rev. Lett.* 100.12 (Mar. 28, 2008), p. 127002. DOI: 10.1103/PhysRevLett.100.127002. URL: https://link.aps.org/doi/10.1103/PhysRevLett.100.127002 (visited on 06/17/2021) (cit. on p. 121).

[156] W. Meevasana et al. "Hierarchy of Multiple Many-Body Interaction Scales in High-Temperature Superconductors". In: *Phys. Rev. B* 75.17 (May 9, 2007), p. 174506. DOI: 10.1103/PhysRevB.75.174506. URL: https://link.aps.org/doi/10.1103/PhysRevB.75.174506 (visited on 08/09/2018) (cit. on p. 121).

[157] L. L. Tao and Evgeny Y. Tsymbal. "Two-Dimensional Type-II Dirac Fermions in a $LaAlO_3/LaNiO_3/LaAlO_3$ Quantum Well". In: *Phys. Rev. B* 98.12 (Sept. 4, 2018), p. 121102. DOI: 10.1103/PhysRevB.98.121102. URL: https://link.aps.org/doi/10.1103/PhysRevB.98.121102 (visited on 06/17/2021) (cit. on p. 124).

[158] Y. Y. Peng et al. "Influence of Apical Oxygen on the Extent of In-Plane Exchange Interaction in Cuprate Superconductors". In: *Nature Phys* 13.12 (12 Dec. 2017), pp. 1201–1206. ISSN: 1745-2481. DOI: 10.1038/nphys4248. URL: https://www.nature.com/articles/nphys4248 (visited on 06/17/2021) (cit. on p. 125).

[159] J. Graf et al. "Universal High Energy Anomaly in the Angle-Resolved Photoemission Spectra of High Temperature Superconductors: Possible Evidence of Spinon and Holon Branches". In: *Phys. Rev. Lett.* 98.6 (Feb. 7, 2007), p. 067004. DOI: 10.1103/PhysRevLett.98.067004. URL: https://link.aps.org/doi/10.1103/PhysRevLett.98.067004 (visited on 06/17/2021) (cit. on p. 127).

[160] T. Valla et al. "High-Energy Kink Observed in the Electron Dispersion of High-Temperature Cuprate Superconductors". In: *Phys. Rev. Lett.* 98.16 (Apr. 18, 2007), p. 167003. DOI: 10.1103/PhysRevLett.98.167003. URL: https://link.aps.org/doi/10.1103/PhysRevLett.98.167003 (visited on 06/17/2021) (cit. on p. 127).

[161] J. Chang et al. "When Low- and High-Energy Electronic Responses Meet in Cuprate Superconductors". In: *Phys. Rev. B* 75.22 (June 14, 2007), p. 224508. DOI: 10.1103/PhysRevB.75.224508. URL: https://link.aps.org/doi/10.1103/PhysRevB.75.224508 (visited on 06/21/2018) (cit. on p. 127).

[162] Sujay Ray and Tanmoy Das. "Theory of Angle-Dependent Marginal Fermi Liquid Self-Energy and Its Existence at All Dopings in Cuprates". In: *J. Phys. Condens. Matter.* 31.36 (June 2019), p. 365603. DOI: 10.1088/1361-648x/ab25b8 (cit. on p. 134).

[163] Tadashi Adachi et al. "Evolution of the Electronic State through the Reduction Annealing in Electron-Doped $Pr_{1.3-x}La_{0.7}Ce_xCuO_{4+\delta}$ (x=0.10) Single Crystals: Antiferromagnetism, Kondo Effect, and Superconductivity". In: *J. Phys. Soc. Jpn.* 82.6 (2013), p. 063713. URL: http://jpsj.ipap.jp/link?JPSJ/82/063713/ (cit. on p. 134).

[164] M. Horio et al. "Suppression of the Antiferromagnetic Pseudogap in the Electron-Doped High-Temperature Superconductor by Protect Annealing". In: *Nature Communications* 7 (Feb. 4, 2016), p. 10567. DOI: 10.1038/ncomms10567. URL: https://www.nature.com/articles/ncomms10567 (visited on 03/26/2019) (cit. on pp. 134, 135).

[165] *Deutschlands größtes Beschleunigerzentrum*. URL: https://www.desy.de/ (visited on 10/13/2021) (cit. on p. 134).

[166] U. Flechsig, L. Patthey, and T. Schmidt. "Performance Measurements at the SLS Spectroscopy Beamline". In: *AIP Conf. Proc.* 705 (2004), pp. 316–319. DOI: 10.1063/1.1757797 (cit. on p. 134).

[167] Y. Tokura, H. Takagi, and S. Uchida. "A Superconducting Copper Oxide Compound with Electrons as the Charge Carriers". In: *Nature (London)* 337 (1989), pp. 345–347. DOI: 10.1038/337345a0 (cit. on p. 135).

[168] Raphaël Photopoulos and Raymond Frésard. "A 3D Tight-Binding Model for La-Based Cuprate Superconductors". In: *Ann. Phys.* 531.12 (2019), p. 1900177. DOI: 10.1002/andp.201900177 (cit. on p. 135).

[169] Y. Onose et al. "Charge Dynamics in Underdoped $Nd_{2-x}Ce_xCuO_4$: Pseudogap and Related Phenomena". In: *Phys. Rev. B* 69.2 (Jan. 2004), p. 024504. DOI: 10.1103/PhysRevB.69.024504. URL: https://link.aps.org/doi/10.1103/PhysRevB.69.024504 (cit. on p. 135).

[170] N. E. Hussey et al. "Normal-State Magnetoresistance of Sr_2RuO_4". In: *Phys. Rev. B* 57.9 (Mar. 1998), pp. 5505–5511. DOI: 10.1103/PhysRevB.57.5505. URL: https://link.aps.org/doi/10.1103/PhysRevB.57.5505 (cit. on p. 135).

[171] Y. Nakamura and S. Uchida. "Anisotropic Transport Properties of Single-Crystal $La_{2-x}Sr_xCuO_4$: Evidence for the Dimensional Crossover". In: *Phys. Rev. B* 47.13 (Apr. 1993), pp. 8369–8372. DOI: 10.1103/PhysRevB.47.8369. URL: https://link.aps.org/doi/10.1103/PhysRevB.47.8369 (cit. on p. 135).

[172] Haofei I. Wei et al. "Electron Doping of the Parent Cuprate La_2CuO_4 without Cation Substitution". In: *Phys. Rev. Lett.* 117.14 (Sept. 2016), p. 147002. DOI: 10.1103/PhysRevLett.117.147002. URL: https://link.aps.org/doi/10.1103/PhysRevLett.117.147002 (cit. on p. 135).

[173] Dongjoon Song et al. "Electron Number-Based Phase Diagram of $Pr_{1-x}LaCe_xCuO_{4-\delta}$ and Possible Absence of Disparity between Electron- and Hole-Doped Cuprate Phase Diagrams". In: *Phys. Rev. Lett.* 118.13 (Mar. 2017), p. 137001. DOI: 10.1103/PhysRevLett.118.137001. URL: https://link.aps.org/doi/10.1103/PhysRevLett.118.137001 (cit. on p. 135).

[174] M. Horio et al. "Electronic Structure of Ce-Doped and -Undoped Nd_2CuO_4 Superconducting Thin Films Studied by Hard x-Ray Photoemission and Soft x-Ray Absorption Spectroscopy". In: *Phys. Rev. Lett.* 120.25 (June 2018), p. 257001. DOI: 10.1103/PhysRevLett.120.257001. URL: https://link.aps.org/doi/10.1103/PhysRevLett.120.257001 (cit. on p. 135).

[175] M. Horio et al. "Angle-Resolved Photoemission Spectroscopy of the Low-Energy Electronic Structure of Superconducting Pr_2CuO_4 Driven by Oxygen Nonstoichiometry". In: *Phys. Rev. B* 98.2 (July 2018), 020505(R). DOI: 10.1103/PhysRevB.98.020505. URL: https://link.aps.org/doi/10.1103/PhysRevB.98.020505 (cit. on p. 135).

[176] Shun Asano et al. "Ce Substitution and Reduction Annealing Effects on Electronic States in $Pr_{2-x}ce_xCuO_4$ Studied by Cu K-Edge x-Ray Absorption Spectroscopy". In: *J. Phys. Soc. Jpn.* 87.9 (2018), p. 094710. DOI: 10.7566/JPSJ.87.094710. URL: https://doi.org/10.7566/JPSJ.87.094710 (cit. on p. 135).

[177] N. P. Armitage et al. "Anomalous Electronic Structure and Pseudogap Effects in $Nd_{1.85}Ce_{0.15}CuO_4$". In: *Phys. Rev. Lett.* 87.14 (Sept. 2001), p. 147003. DOI: 10.1103/PhysRevLett.87.147003. URL: https://link.aps.org/doi/10.1103/PhysRevLett.87.147003 (cit. on p. 136).

[178] F. Schmitt et al. "Analysis of the Spectral Function of $Nd_{1.85}Ce_{0.15}CuO_4$ Obtained by Angle-Resolved Photoemission Spectroscopy". In: *Phys. Rev. B* 78.10 (Sept. 2008), 100505(R). DOI: 10.1103/PhysRevB.78.100505. URL: https://link.aps.org/doi/10.1103/PhysRevB.78.100505 (cit. on p. 136).

[179] Seung Ryong Park et al. "Angle-Resolved Photoemission Spectroscopy of Electron-Doped Cuprate Superconductors: Isotropic Electron-Phonon Coupling". In: *Phys. Rev. Lett.* 101.11 (Sept. 2008), p. 117006. DOI: 10.1103/PhysRevLett.101.117006. URL: https://link.aps.org/doi/10.1103/PhysRevLett.101.117006 (cit. on p. 136).

[180] Haiyun Liu et al. "Identification of Nodal Kink in Electron-Doped ($Nd_{1.85}Ce_{0.15}$) CuO4 Superconductor from Laser-Based Angle-Resolved Photoemission Spectroscopy". In: *EPJ Web of Conferences* 23 (2012), p. 00005. DOI: 10.1051/epjconf/20122300005. URL: https://doi.org/10.1051/epjconf/20122300005 (cit. on p. 136).

[181] T. Yoshida et al. "Systematic Doping Evolution of the Underlying Fermi Surface of $La_{2-x}Sr_xCuO_4$". In: *Phys. Rev. B* 74.22 (2006), p. 224510. DOI: 10.1103/PhysRevB.74.224510. URL: https://link.aps.org/doi/10.1103/PhysRevB.74.224510 (cit. on p. 136).

[182] J. Chang et al. "Anisotropic Quasiparticle Scattering Rates in Slightly Underdoped to Optimally Doped High-Temperature $La_{2-x}Sr_xCuO_4$ Superconductors". In: *Phys. Rev. B* 78.20 (Nov. 2008), p. 205103. DOI: 10.1103/PhysRevB.78.205103 (cit. on p. 137).

[183] W. Meevasana et al. "Extracting the Spectral Function of the Cuprates by a Full Two-Dimensional Analysis: Angle-Resolved Photoemission Spectra of $Bi_2Sr_2CuO_6$". In: *Phys. Rev. B* 77.10 (Mar. 2008), p. 104506. DOI: 10.1103/PhysRevB.77.104506. URL: https://link.aps.org/doi/10.1103/PhysRevB.77.104506 (cit. on p. 137).

[184] T. Yoshida et al. "Zn-Impurity Effects on Quasiparticle Scattering in $La_{2-x}Sr_xCuO_4$ Studied by Angle-Resolved Photoemission Spectroscopy". In: *Phys. Rev. B* 80.24 (Dec. 2009), p. 245113. DOI: 10.1103/PhysRevB.80.245113. URL: https://link.aps.org/doi/10.1103/PhysRevB.80.245113 (cit. on p. 138).

[185] M. Ikeda et al. "Effects of Chemical Pressure on the Fermi Surface and Band Dispersion of the Electron-Doped High-T_c Superconductors". In: *Phys. Rev. B* 80.1 (July 2009), p. 014510. DOI: 10.1103/PhysRevB.80.014510. URL: https://link.aps.org/doi/10.1103/PhysRevB.80.014510 (cit. on pp. 139, 142, 179).

[186] F. Schmitt et al. "High-Energy Anomaly in $Nd_{2-x}Ce_xCuO_4$ Investigated by Angle-Resolved Photoemission Spectroscopy and Quantum Monte Carlo Simulations". In: *Phys. Rev. B* 83.19 (May 2011), p. 195123. DOI: 10.1103/PhysRevB.83.195123. URL: https://link.aps.org/doi/10.1103/PhysRevB.83.195123 (cit. on p. 139).

[187] Ai Ikeda et al. "Incommensurate Defect-Driven Electron Correlations in $Pr_{1.85}Ce_{0.15}CuO_{4+\delta}$". In: *Phys. Rev. B* 94.5 (Aug. 2016), p. 054513. DOI: 10.1103/PhysRevB.94.054513. URL: https://link.aps.org/doi/10.1103/PhysRevB.94.054513 (cit. on p. 140).

[188] Tarapada Sarkar, Richard L. Greene, and S. Das Sarma. "Anomalous Normal-State Resistivity in Superconducting $La_{2-x}Ce_xCuO_4$: Fermi Liquid or Strange Metal ?" In: *Phys. Rev. B* 98.22 (Dec. 2018), p. 224503. DOI: 10.1103/PhysRevB.98.224503. URL: https://link.aps.org/doi/10.1103/PhysRevB.98.224503 (cit. on p. 140).

[189] K. Miyake, T. Matsuura, and C.M. Varma. "Relation between Resistivity and Effective Mass in Heavy-Fermion and A15 Compounds". In: *Solid State Communications* 71.12 (1989), pp. 1149–1153. ISSN: 0038-1098. DOI: 10.1016/0038-1098(89)90729-1. URL: http://www.sciencedirect.com/science/article/pii/0038109889907291 (cit. on pp. 140, 141).

[190] K. Byczuk et al. "Kinks in the Dispersion of Strongly Correlated Electrons". In: *Nat. Phys.* 3.3 (2007), pp. 168–171. ISSN: 1745-2481. DOI: 10.1038/nphys538. URL: https://doi.org/10.1038/nphys538 (cit. on pp. 140, 141).

[191] N. J. C. Ingle et al. "Quantitative Analysis of Sr_2RuO_4 Angle-Resolved Photoemission Spectra: Many-Body Interactions in a Model Fermi Liquid". In: *Phys. Rev. B* 72.20 (Nov. 2005), p. 205114. DOI: 10.1103/PhysRevB.72.205114. URL: https://link.aps.org/doi/10.1103/PhysRevB.72.205114 (cit. on p. 140).

[192] David Sénéchal and A.-M. S. Tremblay. "Hot Spots and Pseudogaps for Hole- and Electron-Doped High-Temperature Superconductors". In: *Phys. Rev. Lett.* 92.12 (Mar. 2004), p. 126401. DOI: 10.1103/PhysRevLett.92.126401. URL: https://link.aps.org/doi/10.1103/PhysRevLett.92.126401 (cit. on p. 141).

[193] Hena Das and Tanusri Saha-Dasgupta. "Electronic Structure of La_2CuO_4 in the T and T' Crystal Structures Using Dynamical Mean Field Theory". In: *Phys. Rev. B* 79.13 (Apr. 2009), p. 134522. DOI: 10.1103/PhysRevB.79.134522. URL: https://link.aps.org/doi/10.1103/PhysRevB.79.134522 (cit. on p. 141).

[194] Cédric Weber, Kristjan Haule, and Gabriel Kotliar. "Strength of Correlations in Electron- and Hole-Doped Cuprates". In: *Nat. Phys.* 6 (2010), pp. 574–578. DOI: 10.1038/nphys1706 (cit. on p. 141).

[195] Cédric Weber, Kristjan Haule, and Gabriel Kotliar. "Apical Oxygens and Correlation Strength in Electron- and Hole-Doped Copper Oxides". In: *Phys. Rev. B* 82.12 (Sept. 8, 2010), p. 125107. DOI: 10.1103/PhysRevB.82.125107. URL: https://link.aps.org/doi/10.1103/PhysRevB.82.125107 (visited on 03/27/2018) (cit. on p. 141).

[196] N. E. Hussey. "Non-Generality of the Kadowaki-Woods Ratio in Correlated Oxides". In: *J. Phys. Soc. Jpn* 74.4 (Apr. 2005), pp. 1107–1110. ISSN: 0031-9015. DOI: 10.1143/JPSJ.74.1107. URL: https://journals.jps.jp/doi/10.1143/JPSJ.74.1107 (visited on 01/26/2020) (cit. on p. 142).

[197] R. Eguchi et al. "Fermi Surfaces, Electron-Hole Asymmetry, and Correlation Kink in a Three-Dimensional Fermi Liquid $LaNiO_3$". In: *Phys. Rev. B* 79.11 (Mar. 2009), p. 115122. DOI: 10.1103/PhysRevB.79.115122. URL: https://link.aps.org/doi/10.1103/PhysRevB.79.115122 (cit. on pp. 142, 143, 179).

[198] E. Pavarini et al. "Band-Structure Trend in Hole-Doped Cuprates and Correlation with T_{cmax}". In: *Phys. Rev. Lett.* 87 (2001), p. 047003. URL: http://link.aps.org/doi/10.1103/PhysRevLett.87.047003 (cit. on pp. 142, 179).

[199] Noriaki Hamada. "Electronic Band Structure of $LaNiO_3$". In: *J. Phys. Chem. Solids* 54.10 (1993), pp. 1157–1160. ISSN: 0022-3697. DOI: 10.1016/0022-3697(93)90159-O. URL: http://www.sciencedirect.com/science/article/pii/0022369793901590 (cit. on pp. 142, 179).

[200] M. W. Haverkort et al. "Strong Spin-Orbit Coupling Effects on the Fermi Surface of Sr_2RuO_4 and Sr_2RhO_4". In: *Phys. Rev. Lett.* 101.2 (July 2008), p. 026406. DOI: 10.1103/PhysRevLett.101.026406. URL: https://link.aps.org/doi/10.1103/PhysRevLett.101.026406 (cit. on pp. 142, 179).

[201] E. A. Nowadnick et al. "Quantifying Electronic Correlation Strength in a Complex Oxide: A Combined DMFT and ARPES Study of $LaNiO_3$". In: *Phys. Rev. B* 92.24 (Dec. 2015), p. 245109. DOI: 10.1103/PhysRevB.92.245109. URL: https://link.aps.org/doi/10.1103/PhysRevB.92.245109 (cit. on p. 142).

[202] Jun Kondo. "Resistance Minimum in Dilute Magnetic Alloys". In: *Progress of Theoretical Physics* 32.1 (July 1, 1964), pp. 37–49. ISSN: 0033-068X. DOI: 10.1143/PTP.32.37. URL: https://doi.org/10.1143/PTP.32.37 (visited on 03/24/2021) (cit. on p. 147).

[203] P. W. Anderson. "Localized Magnetic States in Metals". In: *Phys. Rev.* 124.1 (Oct. 1, 1961), pp. 41–53. DOI: 10.1103/PhysRev.124.41. URL: https://link.aps.org/doi/10.1103/PhysRev.124.41 (visited on 06/29/2021) (cit. on p. 147).

[204] Sooyoung Jang et al. "Evolution of the Kondo Lattice Electronic Structure above the Transport Coherence Temperature". In: *PNAS* 117.38 (Sept. 22, 2020), pp. 23467–23476. ISSN: 0027-8424, 1091-6490. DOI: 10.1073/pnas.2001778117. pmid: 32887802. URL: https://www.pnas.org/content/117/38/23467 (visited on 05/11/2021) (cit. on pp. 147, 152).

[205] W. J. De Haas and G. J. Van Den Berg. "The Electrical Resistance of Gold and Silver at Low Temperatures". In: *Physica* 3.6 (June 1, 1936), pp. 440–449. ISSN: 0031-8914. DOI: 10.1016/S0031-8914(36)80009-3. URL: https://www.sciencedirect.com/science/article/pii/S0031891436800093 (visited on 06/29/2021) (cit. on p. 148).

[206] Alexander Cyril Hewson. *The Kondo Problem to Heavy Fermions*. Cambridge Studies in Magnetism. Cambridge: Cambridge University Press, 1993. ISBN: 978-0-521-59947-4. DOI: 10.1017/CBO9780511470752. URL: https://www.cambridge.org/core/books/kondo-problem-to-heavy-fermions/EDBEDC3F4492DD3EE27E02259935705A (visited on 06/29/2021) (cit. on p. 148).

[207] Prasanta Misra. *Heavy-Fermion Systems*. Elsevier, Dec. 11, 2007. 353 pp. ISBN: 978-0-08-055467-9 (cit. on pp. 148, 149).

[208] H. Fujii, T. Fujita, and G. Oomi. *Transport and Thermal Properties of F-Electron Systems*. Springer Science & Business Media, Dec. 6, 2012. 304 pp. ISBN: 978-1-4615-2868-5. Google Books: vSroBwAAQBAJ (cit. on p. 148).

[209] J. Flouquet et al. "Low-temperature Properties of CeAl3". In: *Journal of Applied Physics* 53.3 (Mar. 1, 1982), pp. 2127–2130. ISSN: 0021-8979. DOI: 10.1063/1.330755. URL: https://aip.scitation.org/doi/abs/10.1063/1.330755 (visited on 10/04/2021) (cit. on p. 148).

[210] G. R. Stewart, Z. Fisk, and M. S. Wire. "New Ce Heavy-Fermion System: $CeCu_6$". In: *Phys. Rev. B* 30.1 (July 1, 1984), pp. 482–484. DOI: 10.1103/PhysRevB.30.482. URL: https://link.aps.org/doi/10.1103/PhysRevB.30.482 (visited on 10/04/2021) (cit. on p. 148).

[211] V. V. Glushkov et al. "Spin Gap Formation in SmB6". In: *Physica B: Condensed Matter*. Proceedings of the International Conference on Strongly Correlated Electron Systems 378–380 (May 1, 2006), pp. 614–615. ISSN: 0921-4526. DOI: 10.1016/j.physb.2006.01.167. URL: https://www.sciencedirect.com/science/article/pii/S0921452606002936 (visited on 10/04/2021) (cit. on p. 148).

[212] G. Li et al. "Two-Dimensional Fermi Surfaces in Kondo Insulator SmB6". In: *Science* 346.6214 (Dec. 5, 2014), pp. 1208–1212. DOI: 10.1126/science.1250366. URL: https://www.science.org/doi/full/10.1126/science.1250366 (visited on 10/04/2021) (cit. on p. 148).

[213] M. Jaime et al. "Specific Heat of Ce3Bi4Pt3 at 60T". In: *Physica B: Condensed Matter*. Proceedings of the Sixth International Symposium on Research in High Magnetic Fields 294–295 (Jan. 1, 2001), pp. 240–244. ISSN: 0921-4526. DOI: 10.1016/S0921-4526(00)00650-5. URL: https://www.sciencedirect.com/science/article/pii/S0921452600006505 (visited on 10/04/2021) (cit. on p. 148).

[214] S. Paschen et al. "First Results on U2Ru2Sn Single Crystals". In: *Physica B: Condensed Matter*. Proceedings of the 23rd International Conference on Low Temperature Physics 329–333 (May 1, 2003), pp. 549–550. ISSN: 0921-4526. DOI: 10.1016/S0921-4526(02)02396-7. URL: https://www.sciencedirect.com/science/article/pii/S0921452602023967 (visited on 10/04/2021) (cit. on p. 148).

[215] Y. Takeda et al. "Temperature Dependence of the Electronic States of Kondo Semiconductor YbB12". In: *Physica B: Condensed Matter*. Proceedings of The International Symposium on Synchrotron Radiation Research for Spin and Electronic States in d and f Electron Systems 351.3 (Sept. 15, 2004), pp. 286–288. ISSN: 0921-4526. DOI: 10.1016/j.physb.2004.06.027. URL: https://www.sciencedirect.com/science/article/pii/S0921452604007355 (visited on 10/04/2021) (cit. on p. 149).

[216] Philipp Gegenwart, Qimiao Si, and Frank Steglich. "Quantum Criticality in Heavy-Fermion Metals". In: *Nature Phys* 4.3 (3 Mar. 2008), pp. 186–197. ISSN: 1745-2481. DOI: 10.1038/nphys892. URL: https://www.nature.com/articles/nphys892 (visited on 06/30/2021) (cit. on p. 149).

[217] F. Steglich et al. "Superconductivity in the Presence of Strong Pauli Paramagnetism: $CeCu_2Si_2$". In: *Phys. Rev. Lett.* 43.25 (Dec. 17, 1979), pp. 1892–1896. DOI: 10.1103/PhysRevLett.43.1892. URL: https://link.aps.org/doi/10.1103/PhysRevLett.43.1892 (visited on 06/30/2021) (cit. on pp. 149, 150).

[218] H. P. van der Meulen et al. "Field Suppression of the Heavy-Fermion State in $CeRu_2Si_2$". In: *Phys. Rev. B* 44.2 (July 1, 1991), pp. 814–818. DOI: 10.1103/PhysRevB.44.814. URL: https://link.aps.org/doi/10.1103/PhysRevB.44.814 (visited on 07/12/2021) (cit. on p. 150).

[219] L. C. Gupta et al. "Magnetic Behavior of the Kondo-Lattice System $CeRu_2Si_2$". In: *Phys. Rev. B* 28.7 (Oct. 1, 1983), pp. 3673–3676. DOI: 10.1103/PhysRevB.28.3673. URL: https://link.aps.org/doi/10.1103/PhysRevB.28.3673 (visited on 07/12/2021) (cit. on p. 150).

[220] J. D. Thompson et al. "Heavy Fermion State and Pressure-Induced Resistive Behaviour in $CeRu_2Si_2$". In: *Solid State Communications* 56.2 (Oct. 1, 1985), pp. 169–172. ISSN: 0038-1098. DOI: 10.1016/0038-1098(85)90733-1. URL: https://www.sciencedirect.com/science/article/pii/0038109885907331 (visited on 07/12/2021) (cit. on p. 150).

[221] E. Stryjewski and N. Giordano. "Metamagnetism". In: *Advances in Physics* 26.5 (Sept. 1, 1977), pp. 487–650. ISSN: 0001-8732. DOI: 10.1080/00018737700101433. URL: https://doi.org/10.1080/00018737700101433 (visited on 10/04/2021) (cit. on p. 150).

[222] J. Flouquet et al. "Itinerant Metamagnetism of CeRu2Si2: Bringing out the Dead. Comparison with the New Sr3Ru2O7 Case". In: *Physica B: Condensed Matter* 319.1 (July 1, 2002), pp. 251–261. ISSN: 0921-4526. DOI: 10.1016/S0921-4526(02)01126-2. URL: http://www.sciencedirect.com/science/article/pii/S0921452602011262 (visited on 02/11/2019) (cit. on p. 150).

[223] H. Aoki et al. "Transition of f Electron Nature from Itinerant to Localized: Metamagnetic Transition in $CeRu_2Si_2$ Studied via the de Haas–van Alphen Effect". In: *Phys. Rev. Lett.* 71.13 (Sept. 27, 1993), pp. 2110–2113. DOI: 10.1103/PhysRevLett.71.2110. URL: https://link.aps.org/doi/10.1103/PhysRevLett.71.2110 (visited on 01/14/2020) (cit. on p. 150).

[224] R. Daou, C. Bergemann, and S. R. Julian. "Continuous Evolution of the Fermi Surface of $CeRu_2Si_2$ across the Metamagnetic Transition". In: *Phys. Rev. Lett.* 96.2 (Jan. 17, 2006), p. 026401. DOI: 10.1103/PhysRevLett.96.026401. URL: https://link.aps.org/doi/10.1103/PhysRevLett.96.026401 (visited on 02/06/2019) (cit. on pp. 150, 153).

[225] F. S. Tautz et al. "The Nature of Elementary Excitations below and above the Metamagnetic Transition in $CeRu_2Si_2$". In: *Physica B: Condensed Matter*. Proceedings of the International Conference on Strongly Correlated Electron Systems 206–207 (Feb. 1, 1995), pp. 29–32. ISSN: 0921-4526. DOI: 10.1016/0921-4526(94)00359-4. URL: http://www.sciencedirect.com/science/article/pii/0921452694003594 (visited on 04/27/2020) (cit. on pp. 150, 152).

[226] T. Willers et al. "Spectroscopic Determination of Crystal-Field Levels in $CeRh_2Si_2$ and $CeRu_2Si_2$ and of the $4f^0$ Contributions in CeM_2Si_2 (M=Cu, Ru, Rh, Pd, and Au)". In: *Phys. Rev. B* 85.3 (Jan. 18, 2012), p. 035117. DOI: 10.1103/PhysRevB.85.035117. URL: https://link.aps.org/doi/10.1103/PhysRevB.85.035117 (visited on 06/18/2021) (cit. on pp. 151, 158, 170).

[227] T. Endstra, G. J. Nieuwenhuys, and J. A. Mydosh. "Hybridization Model for the Magnetic-Ordering Behavior of Uranium- and Cerium-Based 1:2:2 Intermetallic Compounds". In: *Phys. Rev. B* 48.13 (Oct. 1, 1993), pp. 9595–9605. DOI: 10.1103/PhysRevB.48.9595. URL: https://link.aps.org/doi/10.1103/PhysRevB.48.9595 (visited on 10/08/2021) (cit. on pp. 151, 163).

[228] A. Koizumi et al. "f Electron Contribution to the Change of Electronic Structure in $CeRu_2Si_2$ with Temperature: A Compton Scattering Study". In: *Phys. Rev. Lett.* 106.13 (Mar. 28, 2011), p. 136401. DOI: 10.1103/PhysRevLett.106.136401. URL: https://link.aps.org/doi/10.1103/PhysRevLett.106.136401 (visited on 10/11/2021) (cit. on pp. 152, 163).

[229] *CASSIOPEE — French National Synchrotron Facility*. URL: https://www.synchrotron-soleil.fr/en/beamlines/cassiopee (visited on 10/05/2021) (cit. on p. 153).

[230] M. Hoesch et al. "A Facility for the Analysis of the Electronic Structures of Solids and Their Surfaces by Synchrotron Radiation Photoelectron Spectroscopy". In: *Review of Scientific Instruments* 88.1 (Jan. 1, 2017), p. 013106. ISSN: 0034-6748. DOI: 10.1063/1.4973562. URL: https://aip.scitation.org/doi/abs/10.1063/1.4973562 (visited on 10/05/2021) (cit. on p. 153).

[231] M. Yano et al. "Electronic Structure of $CeRu_2X_2$ (X = Si, Ge) in the Paramagnetic Phase Studied by Soft X-Ray ARPES and Hard x-Ray Photoelectron Spectroscopy". In: *Phys. Rev. B* 77.3 (Jan. 15, 2008), p. 035118. DOI: 10.1103/PhysRevB.77.035118. URL: https://link.aps.org/doi/10.1103/PhysRevB.77.035118 (visited on 02/11/2019) (cit. on p. 153).

[232] J. D Denlinger et al. "Comparative Study of the Electronic Structure of XRu_2Si_2: Probing the Anderson Lattice". In: *Journal of Electron Spectroscopy and Related Phenomena*. Strongly Correlated Systems 117–118 (June 1, 2001), pp. 347–369. ISSN: 0368-2048. DOI: 10.1016/S0368-2048(01)00257-2. URL: http://www.sciencedirect.com/science/article/pii/S0368204801002572 (visited on 02/13/2019) (cit. on p. 153).

[233] Heike Pfau et al. "Thermoelectric Transport across the Metamagnetic Transition of $CeRu_2Si_2$". In: *Phys. Rev. B* 85.3 (Jan. 30, 2012), p. 035127. DOI: 10.1103/PhysRevB.85.035127. URL: https://link.aps.org/doi/10.1103/PhysRevB.85.035127 (visited on 06/18/2019) (cit. on p. 153).

[234] S. Patil et al. "ARPES View on Surface and Bulk Hybridization Phenomena in the Antiferromagnetic Kondo Lattice CeRh 2 Si 2". In: *Nature Communications* 7.1 (1 Mar. 18, 2016), p. 11029. ISSN: 2041-1723. DOI: 10.1038/ncomms11029. URL: https://www.nature.com/articles/ncomms11029 (visited on 11/20/2020) (cit. on pp. 153, 154, 157).

[235] K. Kummer et al. "Temperature-Independent Fermi Surface in the Kondo Lattice $YbRh_2Si_2$". In: *Phys. Rev. X* 5.1 (Mar. 12, 2015), p. 011028. DOI: 10.1103/PhysRevX.5.011028. URL: https://link.aps.org/doi/10.1103/PhysRevX.5.011028 (visited on 11/27/2020) (cit. on p. 154).

[236] L. V. Pourovskii et al. "Theoretical Prediction and Spectroscopic Fingerprints of an Orbital Transition in $CeCu_2Si_2$". In: *Phys. Rev. Lett.* 112.10 (Mar. 13, 2014), p. 106407. DOI: 10.1103/PhysRevLett.112.106407. URL: https://link.aps.org/doi/10.1103/PhysRevLett.112.106407 (visited on 08/02/2021) (cit. on pp. 160, 162).

Index